Department of Precision and Microsystems Engineering

In situ stiffness adjustment for AFM probes

M.L.C. de Laat

Report no : MSD 2016.008
Coach : Dr. M.K. Ghatkesar, Dr. H.H. Pérez Garza
Professor : Prof. Dr. U. Staufer
Specialisation : Micro & Nano Engineering
Type of report : Master Thesis
Date : 10 February 2016

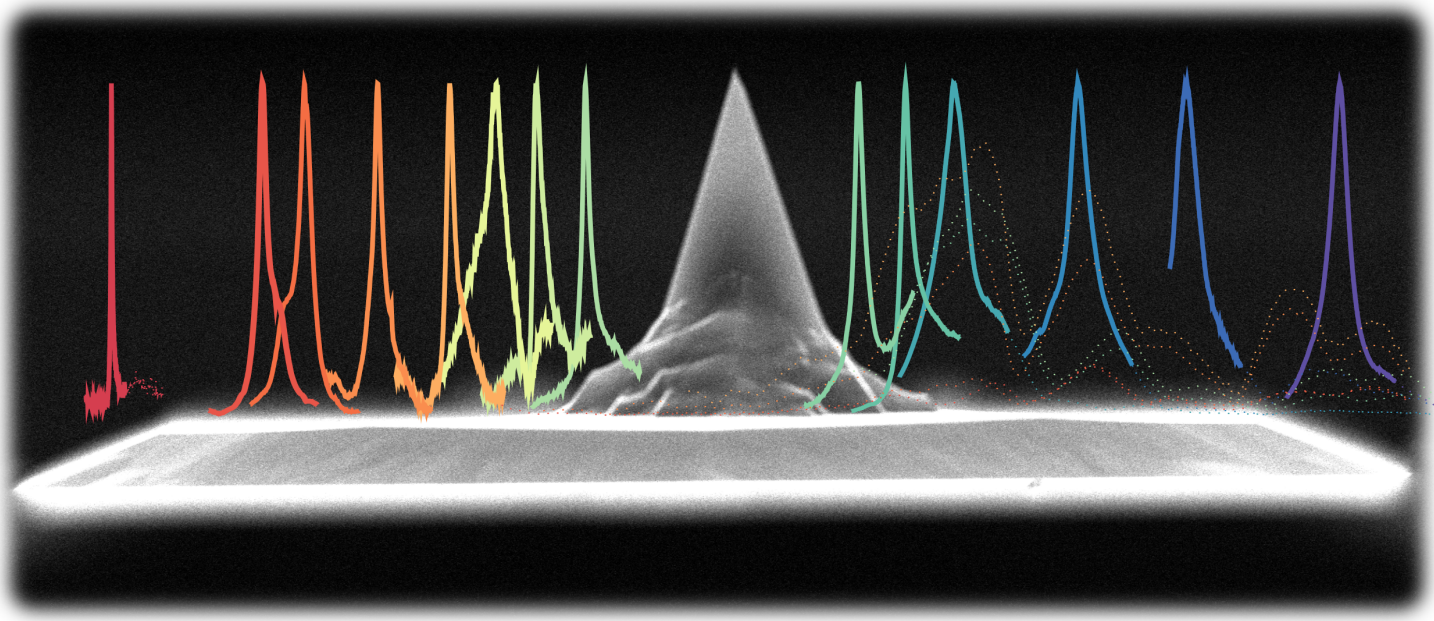

In situ STIFFNESS ADJUSTMENT FOR AFM PROBES

by

M.L.C. de Laat

in partial fulfillment of the requirements for the degree of

Master of Science

in Mechanical Engineering (Precision and Microsystems Engineering)

at the Delft University of Technology,

to be defended publicly on Wednesday February 10, 2016 at 14:00.

Coach:	Dr. M.K. Ghatkesar	TU Delft
	Dr. H. H. Pérez Garza	TU Delft, DENSsolutions
Thesis committee:	Prof. Dr. U. Staufer	TU Delft
	Dr. N. Tolou	TU Delft

An electronic version of this thesis is available at `http://repository.tudelft.nl/`.

TU Delft Delft University of Technology

ABSTRACT

The choice on which type of cantilever to use for Atomic Force Microscopy (AFM) depends on the type of the experiment being done. Typically, the cantilever has to be exchanged when a different stiffness is required and the entire alignment has to be repeated. In the present work, a method to *in situ* adjust the stiffness of an AFM cantilever is developed.

To identify potential solutions, an extensive literature review was performed on the state-of the art in stiffness adjustment methods in MEMS. The categorization of the found devices was based on the following principles: Electrostatic, Mechanical, Stressing effects and changing Young's modulus. A comprehensive table is made listing variety of properties of the devices. A figure mapping all these devices for their respective operating range of stiffness is also given. It was concluded that electrostatic tuning is the most applied and versatile method, but large and complex devices were designed. Mechanical tuning is often discrete, but provides a large tuning range for a simple device. Over all, the review can be used as a guide for designers of MEMS that require stiffness tuning.

After evaluating the literature and considering the boundary conditions, three concepts were compared. The concept based on changing the effective length of the cantilever was chosen to be implemented. By applying a voltage between the AFM cantilever and an electrode (with an insulating layer at the point of contact), the cantilever snaps to the electrode, reducing the cantilever's effective length.

The static pull-in behavior of the system was initially characterized. An analytical and a COMSOL model were developed. With these models, the pull-in voltage and cantilever deflection behavior were estimated. An experiment setup was build for validation of the models. The cantilever deflection for a varying electrostatic load was visualized and measured from side view. The experiments were done with commercial AFM probes and an electrode that is controlled with a robotic nanomanipulator. The results obtained for the pull-in voltage and deflection at pull-in from the models and experiments were within 13% and 19% error respectively. Subsequently, an analysis on the post-pull in behavior of the system with a time dependent study in COMSOL is presented.

To proof the claims on stiffness adjustment, experiments were performed to study the cantilever in the dynamic mode. The fundamental resonance frequency of the cantilever was measured for a varying effective length using a laser Doppler vibrometer. The results obtained matched with the theoretical estimated numbers. The stiffness was adjusted *in situ* in the range of $0.2\,\mathrm{N\,m^{-1}}$ to $27\,\mathrm{N\,m^{-1}}$, covering two orders of magnitude using one single cantilever.

PREFACE AND ACKNOWLEDGMENT

This thesis is the result of my master project, which was conducted within the group of Micro- and Nano Engineering at the faculty of Mechanical Engineering at Delft University of Technology.

I would like to take this opportunity to thank a few people that helped me throughout this project. First of all, I would like to thank Dr. Murali Ghatkesar, who was my daily supervisor during the project. The bi-weekly meetings that we had were the building blocks of the project. They were very constructive and enjoyable. It was no exception that these meeting would take twice as long as planned due to all sorts of conversations, which were definitely not limited to the topic of the thesis. I appreciate these meetings and commitment from my supervisor that came with it. Two manuscripts were submitted to a journal, that will hopefully get accepted. Writing in a publishable format took a lot of time and energy. Not only for me, but also for him to provide valuable feedback, which was indispensable for the result. Murali gave me the chance to go to the 'International MicroNanoConference' in Amsterdam to give a poster presentation. It was a great experience to attend this conference and to interact with people from the field of Atomic Force Microscopy and micro- and nano science in general. Lastly, Murali presented my work to his former colleague Dr. Akshay Naik, assistant professor at the Centre for Nano Science and Engineering at the Indian Institute of Science in Bangalore, where he attended a conference. Dr. Naik invited me to present my work at his institute. I will visit this institute from the 30th of April until 4th of May. I want to thank Murali for the collaboration and great opportunities he gave me during this project.

Secondly, I would like to thank my second supervisor, Dr. Hugo Pérez Garza. During the first months of the project he was a PhD student at the MNE group and later went to work for DENS Solutions. I'm very thankful, that he remained connected to the project, even though his work at the university was done. Some of the meeting we had were only ten minutes. But the meetings were incredibly effective and gave me so many new ideas and energy that I could continue for weeks. Hugo is a co-author of the manuscripts, helped me a lot with the poster for the conference and was a great support for initializing the experiments. Thank you for transferring so much enthusiasm, energy and good advice!

I want to thank Prof.Dr. Just Herder for being co-author of the review manuscript. Just is an experienced author of many articles and provided me with valuable advise and feedback.

During the experimental phase, Tjitte-Jelte Peters, PhD student at the group of Micro- and Nano Engineering was of great help. He trained me in using the laser Doppler vibrometer, which I've used to perform resonance frequency experiments. He helped with the clean room steps during the fabrication of the electrodes. Thank you for the indispensable help and showing me around at the EKL clean room facilities.

I would like to thank the head of the thesis committee prof.Dr. Urs Staufer and the external committee member Dr. Nima Tolou for their time and effort they put in reading of this work, attending my presentation and examination.

Thank you, technical support staff: Rob Luttjeboer, Harry Jansen and Patrick van Holst for helping me with the experimental setup. Thank you, PhD's, staff and fellow students from MNE for providing me with valuable feedback during, and outside the MNE meetings, pleasant collaborations, interesting presentations and discussions . Thank you, guys at my office, for spending so many hours in the same room with me, joking around, having lunch, an occasional beer and support during this project.

Above all I would like to thank my parents for their unconditional love, support and believe in me.

Marcel de Laat
Delft, January 2016

CONTENTS

LIST OF FIGURES

LIST OF TABLES

1

INTRODUCTION

The Atomic Force Microscope (AFM) was invented by Binnig and Quate in 1986 [1]. AFM is a technology that can image samples with extreme high resolution. In good conditions sub-nanometer resolution can be achieved and it is possible to visualize individual atoms [2]. An AFM uses a silicon based chip with a cantilever beam and a very sharp tip to probe a surface. The forces that act on the tip cause the cantilever beam to deflect, which is measured with a sensor as shown in figure 1.1. With this information, the topography of the surface can be reconstructed. The AFM has some advantages over competitive microscopy technologies: It does not require the samples to be conductive, like it is the case for Scanning Tunneling Microscopy (STM), Scanning Electron Microscopy (SEM) and Transmission Electron Microscopy (TEM). So special preparation of the sample is not required. Samples can be imaged in a liquid environment, which makes it possible to measure biological samples *in vivo* in high resolution. The AFM can also measure the out-of-plane height profile of the sample, while for other technologies this can only be estimated. In addition, it is also possible to calculate the force between tip and sample by using the (known) stiffness of the cantilever, using Hooke's law. This information can for instance be used to measure material properties like Young's modulus [3] and molecular interaction force [4, 5]. More details about the basic working principles of AFM are found in appendix A.

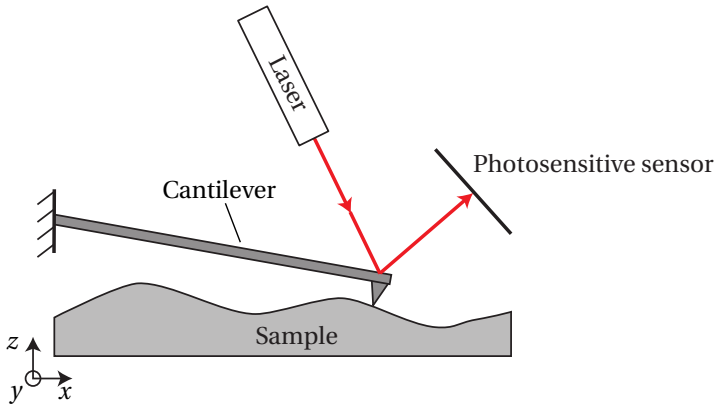

Figure 1.1: The main principle of the AFM: A sample is probed with a sharp tip, suspended by a cantilever. The deflection of the cantilever is measured with a sensor, such that the topography of the surface can be measured with extremely high accuracy.

1.1. PROBLEM STATEMENT

The stiffness of the cantilever is important to the type of measurement mode that needs to be performed; for a different type of measurement a different stiffness is needed, as shown figure 1.2 [6]. In practice, users have to exchange the cantilever if they want to switch to a different stiffness. The probe holder needs to be

dismounted and the probe needs to be replaced with tweezers. Next, the probe holder needs to be remounted and the alignment process of the sensor has to be repeated. A probe with an *in situ* adjustable stiffness would provide a faster solution for this time consuming process and opens the door to new applications:

1. Peak Force tapping mode is used for simultaneous imaging and Young's modulus mapping [7]. Cantilevers with a stiffness in the order of $40\,\mathrm{N\,m^{-1}}$ are commonly used [8]. The stiffness of the cantilever should match the Young's modulus for high accuracy measurements. Samples with high Young's modulus variability ($\sim$ 1 order of magnitude [9]) cannot be accurately measured with a single cantilever. A tunable stiffness probe would provide the solution to successfully measure these samples.
2. Living biological cells can be imaged with AFM. The outer membrane is very soft, while the underlying cytoskeleton is approximately 10× stiffer. A stiffness adjustable probe could image the outer membrane with a low stiffness ($\sim 0.01\,\mathrm{N\,m^{-1}}$) and the underlying structure with a higher stiffness ($\sim 0.1\,\mathrm{N\,m^{-1}}$) [10].
3. Combination of imaging and spectroscopy in a single measurement. For high resolution imaging, non contact mode is often preferred, which requires a stiff cantilever ($\sim 40\,\mathrm{N\,m^{-1}}$). For force spectroscopy a soft cantilever is required ($\sim 0.1\,\mathrm{N\,m^{-1}}$) such that a high resolution measurement can be performed, without damaging the sample.

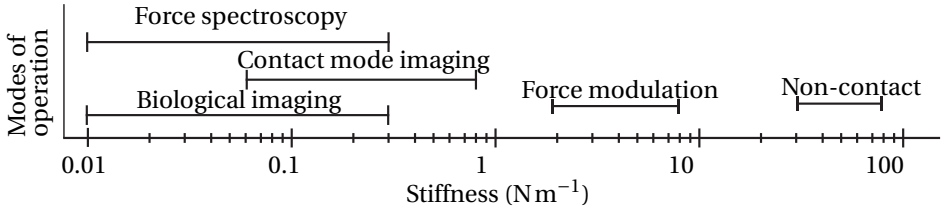

Figure 1.2: The range of stiffness for the AFM cantilever for different imaging modes. More details are found in appendix A.3.

1.2. REQUIREMENTS

There are a two main requirements. The first is about the range of stiffness that should be covered. The other requirement is to satisfy the compatibility with conventional AFM systems:

- **Range of stiffness:** In section 1.1 several applications for a stiffness tunable probes were discussed. The demands for tuning range differ per application. But the required change in stiffness is at least one order of magnitude, which should be covered by the probe.
- **Compatibility:** The design should be compatible with commercially available AFM systems, such that it can be widely applied to current systems and commercial success could be possible. Therefore, the system should be compatible with the widely applied laser deflection sensor, and the extra electronic equipment should be minimized as much as possible.

"*The goal of this thesis is to adjust the stiffness of an AFM cantilever in situ, such that it covers at least one order of magnitude while it remains compatible with conventional AFM systems.*"

1.3. ORGANIZATION OF THE THESIS

To identify potential solutions an extensive literature review was performed on the state-of the art in stiffness adjustment methods in MEMS, which is found in chapter 2. In chapter 3 three concepts are compared and the chosen solution is presented, which is elaborated in the remaining chapters. In chapter 4 the results of the thesis are presented, which are written in a journal-style format. These results are supported with supplementary material that are found in chapters 5 and 6. The thesis ends with the conclusions and recommendations in chapter 7.

REFERENCES

[1] G. Binnig, C. F. Quate, and C. Gerber, "Atomic Force Microscope," *Physical Review Letters*, vol. 56, pp. 930–933, mar 1986.

[2] T. R. Albrecht and C. F. Quate, "Atomic resolution imaging of a nonconductor by atomic force microscopy," *Journal of Applied Physics*, vol. 62, p. 2599, oct 1987.

[3] N. A. Burnham, "Measuring the nanomechanical properties and surface forces of materials using an atomic force microscope," *Journal of Vacuum Science & Technology A: Vacuum, Surfaces, and Films*, vol. 7, p. 2906, jul 1989.

[4] O. H. Willemsen, M. M. Snel, A. Cambi, J. Greve, B. G. De Grooth, and C. G. Figdor, "Biomolecular interactions measured by atomic force microscopy.," *Biophysical journal*, vol. 79, pp. 3267–81, dec 2000.

[5] T. Hugel and M. Seitz, "The Study of Molecular Interactions by AFM Force Spectroscopy," *Macromolecular Rapid Communications*, vol. 22, pp. 989–1016, sep 2001.

[6] Y. F. Dufrêne, D. Martínez-Martín, I. Medalsy, D. Alsteens, and D. J. Müller, "Multiparametric imaging of biological systems by force-distance curve–based AFM," *Nature Methods*, vol. 10, pp. 847–854, aug 2013.

[7] Bruker, "Peak Force Tapping Mode."

[8] Bruker, "Application Note #133: Introduction to Bruker's ScanAsyst and PeakForce Tapping AFM Technology."

[9] T. G. Kuznetsova, M. N. Starodubtseva, N. I. Yegorenkov, S. a. Chizhik, and R. I. Zhdanov, "Atomic force microscopy probing of cell elasticity.," *Micron (Oxford, England : 1993)*, vol. 38, pp. 824–33, jan 2007.

[10] C. Mueller-Falcke, Y.-A. Song, and S.-G. Kim, "Tunable Stiffness Scanning Microscope Probe," in *SPIE 5604, Optomechatronic Micro/Nano Components, Devices, and Systems* (Y. Katagiri, ed.), vol. 5604, pp. 31–37, oct 2004.

2

MANUSCRIPT: A REVIEW ON *in situ* STIFFNESS ADJUSTMENT METHODS IN MEMS

To identify potential solutions an extensive literature review was performed on the state-of the art in stiffness adjustment methods in MEMS. Devices that were found in literature were categorized based on the following principles: Electrostatic, Mechanical, Stressing effects and changing Young's modulus. A comprehensive table is made, listing a variety of properties of these devices. A figure mapping all these devices for their respective operating range of stiffness is also given. It was concluded that electrostatic tuning is the most applied and versatile method, but large and complex devices were designed. Mechanical tuning is often discrete, but provides a large tuning range for a simple device. The literature review is written in a journal article format and is aimed at designers of MEMS to enable them with an overview on existing stiffness adjustment methods. The manuscript is submitted to a journal and is under review.

Topical Review:

A review on *in situ* stiffness adjustment methods in MEMS

M L C de Laat[1], H H Pérez Garza[1,2], J L Herder[1], M K Ghatkesar[1⋆]
[1] Micro and Nano Engineering Group, Faculty of Mechanical, Maritime and Materials (3mE) Engineering, Delft University of Technology, Mekelweg 2, 2628 CD, Delft, The Netherlands
[2] DENSsolutions, Informaticalaan 12, 2628ZD, Delft, The Netherlands
⋆ E-mail: m.k.ghatkesar@tudelft.nl

Abstract:
In situ stiffness adjustment in microelectromechanical systems (MEMS) is used in a variety of applications such as radio-frequency (RF) mechanical filters, energy harvesters, atomic force microscopy and vibration detection sensors. In this review we enable designers with an overview of existing stiffness adjustment methods, their working principle, and possible tuning range. The concepts are categorized according to their physical working principle. It is concluded that the electrostatic adjustment principle is the most applied method, and both a small and large range in stiffness can be achieved. But in order to obtain wide range in stiffness change, large and complex devices were designed. Mechanical stiffness adjustment is found to be a space-effective way of obtaining large changes in stiffness, but these methods are often discrete and require large tuning voltages. Stiffness tuning through stressing effects and change in Young's modulus was only used for small changes. Tuning by change in second moment of inertia was used for an intermediate tuning range.

2.1. INTRODUCTION

Micro-electromechanical systems (MEMS) are small microchips that integrate mechanical and electrical functionality onto a single device. Many of these MEMS have deformable structures where the stiffness is a key factor in the performance of the device. An example is the stiffness of the cantilever of an Atomic Force Microscope (AFM) probe, where the stiffness should match the mode of operation and the mechanical properties of the sample. Design for stiffness is also very important for device where the resonance frequency is the determining factor in the performance, because this is depending on the stiffness ($f_0 = \frac{1}{2\pi}\sqrt{\frac{k_{\text{eff}}}{m_{\text{eff}}}}$, where k_{eff} and m_{eff} are the effective stiffness and effective mass respectively). Eminent examples are RF-filters, mass sensors, gyroscopes and energy harvesters.

The ability to adjust the stiffness after fabrication can provide great benefits to the performance of MEMS: it can compensate for unwanted manufacturing inaccuracies and influences of the operational environment (like temperature, humidity etc.) or it can increase the operational range.

Several methods to achieve this change in stiffness are described in literature. However, an organized review of all these techniques is not available, which is addressed in this paper. Earlier, a review has been made on variable stiffness devices [1], however it does not cover MEMS. Furthermore, there are several reviews that cover frequency tuning in MEMS [2, 3], which is closely related to stiffness tuning (one of the approaches of tuning the resonance frequency is by tuning the

stiffness). This review only covers stiffness adjustment methods in MEMS and compares these devices on their stiffness adjusting capabilities. The stiffness change should be reversible, controllable and *in situ* (while the device is in operation). Some devices show stiffness tuning effects only in dynamic behavior [4, 5]. These devices are not be addressed in this review. Stiffness adjustment covers both continuous tuning- and discrete switching of stiffness. Both are be addressed in this review. The contribution of this paper is an organized overview on the state of the art of in situ stiffness adjustment in MEMS and the advantages and disadvantages of the found methods. A categorization is defined, which is used throughout the paper to sort the literature. The results are summarized in a table and a graph. Those are intended to be a selection tool for designers that need stiffness adjustment capabilities in MEMS.

In the following sections, the method that was used are explained, covering the search method, definition of the classification and the key properties of the found literature. Next, the results are presented and they are summarized in a table and graph. Lastly, the results are discussed and the conclusions are presented.

2.2. METHODS

In this part the methods are presented that were used for this review. First the search method is discussed, followed by the categorization that is used and the key properties that are addressed.

2.2.1. SEARCH METHOD

Many devices that have stiffness adjustment capabilities are applied in resonance tuning applications. To get a complete overview, the search was not only aimed at stiffness tuning, but also on frequency tuning. Only the devices that achieved frequency tuning through stiffness tuning are included in the results though. As an initial search the key words *stiffness, compliance, spring constant, frequency* were combined with *tuning, adjusting, switching, changing, change, varying, softening, hardening*. The references were also checked.

2.2.2. CATEGORIZATION

The categorization was established to sort the found literature. This is done according to the physical working principle. Some of these categories also have sub-categories to differentiate distinctive methods that were used. The categorization can be found in table 2.1. The first group uses electrostatic effects to add a stiffness to the system. There are four different tuning methods that can be distinguished: *Parallel plate*, *Varying gap*, *Varying electrode shape* and *Non-interdigitated comb fingers*. These are further explained in section 2.3.1. The second group uses mechanical tuning, that can either be achieved by *changing the effective length* of the suspension or by *engaging extra mechanical springs*. These are addressed in section 2.3.2. The third category uses a change in the second moment of inertia to change the stiffness (section 2.3.3). The fourth group uses compressive and axial stressing effects for stiffness adjustments, that can be induced by *piezoelectric elements*, *thermal expansion* or by *electrostatic forces*. This is discussed in section 2.3.4. The Young's modulus (elasticity of a material) has got a temperature dependency. So the stiffness, which is dependent on the Young's Modulus, can be tuned by changing the temperature. This effect is used by the devices in the final category (section 2.3.5).

Table 2.1: Categorization of stiffness adjustment methods used in this review.

Physical Principle	**Sub-category**
Electrostatic	Parallel plate
	Varying gap
	Varying electrode shape
	Non-interdigitated
Mechanical	Change effective length
	Engaging mechanical springs
Second moment of inertia	-
Stressing effects	Piezoelectrically induced
	Thermally induced
	Electrostatically induces
Young's modulus	-

2.2.3. KEY PROPERTIES

The performance of the devices is addressed according to several key properties. These key properties are used in table 2.2 to describe the devices.

They are defined as:

- **Unadjusted stiffness (k_0)**: The stiffness of the system in the direction of motion, when no tuning voltage is applied (all of the mechanisms are voltage controlled).

- **Change in stiffness ($\Delta k = k_{tun} - k_0$)**: The difference between the unadjusted stiffness k_0 and the tuned stiffness k_{tun}. This can either be a positive or negative number, depending on whether the method increases or decreases the stiffness.

- **Normalized change in stiffness** $\left(k_{norm} = \frac{k_{high}}{k_{low}}\right)$: The ratio between the highest and lowest achievable stiffness in the device. When the stiffness has decreased: $k_{high} = k_0$ and $k_{low} = k_{tun}$, when the stiffness is increased $k_{high} = k_{tun}$ and $k_{low} = k_0$. A similar parameter was used in an earlier review [1].

- **Tuning voltage (V)**: The voltage that is applied to the system in order to achieve the maximum stiffness adjustment effect.

- **Size**: The size of the system. In some of the found literature the size of the device is explicitly mentioned. When this is not the case, micro graphs or schematics are used to make an estimate, if a reference scale is present.

- **Relative Size**: The relative size of the tuning mechanism with respect to the entire system, expressed as a percentage in steps of 20% (0-20, 21-40, 41-60, 61-80, 81-100). This is estimated from micro graphs or schematics of the devices. The size of the tuning mechanism is defined as the amount of space it adds to the system; it is the difference between the size of the current system and the size it would have without stiffness tuning capabilities.

- **Motion**: MEMS are usually made out of silicon wafers. The motion of the device can either be in the plane of the wafer, or out of plane.

2.2.4. DERIVE STIFFNESS CHANGE FROM RESONANCE FREQUENCY

A lot of the concepts that are discussed in this section are rather designed to change the resonant frequency than to change the stiffness, It is not always possible to find the stiffness of the devices in these papers. In the case where both the unadjusted- and the adjusted resonant frequency are known and the (effective) mass remains constant, it is possible to determine the ratio between unadjusted and adjusted stiffness. The effective mass of the system is expressed as a function of the effective stiffness and resonance frequency and set equal for the high- and low stiffness state of the system. When the untuned stiffness is known, the tuned stiffness can be derived.

$$f = \frac{1}{2\pi}\sqrt{\frac{k_{eff}}{m_{eff}}} \tag{2.1}$$

$$m_{eff\text{-}high} = m_{eff\text{-}low} \tag{2.2}$$

$$\frac{k_{eff\text{-}high}}{k_{eff\text{-}low}} = \left(\frac{f_{high}}{f_{low}}\right)^2 \tag{2.3}$$

With f the resonance frequency, k_{eff} the effective stiffness and m_{eff} the effective mass. The subscripts 'high' and 'low' are used to indicate the high and low stiffness state of the system.

2.3. RESULTS

The results are sorted according to the categorization that was defined in section 2.2.2. For each category the theory behind the working principle is explained in the introduction and examples found in literature are given. The examples are briefly explained; for more details the original papers can be consulted. In table 2.2 the found literature and its performance indicators are summarized. In figure 2.1 the devices are presented, where the relation between the change in stiffness and normalized change in stiffness are indicated. The devices of which the unadjusted stiffness and change in stiffness could not be found or calculated are not included in this graph and table. The color and symbols, that are used in the table correspond to the ones used in the graph. This provides a tool to select a concept for a specific application.

Table 2.2: Summary of in situ adjustable stiffness devices. Only devices of which the stiffness data was presented in- or could be derived from the original literature are included in this overview. The definition of the performance indicators can be found in section 2.2.3. The reference in the table corresponds to both the number in the bibliography and the ones used in figure 2.1. A letter between parentheses in the reference column indicates that more than one device is included from a single reference.

Physical Principle	**Subgroup and section**	**Reference**	**Untuned stiffness** ($N m^{-1}$)	**Change in Stiffness** ($N m^{-1}$)	**Normalized change in stiffness**	**Tuning voltage** (V)	**Size**	**Relative size (%)**	**Motion**
Electrostatic •	Parallel plate (2.3.1.1)	[6](a)	17.41	-16.79	28.08	46.1	$0.065\,mm^2$	81-100	In Plane
		[7]	29	-9.4	1.48	50	$1.4 \times 1.8 mm$	21-40	In Plane
		[8]	24.4	-13.4	2.22	53	$250\,\mu m$(diameter)[a]	21-40	Out of plane
		[6](b)	5.1	-3.2	2.7	22.4	-	81-100	In Plane
		[9]	1.03	-1	29	10	$650 \times 530\,\mu m$	41-60	In Plane
		[10]	0.1338	-0.03	1.32	-	$840 \times 520\,\mu m$	0-20	Out of Plane
	(nanoresonator) (2.3.1.1)	[11]	0.09	0.027	1.3	0.58	$30\,\mu m \times 200 \times 104\,nm$[a]	-	Out of plane
	Varying gap (2.3.1.2)	[12]	0.6	-0.05	1.11	29	$3020 \times 2000\,\mu m$	0-20	In Plane
		[13]	17.3	-1	1.06	60	$1000 \times 1250\,\mu m$	81-100	In Plane
		[14](a)	0.47	-0.47	∞[d]	80	-	41-60	In Plane
		[14](b)	0.47	0.28	1.60	90	-	41-60	In Plane
		[15]	2.64	-2.11	5	150	$460 \times 840\,\mu m$	81-100	In Plane
	Varying electrode surface (2.3.1.3)	[16]	0.76	-0.36	1.9	40	$800 \times 425\,\mu m$	21-40	In Plane
		[17]	17	3.7	1.21	30	$460 \times 260\,\mu m$	41-60	In Plane
		[18]	0.30	0.02	1.07	20	$1\,mm^2$	61-80	In Plane
		[19](a)	6.1	1.45	1.24	120	-	41-60	In Plane
		[19](b)	4.3	-1	1.30	90	-	41-60	In Plane
		[20](a)	2.09	-1.89	8.04	35	$8.78\,mm^2$	81-100	In Plane
		[20](b)	17.59	-2.9	1.20	35	$8.78\,mm^2$	81-100	In Plane
	Non-interdigitated (2.3.1.4)	[21](c)	2.6	-2.69	∞[d]	56.6	$730 \times 500\,\mu m$	61-80	In Plane
		[21](d)	2.6	5.2	3	72.1	-	81-100	In Plane
Mechanical *	Effective length (2.3.2.1)	[22]	3.2	17.7[c]	6.6	240	$775 \times 375\,\mu m$	61-80	In Plane
	Mechanical springs (2.3.2.2)	[23]	0.01	0.09[c]	10	130	$500 \times 650\,\mu m$	61-80	In Plane
Stressing effects □	Thermal (2.3.4.2)	[24](a)	0.2	0.22	2.1	6	$2600 \times 2100\,\mu m$	0-20	In Plane
		[24](b)	0.2	-0.04	1.25	6	$2600 \times 2100\,\mu m$	0-20	In Plane
		[24](c)	0.69	0.8	2.15	-	-	0-20	In Plane
Young's modulus ♦	(2.3.5)	[25]	84.1	-1.84	1.02	7.7	$1300 \times 1450\,\mu m$	0-20	In Plane

* Estimated from provided data
[a] Deflecting beam only
[c] Discrete system
[d] Experiments show zero stiffness after tuning

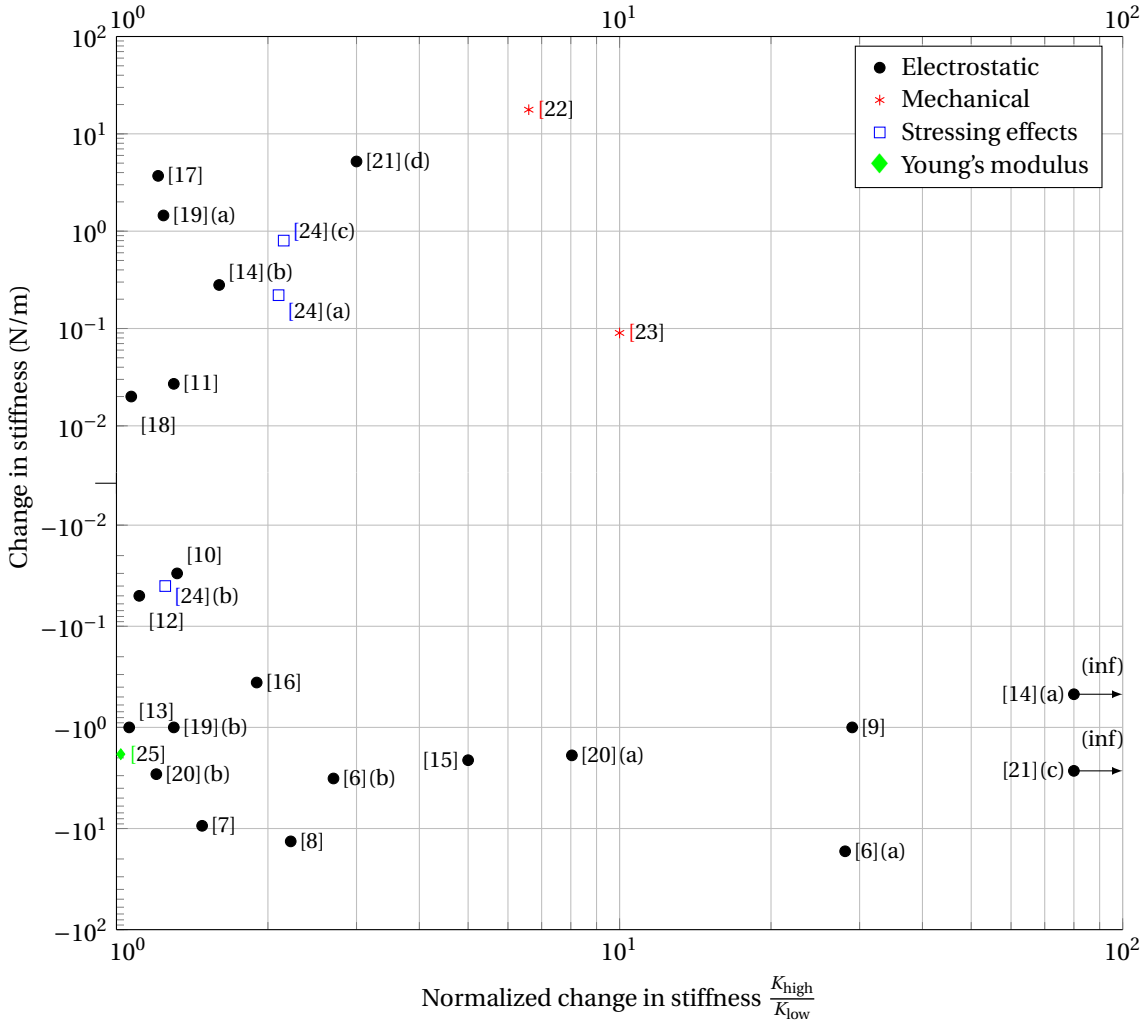

Figure 2.1: Change in stiffness versus normalized change in stiffness. The normalized stiffness is the largest achievable stiffness k_{high} divided by the lowest achievable stiffness k_{low}. The vertical axis is the change in stiffness, which can be positive or negative depending on whether the stiffness is higher or lower than the initial stiffness respectively. Devices that combine a large change in stiffness with a low normalized change in stiffness have a large untuned stiffness. Devices that combine a low change in stiffness with a large normalized change in stiffness have a low untuned stiffness. This figure provides insight in the stiffness tuning capabilities of the described devices. It provides a tool for designers of MEMS that require stiffness tuning to select a concept or suitable method that matches with the intended stiffness tuning range. Other important properties like size, relative size of the tuning mechanisms, tuning voltage and the direction of motion are shown in table 2.2. The numbers used in the graph correspond to the ones used in that table, and the references of this article. The colors and symbols represent devices that use the same physical principle. Devices [14](a) and [21](c) approach zero stiffness, so the normalized stiffness goes to infinity.

2.3.1. ELECTROSTATIC

Electrostatic stiffness adjustment relies on the fact that electrostatic forces are strong on micro scale, compared to other forces like gravity and inertial forces. In general, these concepts comprise a moving mass that is suspended by flexures. Electrodes are attached to the moving mass and are in close proximity to stationary electrodes. By applying a voltage between the stationary and moving electrodes, it is possible to exert a force on the mass. The electrodes will move, such that the electrostatic forces are in equilibrium with the mechanical restoring forces. In this new equilibrium, the stiffness has changed compared to its original state. There are four configurations of adding an electrostatic stiffness to a system: parallel plate (section 2.3.1.1), varying gap method (section 2.3.1.2), varying surface method (section 2.3.1.3) and non-interdigitated comb fingers (section 2.3.1.4). Furthermore nano-resonators with electrostatic stiffness tuning are discussed under parallel plate mechanisms (section 2.3.1.1). The theory behind the four configurations is explained in the corresponding sections.

2.3.1.1. ELECTROSTATIC: PARALLEL PLATE.

Two capacitive plates, separated by gap g_0, a potential difference V and an overlapping surface $A = (a_0 + x)b_0$, are shown in figure 2.2. The bottom plate is fixed, and the top plate can move in both x and y direction. The capacitance between two electrodes is defined as:

$$C = \frac{\epsilon(a_0 + x)b_0}{g_0 - y} \tag{2.4}$$

The amount of energy U, stored between capacitive plates can be calculated with:

$$U = \frac{1}{2}CV^2 \tag{2.5}$$

The force on the top plate can be found by taking the derivative of the energy with respect to the direction of interest. The stiffness is found by taking the derivative of this force.

$$\begin{aligned} F_x &= \frac{\partial U(x)}{\partial x}\Big|_y \\ &= \frac{1}{2}\frac{\epsilon b_0}{g_0}V^2 \end{aligned} \tag{2.6}$$

$$K_x = \frac{\partial F_x(x)}{\partial x} = 0 \tag{2.7}$$

$$\begin{aligned} F_y(y) &= \frac{\partial U(y)}{\partial y}\Big|_x \\ &= \frac{1}{2}\frac{\epsilon a_0 b_0}{(g_0 - y)^2}V^2 \end{aligned} \tag{2.8}$$

$$\begin{aligned} K_y(y) &= \frac{\partial F_y(y)}{\partial y} \\ &= \frac{\epsilon a_0 b_0}{(g_0 - y)^3}V^2 \end{aligned} \tag{2.9}$$

When a voltage is applied to the system, the parallel plates will move such that there is an equilibrium between the electrostatic attraction and mechanical restoring force. Around this new equilibrium position the stiffness is determined by sum of the mechanical- and electrostatic stiffness. The two capacitive plates have a (non-linear) stiffness in the y-direction, but have zero stiffness in x-direction. This electrostatic stiffness in y-direction is used in the parallel plate devices. Because the electrostatic stiffness is in the opposite direction of the mechanical restoring force it is commonly called a 'negative'-stiffness. (For a positive displacement in y, the electrostatic force increases positively, while the mechanical restoring force increases negatively).

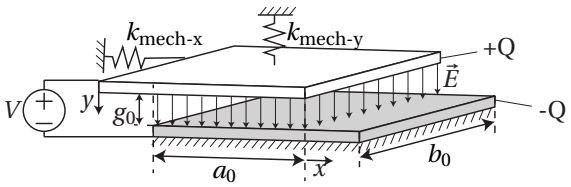

Figure 2.2: Two conductive plates, that have overlapping surface $A = (a_0 + \Delta a)b$, gap g_0, with a potential difference V. The charges ($+Q$ and $-Q$) accumulate on the plates and forms the electric field $\vec{E}$. The bottom plate is fixed, and the top plate can move in x and y direction. Mechanical springs are attached to the top plate.

The amount of electrostatic force and stiffness depend on the surface area, as shown in equations (2.6-2.9). So in order to have a significant effect without the need to further increase the voltage, the surface of the electrodes is often increased by applying as comb-like design as shown in figure 2.3.

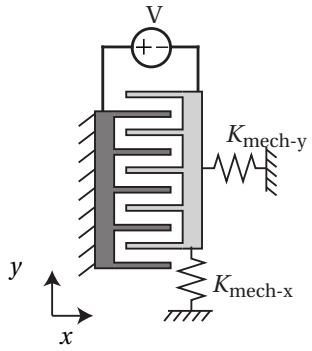

Figure 2.3: Two capacitive plates with combs to increase the surface area.

Parallel plate electrostatic tuning was by Adams *et al.* [6]. The device is shown in figure 2.4. A tuning voltage is applied between the stationary and moving plates of the capacitor. With this design, a device with a resonance frequency of 21 kHz was reduced to 7.7 % of its nominal value. The estimated mass of the system is 1.0×10^{-9} kg. So the mechanical stiffness of system can be calculated by using equation (2.1). This gives a stiffness of $17.41\,\mathrm{N\,m^{-1}}$. The measured electrostatic stiffness coefficient k_e^0 is $-7.9 \times 10^{-3}\,\mathrm{N\,m^{-1}\,V^{-2}}$, so for a tuning voltage of approximately 46 V (estimated from figure 2.5), this gives an electrostatic stiffness of:

$$k_{elec} = k_e^0 \cdot V^2 \qquad (2.10)$$
$$= -16.59\,\mathrm{N\,m^{-1}}$$

More devices were presented in this paper and are discussed later in this section, in section 2.3.1.2 and 2.3.1.3. Each device is separately mentioned in table 2.2. The parallel plate design is marked with **(a)**. The measurement results of these four devices can be found in figure 2.5.

A similar device was presented by Horsley *et al.* [7]. A parallel plate comb drive adds an electrostatic stiffness of $-9.4\,\mathrm{N\,m^{-1}}$ to the mechanical suspension of $29\,\mathrm{N\,m^{-1}}$. Parallel plate tuning was also applied by Torun *et al.* [8], to tune the stiffness of a membrane that is used for force spectroscopy applications. The stiffness was reduced from $24.4\,\mathrm{N\,m^{-1}}$ to $11\,\mathrm{N\,m^{-1}}$.

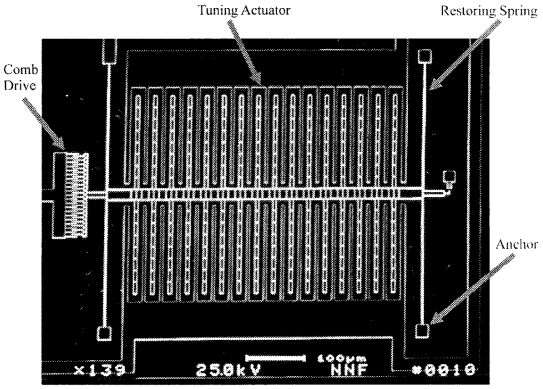

Figure 2.4: SEM image of the mechanical oscillator with a symmetric, parallel-plate actuator. A comb drive and a displacement indicator are attached to the outer sides of the left and right restoring springs, respectively. Reprinted from [6]. © IOP Publishing. Reproduced with permission. All rights reserved.

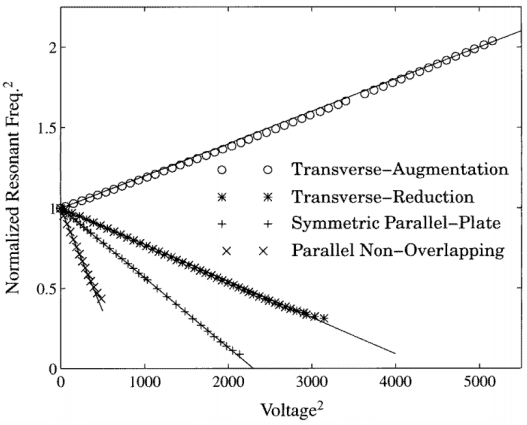

Figure 2.5: Experimental data for all four tuning actuators. The solid lines are least-squares fits to the first 10% of each data set. Normalizations are based on each oscillator's individual resonance frequency. Reprinted from [6]. © IOP Publishing. Reproduced with permission. All rights reserved.

The parallel plate tuning mechanism of figure 2.4 has a limited range of motion. When the gap between the stationary and moving electrodes becomes too small, the electrostatic attraction forces will become larger than the mechanical restoring force. The plates will collide and destroy the device. In order to increase the range of motion, Adams *et al.*[6] applied parallel plate tuning with a branched finger design instead of

having straight fingers, as shown in figure 2.6. When the position of the mass changes, the suspended combs move into the entrance region of the stationary combs. In order to achieve a linear behavior in positive and negative moving directions, a symmetric setup is used, such that the comb fingers will penetrate an entrance region in both directions of motion. The range of motion is increased from 0.8 µm to 1.3 µm compared to the previous design, while the efficiency remained approximately equal. The untuned resonance frequency is 7.5 kHz and the mass is 2.3×10^{-9} kg. So the mechanical stiffness of the system is $5.1\,\mathrm{N\,m^{-1}}$ according to equation (2.1). The experimental electrostatic stiffness is $-6.3 \times 10^{-3}\,\mathrm{N\,m^{-1}\,V^{-2}}$, resulting in a change in stiffness of $-3.2\,\mathrm{N\,m^{-1}}$ for $500\,\mathrm{V^2}$ which is estimated from figure 2.5. A similar design was presented by Park *et al.* [9]. The untuned- and tuned resonance frequency are 5.12 kHz and 0.950 kHz respectively. The theoretical proof mass weight is 1 µg, so this yields an untuned stiffness of $1.03\,\mathrm{N\,m^{-1}}$ and a tuned stiffness of $0.04\,\mathrm{N\,m^{-1}}$ for a tuning voltage of 10 V.

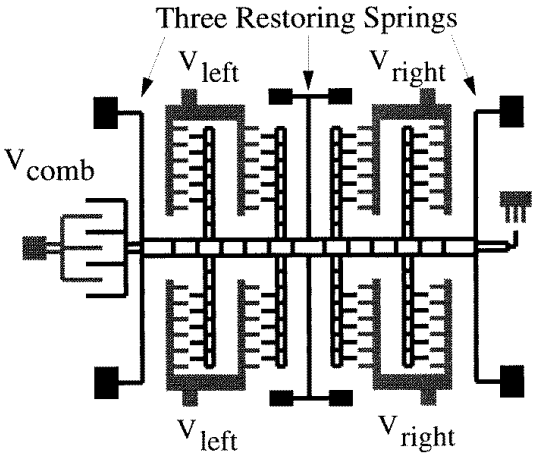

Figure 2.6: Schematic diagram of the parallel-reduction tunable oscillator. Reprinted from [6]. © IOP Publishing. Reproduced with permission. All rights reserved.

Parallel plate tuning has been applied in a MEMS gyroscope by Sonmezglu *et al.* [26]. The gyroscope has two vibrating modes (in x- and y-direction, in plane) and the resonance frequencies of these modes should be as close as possible. But due to manufacturing errors or temperature influences, there is usually a mismatch between these resonance frequencies. So by tuning the stiffness in one of these modes, the frequency can be tuned, such that it matches the other mode. A normalized change in stiffness of 1.30 is achieved, according to equation (2.3).

Parallel plate stiffness tuning is also applied without the commonly used comb structures. Yao *et al.* [27] and Evoy *et al.* [28] used flat electrodes under a suspended out of plane resonator to apply electrostatic softening. Zhao *et al.* [29] developed a micromirror, that has two torsional modes, and one translational mode of which the stiffness can be reduced with electrostatic softening. The device is shown in figure 2.7. The stiffness in z-direction is $0.1338\,\mathrm{N\,m^{-1}}$ and has a corresponding resonance frequency of 1150 Hz. This can be reduced to approximately 1000 Hz, which corresponds to $0.10\,\mathrm{N\,m^{-1}}$, according to equation (2.3). The torsional stiffness of the device can be tuned using the same tuning electrodes.

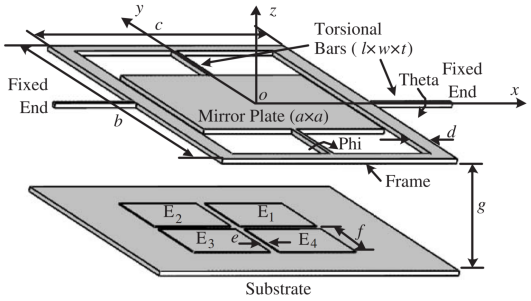

Figure 2.7: 3D model of dual-axis micromirror. The micromirror is suspended with the torsional beams. The electrodes $E_1 - E_4$ are used to tune the stiffness of the system. Reprinted from [10], with permission from Elsevier.

Nano-resonators Nano resonators are very small MEMS devices that often operate in the order of megahertz (MHz), or even gigahertz (GHz). These devices are for example being applied in the field of ultra-sensitive mass sensing [30–32] and radio frequency signal processing [33]. The resonators are usually doubly clamped structures, as shown in figure 2.8. The resonating structure can either be a micro fabricated beam or an even smaller structure such as a carbon nanotube or graphene flake. Some of these nano resonators

also have stiffness tuning capabilities. The common tuning method for this class of devices is parallel plate tuning. But instead of having dedicated structures that cover the stiffness tuning like discussed in the previous paragraph, the resonator itself serves as tuning electrode. The substrate of the device is commonly used as the tuning electrode. Just like the devices discussed in section 2.3.1.1, an electrostatic (negative) stiffness can be added to the system. One device is discussed as an example for these type of devices. Other devices that use the same tuning method were reported by Schwab *et al.* [11], Kwon *et al.* [34], Lopez *et al.* [35], Yan *et al.* [36], Stiller *et al.* [37] and Wu *et al.* [38].

Piazza *et al.* [39] reported on quality factor enhancement and capacitive fine tuning of resonators. The device is intended as a high quality factor MEMS resonator for on-chip filtering and frequency reference. The resonance frequency of the device can be tuned by applying a voltage between the substrate and the device layer. The ZnO layer is a piezoelectric layer. By applying a voltage between the drive electrode and the device layer, a vibration can be induced. The vibration of the device can be sensed by measuring the voltage on the sense electrode. The configuration of the device is shown in figure 2.8. The untuned frequency of the device is 719 kHz and for a tuning voltage of 20 V the resonance frequency decreases with 6 kHz. There is insufficient data available to determine the stiffness of the system.

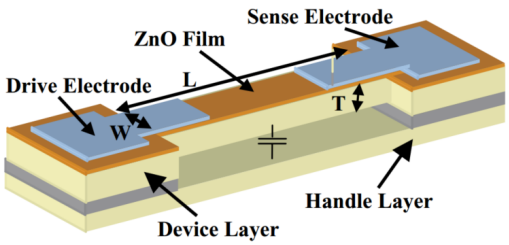

Figure 2.8: Voltage-tunable, piezoelectrically-transduced single crystal silicon resonators. Reprinted from [39], with permission from Elsevier.

Some of these nano resonators have the capability to tune the stiffness both positively as negatively in the same device. However, the positive stiffness tuning is for the resonance mode which is perpendicular to the mode of the negative stiffness tuning. An electrode is placed along the side of the resonator, in the same plane. When a voltage is applied between this electrode and the resonator, a negative stiffness is added to the in plane motion. This voltage also has the effect that the resonator is pulled into the direction of the electrode, due to the electrostatic forces. This force induces a tensile stress in the resonator. When the beam vibrates in the out of plane mode, this tensile stress causes a stiffening effect. This effect is explained in section 2.3.4. This method of both positive and negative stiffness tuning has been applied by Fung *et al.* [40], Pandey *et al.* [41], Rieger *et al.* [42], Solanki *et al.* [43], Fardindoost *et al.* [44] and Kozinsky *et al.* [45]. The last one is discussed in more detail as an example.

Kozinsky *et al.* [45] presented a device with an electrostatic mechanism to tune the nonlinearity of a resonator, increase the dynamical range and that can tune the resonance frequency. A theoretical model was developed that can serve as a design guideline, and a device was fabricated. This section only goes into the details of the frequency tuning capabilities. The device consists of a clamped-clamped beam with dimensions of 150 nm × 100 nm × 15 µm. A gate electrode is placed 400 nm from this beam and covers almost the entire length as shown in figure 2.9. This electrode can apply a DC bias voltage and an AC actuation voltage. The resonance frequency of both in-plane and out-of-plane were measured. When the gate electrode exerts a DC voltage to the resonator, both the in-plane and the out-of-plane frequencies change. Two different mechanisms are responsible for the change in stiffness. For the in-plane resonating mode the resonance frequency will decrease, because the electrostatic force will add a negative stiffness. The untuned resonance frequency of the in-plane motion is 8.78 MHz and can decrease with 6% for a tuning voltage of approximately 28 V (estimated from figure 2.9). This corresponds to an increase of 12% in stiffness according to equation (2.3). For the out of plane mode the resonance frequency will increase as a result of induced stress in the beam. The gate electrode can exert a force on the resonator, resulting in tensile stress in the beam. The untuned resonance frequency is 7.60 MHz and for

a tuning voltage of approximately 30 V the resonance frequency increases with 4%. This corresponds to an increase of 8% in stiffness according to equation (2.3).

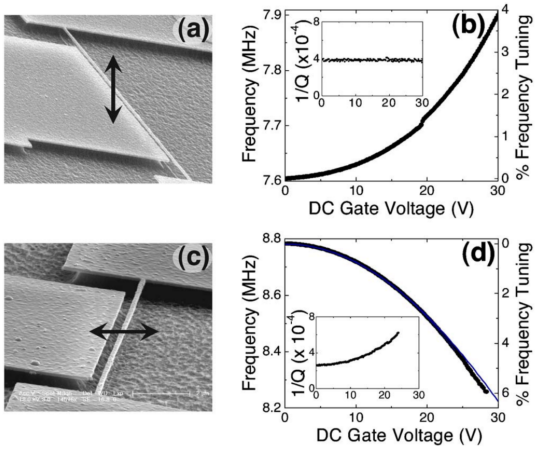

Figure 2.9: Elastic tuning of frequency upward (b) for the beam's vibration out of plane with the gate (a). Capacitive tuning of frequency downward (d) for vibration in-plane of the gate (c). The blue curve in (d) is the prediction of the theoretical model for the capacitive frequency tuning. Reprinted with permission from [45]. Copyright 2002, AIP Publishing LLC.

2.3.1.2. ELECTROSTATIC: VARYING GAP

The concepts in this section are similar to the parallel plate devices of section 2.3.1.1. The comb structure is commonly applied and the stiffness is added by applying a voltage between a moving and a stationary electrode. But the direction of motion is perpendicular compared to the parallel plate devices (x-direction instead of y, for figure 2.2). If we look at equation (2.7), it was shown that no electrode stiffness can be added in this direction for two flat, parallel electrodes. However, by having a gap $g(x)$ that is a function of the displacement in x, a stiffness can be added to the system. This is illustrated in figure 2.10. The equation governing the stiffness can be derived as:

$$\mathrm{d}C = \frac{\epsilon\,\mathrm{d}A}{g(x)} = \frac{\epsilon b_0\,\mathrm{d}x}{g(x)} \tag{2.11}$$

$$C = \epsilon b_0 \int_0^{a_0+x} \frac{\mathrm{d}x}{g(x)} \tag{2.12}$$

$$\begin{aligned} F_\mathrm{x}(x) &= \frac{\partial U(x)}{\partial x}\Big|_y \\ &= \frac{\epsilon b_0 V^2}{2}\frac{\partial}{\partial x}\int_0^{a_0+x}\frac{\mathrm{d}x}{g(x)} \\ &= \frac{\epsilon b_0 V^2}{2g(a_0+x)} \end{aligned} \tag{2.13}$$

$$\begin{aligned} K_\mathrm{x}(x) &= \frac{\partial F_\mathrm{x}(x)}{\partial x} \\ &= \frac{\epsilon b_0 V^2}{2}\frac{\partial g(a_0+x)}{\partial x} \end{aligned} \tag{2.14}$$

Because the capacitance now is a function of the motion in x-direction, the derivative of the force term does not become zero and yield a non-zero stiffness. By tailoring the gap shape, the force-deflection relation (stiffness) can be chosen by design.

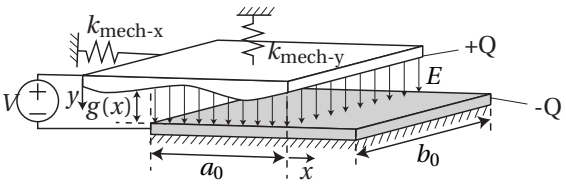

Figure 2.10: Two conductive plates, that have overlapping surface $A = (a_0+x)b_0$, gap $g(x)$, with a potential difference V. The charges ($+Q$ and $-Q$) accumulate on the plates and forms the electric field $\vec{E}$. The bottom plate is fixed, and the top plate can move in x and y direction.

This method was applied to a number of devices. The first notion on variable gap comb drive was in the context of actuators [46–48]. Later this was applied to stiffness tuning mechanisms. Jensen *et al.* [14] applied the method to a comb-finger structure. Seven shapes of comb fingers were designed of which two were fabricated and tested. The shape of the fingers was different, but were applied in the same device. One of the fabricated designs has a shape such that the system becomes stiffer ((a) in table 2.2) under an applied voltage, the other fabricated one becomes more compliant ((b)) in table 2.2). The schematic drawings of the stiffening (a) and weakening (b) comb shapes can be seen in figure 2.11. When the gap becomes smaller for a displacement x, $\frac{\partial g(x)}{\partial x}$ is negative, resulting in a negative stiffness. The opposite applies to gaps that become larger for a displacement x. The stiffness was tuned from $0.47\,\mathrm{N\,m^{-1}}$

to 0 N m^{-1} with the weakening fingers for 80 V and to 0.75 N m^{-1} with the stiffening fingers for 90 V.

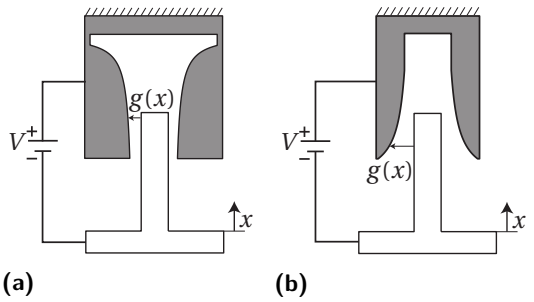

Figure 2.11: Schematic drawings of the weakening (a) and stiffening (b) comb shapes. The gap size changes with displacement x so the electrostatic force is a function of the displacement. [14].

The same concept was applied by Engelen *et al.* [12], that developed a musical instrument using MEMS technology with stiffness tuning capabilities. The device consists out of several similar resonators, that differ in mass and spring constant and thus (untuned) resonance frequency. Because the softest device has the largest normalized change is stiffness, this device is included in table 2.2 and figure 2.1. The theoretical stiffness is 0.6 N m^{-1}. The resonance frequency of this device decreases approximately 5% for a tuning voltage of 29 V, so the normalized change in stiffness is 1.11 according to equation (2.3).

The device of Lee *et al.* [15] applies the same method. The nominal stiffness of the device is 2.64 N m^{-1}. By applying a tuning voltage up to 150 V, this stiffness can be decreased by 80% to 0.53 N m^{-1}.

Varying shape electrodes were similarly applied by Guo *et al.* [13]. The untuned stiffness is 17.3 N m^{-1} and the linear electrostatic stiffness is -2.8×10^{-4} N m^{-1} V^{-2}. For a tuning voltage of 60 V this results in a change of -1 N m^{-1}.

2.3.1.3. Electrostatic: Varying overlapping surface.

In equation (2.7) it was shown that it was not possible to generate a stiffness in x-direction for flat parallel plates. In that case, the second derivative of the energy $U(x)$ with respect to x will be equal to zero (so there is no electrostatic stiffness). But when a comb drive is designed such that the overlapping surface A has a higher order dependency on the displacement (x^n with $n \geq 2$), the second derivative of the energy with respect to x will not be equal to zero. There will be an electrostatic stiffness in x-direction. The equations for the capacitance, electrostatic force and stiffness yield:

$$C(x) = \frac{\epsilon A(x)}{g_0} \tag{2.15}$$

$$F_x(x) = \frac{\partial U(x)}{\partial x}\Big|_y \tag{2.16}$$

$$= \frac{\epsilon V^2}{2g_0}\frac{\partial}{\partial x}A(x)$$

$$k_x(x) = \frac{\partial F_x(x)}{\partial x} \tag{2.17}$$

$$= \frac{\epsilon V^2}{2g_0}\frac{\partial^2}{\partial x^2}A(x) \tag{2.18}$$

So if $\partial^2 A(x)/\partial x^2 \neq 0$, there is an electrostatic stiffness in x-direction. This non-linearly varying overlapping electrode surface can be achieved by using a comb drive with fingers of varying length. This concept was first applied by Lee *et al.* [18]. Later, Dai *et al.*[16], Scheibner *et al.*[20, 49], Shmulevich *et al.*[50] and Kao *et al.*[17] used the same method. This type of tuning comb is shown in figures 2.12 and 2.13. The electrostatic stiffness k_{el} as presented by Kao *et al.* can be calculated as:

$$k_{el} = \frac{N\epsilon H t_h (b+x)}{2Bpdx}V^2 \tag{2.19}$$

with N the number of combs, ϵ the permittivity, t_h is the thickness of the device, and H, b, B, p and d geometric properties that can be found in figure 2.12. A device with a theoretical untuned stiffness of 17 N m^{-1} was fabricated. Under a tuning voltage of 30 V the stiffness increased with 21% to 20.6 N m^{-1}.

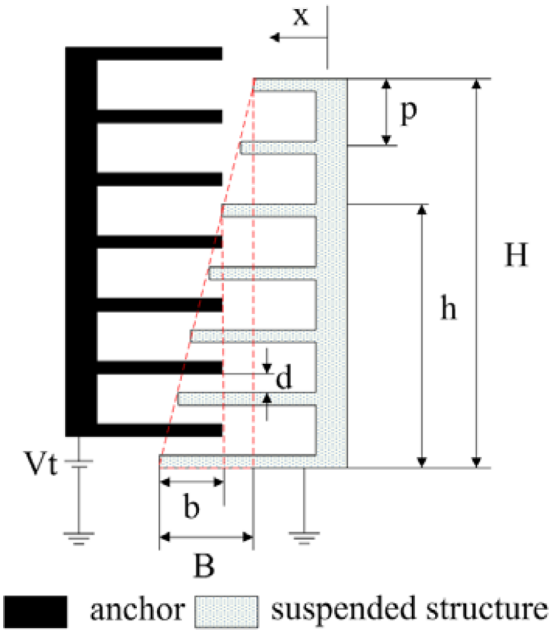

Figure 2.12: Tuning-comb of the tunable resonator. Reprinted from [17], used under the terms of the Creative Commons Attribution 4.0 license.

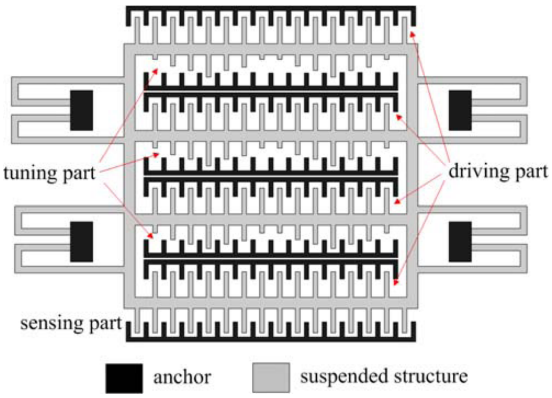

Figure 2.13: Schematic structure of the tunable resonator. Reprinted from [17], used under the terms of the Creative Commons Attribution 4.0 license.

Scheibner *et al.* [20, 49] used varying length comb fingers in a 'wide range tunable resonator'. The purpose of the device is to recognize the wear state in machinery, by checking the mechanical vibrations. It consist of an array of eight cells, such that a total range of 1 kHz to 10 kHz is covered. Each cell in the array has a fixed base frequency, which can be decreased by applying a tuning voltage. The tuning ranges of each subsequent cell are overlapping, so that no gap will occur in the total bandwidth. In table 2.2 cell one (a) and eight (b) are included as separate devices. Cell one has a theoretical untuned stiffness of $2.09\,\mathrm{N\,m^{-1}}$, the theoretical stiffness of cell eight is $17.59\,\mathrm{N\,m^{-1}}$. To approximate the tuned stiffness of the two cells the ratio between the measured tuned- and theoretical untuned resonance frequencies are used (as described in equation (2.3)). This results in a tuned stiffness of $0.2\,\mathrm{N\,m^{-1}}$ and $14.7\,\mathrm{N\,m^{-1}}$ for cell one and eight respectively. These two extremes are included in table 2.2 and figure 2.1 as (a) and (b) respectively.

Dai *et al.* [16] presented a similar device with a (theoretical) untuned stiffness of $0.76\,\mathrm{N\,m^{-1}}$. For a tuning voltage of 40 V, the stiffness drops to $0.4\,\mathrm{N\,m^{-1}}$. Shmulevich *et al.* [50] achieved a linear broad range of stiffness tuning with a similar device. The stiffness of the device was not presented, but the resonance frequency was changed from 957 Hz to 173 Hz for a tuning voltage of 81 V, resulting in a normalized change in stiffness of 30.6 according to equation (2.3). Lee *et al.* [18], that were the first to developed this tuning method achieved tuning from $0.3\,\mathrm{N\,m^{-1}}$ to $0.28\,\mathrm{N\,m^{-1}}$.

A different approach was chosen by Morgan *et al.* [19]. Instead of having varying comb finger lengths, the vertical dimension of the comb fingers was varied. This is illustrated in figure 2.14. These structures could be manufactured due to 'gray-scale' technology, that allows the fabrication of varying height structures with a single lithography and dry etch step. Both positive and negative tuning can be achieved, by designing the combs such that the overlapping surface decreases or increases respectively. Several designs were presented and those with the largest positive (a) and negative (b) tuning range were added to table 2.2. The largest positive change in stiffness is from $6.1\,\mathrm{N\,m^{-1}}$ to $7.55\,\mathrm{N\,m^{-1}}$ for 120 V and the largest negative stiffness tuning was from $4.3\,\mathrm{N\,m^{-1}}$ to $3.3\,\mathrm{N\,m^{-1}}$ for 90 V.

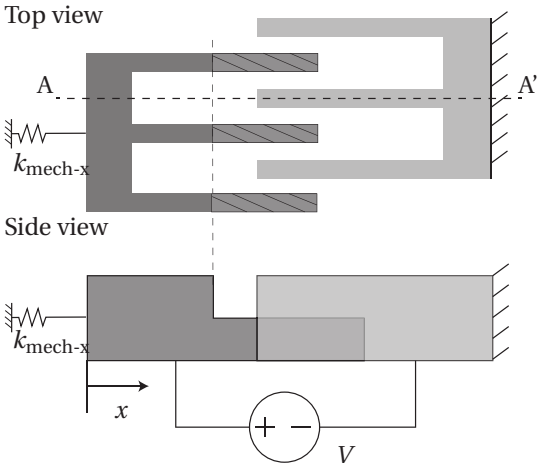

Figure 2.14: Comb fingers with varying height that result in a electrostatic stiffness. [19]

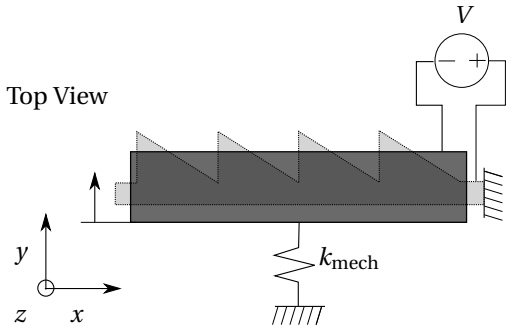

Figure 2.15: Topview of the triangular tuning electrodes as applied by Hu *et al.* [51]. The triangular electrodes are situated below the electrode that is connected to the proof mass. By applying a voltage between the electrodes, an electrostatic stiffness can be added to the system. The shape of the triangluar electrodes influences the stiffness.

A varying overlapping electrode surface was applied to a MEMS gyroscope by Hu *et al.* [51]. A proof-mass is brought into resonance in x-direction. The resonance frequency in y-direction should be the same as in x-direction, such that a rotation of the device results in a transfer of energy from the actuated resonance mode (x-direction) into the sensing direction (y-direction) due to the Coriolis effect. But due to manufacturing errors the resonance frequencies of the in-plane modes do not match. Stiffness tuning is used to change the resonance frequency in y-direction such that it matches the frequency of the mode in x-direction. The tuning electrodes are placed below the electrodes that are connected to the proof mass. The tuning electrodes are triangularly shaped, as shown in figure 2.15, such that the overlapping surface changes non-linearly when the top electrode moves in y-direction. The stiffness is determined by the shape of the electrodes. The resonance frequency is tuned from 1.984 kHz to 2.005 kHz for a tuning voltage of 17.5 V.

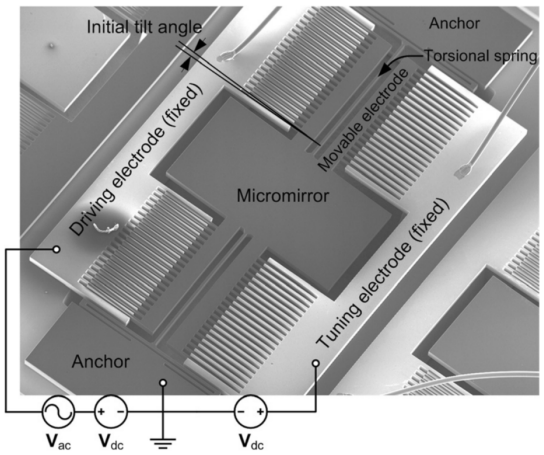

Figure 2.16: The microscanner consists of a rotor, two torsional springs, and two fixed electrodes. The single-crystal silicon torsional springs are plastically deformed such that the rotor including the micromirror and movable comb finger electrode has an initial tilt angle with respect to the stator electrodes. Two electrically isolated fixed electrodes including a driving electrode for actuation and a tuning electrode for tuning of the resonant frequency are symmetrically placed on both sides of the rotor with respect to the torsional springs. Reprinted from [52], used under the terms of the Creative Commons Attribution 4.0 license.

A varying overlapping electrode surface was applied in a angular vertical comb drive by Eun *et al.* [52]. A torsional micro mirror is suspended

by two torsional springs. Perpendicular to the springs a comb structure is applied that overlaps with stationary electrodes. When the micro mirror rotates, the overlapping surface between the moving and stationary electrodes changes nonlinearly. This adds a torsional stiffness to the system. The architecture of the device can be found in figure 2.16. The unmodified resonance frequency of 3176 Hz was tuned to 3066 Hz for a tuning voltage of 30 V.

2.3.1.4. ELECTROSTATIC: NON-INTERDIGITATED COMB FINGERS

The previous electrostatic tuning mechanisms of sections 2.3.1.1 to 2.3.1.3 were based on overlapping comb fingers. It is possible though to use non-interdigitated comb fingers for stiffness tuning. These comb fingers do not overlap and use fringe fields to exert a displacement-depending force on each other. Due to the complexity of these fringe fields, it is not possible to derive an analytical equation for the electrostatic stiffness. Finite element modeling is needed to find this electrostatic stiffness. Both positive and negative stiffness tuning can be achieved, depending on the initial alignment of the fingers.

This method of stiffness tuning was applied by Adams *et al.* [6, 21]. The device is shown in figure 2.17. For these transverse non-overlapping comb drive it's possible to have either a positive or a negative electrostatic stiffness, depending on the initial alignment of the comb fingers. When the initial alignment of the fingers is such that a moving finger is in between two stationary fingers, the restoring force will decrease with a displacement. This adds a negative stiffness to the system (denoted as (b) in table and graph). When the fingers of the stationary- and moving part are aligned, a relative motion will cause a restoring force. This is a positive electrostatic stiffness (c). Both these configurations are applied in a similar device; only the initial alignment is different. These initial configurations are illustrated in figure 2.18. This device has also been used by Zhang *et al.* [53] to research nonlinearity effects on an auto-parametric amplification. The theoretical untuned stiffness of the mechanical mechanism is $2.6\,\mathrm{N\,m^{-1}}$. The experimental electrostatic stiffnesses are $-0.84\times10^{-3}\,\mathrm{N\,m^{-1}\,V^{-2}}$ and $1.0\times10^{-3}\,\mathrm{N\,m^{-1}\,V^{-2}}$ for the reduction and augmentation system respectively. The tuning voltage squared is estimated from figure 2.5 to be $3200\,\mathrm{V^2}$ and $5200\,\mathrm{V^2}$ respectively, resulting in a change of stiffness of $-2.69\,\mathrm{N\,m^{-1}}$ and $5.2\,\mathrm{N\,m^{-1}}$. DeMartini *et al.* [54] applied the same tuning method, for both positive as negative stiffness tuning, but insufficient data was presented to determine the change in stiffness. The device was based on earlier work of Rhoads *et al.* [55].

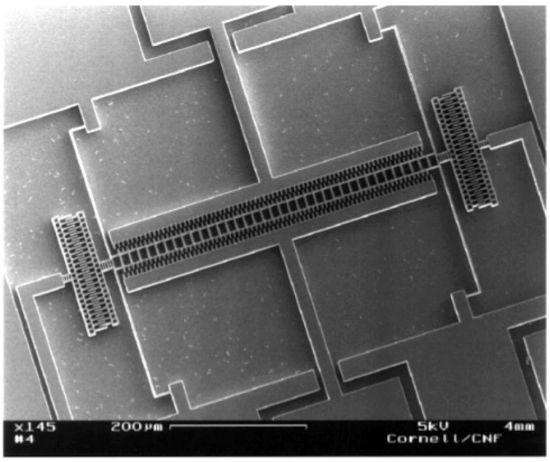

Figure 2.17: SEM image of a tunable resonator with a transverse(-reduction) actuator. Reprinted from [6]. © IOP Publishing. Reproduced with permission. All rights reserved.

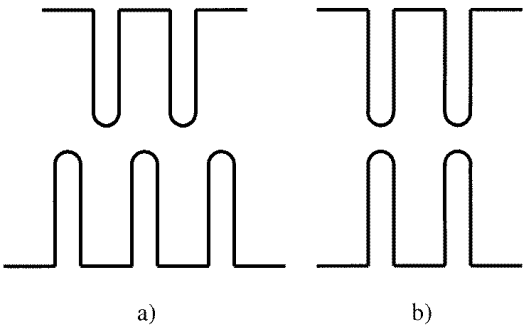

Figure 2.18: Diagram of the transverse non overlapping comb drive designs: (a) transverse reduction, (b) transverse augmentation. The lower halves are fixed in place and the upper halves are constrained to move horizontally. Reprinted from [6]. © IOP Publishing. Reproduced with permission. All rights reserved.

2.3.2. MECHANICALLY

The stiffness of a system can be adjusted by mechanically changing the suspension. In MEMS this suspension usually consists out of several flexural beams, that suspend parts of the chip. The stiffness of these beams is determined by the geometry, material properties and boundary conditions. The influence of the boundary conditions is shown in figures 2.19a and 2.19b. A cantilever, that is clamped at one side and free at the other is shown in figure 2.19a. When the beam is clamped at both ends, the situation is as shown in figure 2.19b. The stiffness is increased four times. The stiffness of a suspended system can be increased by engaging more of these flexures, or changing the effective length.

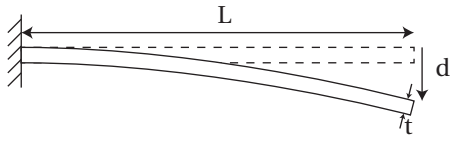

(a) Cantilever beam (see: equation (2.20)).

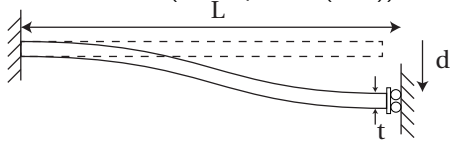

(b) Doubly clamped beam (see: equation (2.21)).

Figure 2.19: Beam in two configurations: cantilever and doubly clamped. The stiffness is a function of Young's modulus E, second moment of inertia I and length L.

$$k_{\text{cant}} = \frac{3EI}{L^3} \tag{2.20}$$

$$k_{\text{dcb}} = \frac{12EI}{L^3} \tag{2.21}$$

2.3.2.1. MECHANICALLY: CHANGE EFFECTIVE LENGTH.

Kafumbe *et al.* [56] used the pull-in of a cantilever beam to change the effective length and tune the stiffness of the system. The configuration of the design is shown in figure 2.20. An electrode is placed closely to a cantilever. By applying a voltage between the cantilever and electrode, the cantilever will start bending towards the electrode. This corresponds to state 1 in figure 2.20. At a critical point, the cantilever will snap in towards the electrode and a dielectric layer on top of the electrode prevents a short circuit. The snap in occurs when the electrostatic forces exceed the mechanical restoring forces of the cantilever. The cantilever is now in a stable clamped-pinned state (state 2). In this state the stiffness decreases for an increasing voltage. This results in a second unstable state after which the cantilever will move into the clamped-clamped configuration, which corresponds with state 3 in figure 2.20. If the voltage is further increased, the contact area between the cantilever and insulative layer will start to increase. This results in a change in effective length, so that the stiffness is changed. When the tuning voltage is decreased once the cantilever is snapped-in, there will be a hysteresis in the system, due to stiction between the cantilever and dielectric layer. Several mechanisms are responsible for the change in stiffness: adding electrostatic stiffness (state 1 and 2), change of boundary conditions (from state 1 to state 2 and state 2 to state 3) and change in effective length (state 3). The device has a long, linear operational range in state 3. The device is intended to work in this state. The change in normalized resonance frequency for the applied normalized voltage for the different stages is shown in figure 2.21.

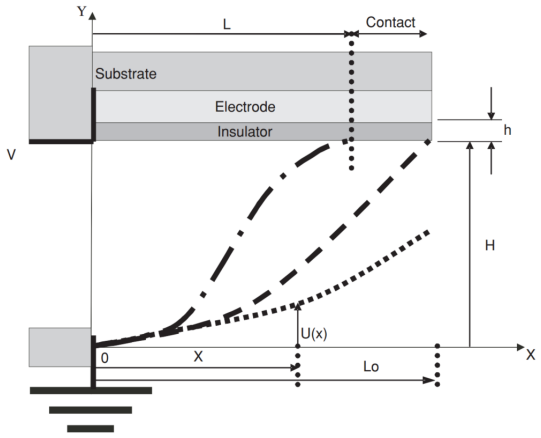

Figure 2.20: System configuration and states. State 1 is represented by (····), state 2 by (- - - -) and state 3 by (—·—). Reprinted from [56]. © IOP Publishing. Reproduced with permission. All rights reserved.

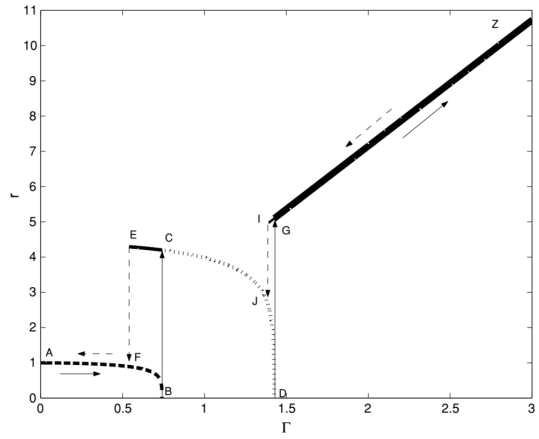

Figure 2.21: Normalized frequency variation with both increasing (A → B → C → D → G → Z), and decreasing normalized actuation voltage (Z → I → J → E → F → A) for the states 1 (- - - -), 2 ((·····) and —) and 3 (—). Reprinted from [56]. © IOP Publishing. Reproduced with permission. All rights reserved.

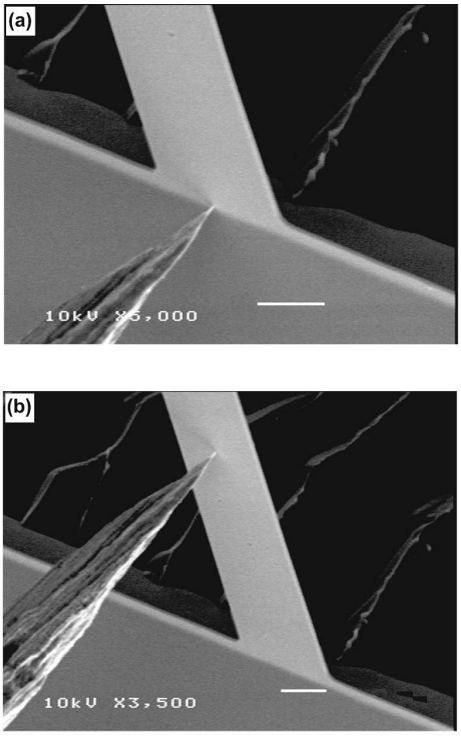

Figure 2.22: Scanning electron micrographs (scale bar corresponds to 10 µm) of the silicon nitride cantilever with the STM tip engaged at the base (a) and 45 µm away from the base of the cantilever (b). Plot (c) shows the corresponding resonant peaks acquired from the intensity of the secondary electrons (video signal). Reprinted with permission from [57]. Copyright 2000, AIP Publishing LLC.

Another device that uses the principle of length change for stiffness adjustment is presented by Zalalutdinov *et al.* [57]. A Scanning Tunneling Microscope (STM) is used to locally actuate and constrain a silicon nitride cantilever. The vertical motion of the STM is actuated by an AC voltage signal on the piezo drive, which is used to drive the cantilever. The force between the STM tip and cantilever provides an actuation and motion constraint. By changing the position where the STM tip engages the cantilever, the effective length is changed. This results in a stiffness and resonance frequency change. A change in resonance frequency of 300% is reported. The engagement of the STM tip with the cantilever can be seen for two different spots on the cantilever in figure 2.22. The first image (a) is actuated at the base of the cantilever, the second (b) at 45 µm from the base. The resulting change in resonance frequency can be seen in part (c) of the image. There is insufficient data provided to calculate the stiffness of this system.

Zine-El-Abidine *et al.* [22] developed an electrostatic comb resonator with adjustable stiffness by using the change in effective length. The device is

shown in figure 2.23. This device moves in-plane, and its position can be determined by measuring the capacitance between the moving and stationary fingers. By changing the effective length of the suspension beams the stiffness of the system changes. This change in effective length is achieved by electrostatic attraction of the suspension beams along a curved electrode as shown in figure 2.24. By applying a sufficiently large voltage between the electrode and the beam, the beam will be pulled in. In order to prevent a short circuit between the suspension beams and electrodes, silicon dioxide stoppers are used. These stoppers are insulated from the electrodes and will be the only contact points with the beam. There are three states in which the system can operate: zero sets activated, one set activated and two sets activated (In order to keep the system symmetrical it is only possible to actuate an entire set of actuators and not just one beam). The bias voltage that was used is 240 V. When an actuator is activated the effective length changes from 300 µm to 160 µm. The thickness of the structure is 25 µm and the width of the beams is 2 µm. Simple beams on the same die have been used to test the Young's modulus (107 GPa). The stiffness has been calculated using equation (2.21). The stiffness of the system in the three different configurations can be found in table 2.3. The maximum change in stiffness is used in table 2.2 and figure 2.1.

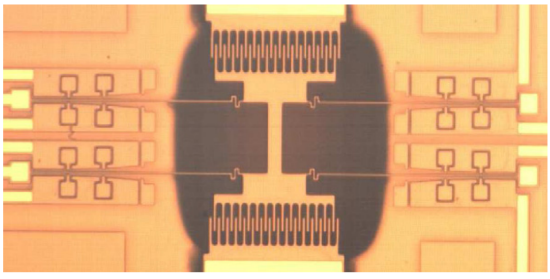

Figure 2.23: The fabricated electrostatic comb resonator with the MEMS actuators with curved electrodes. Reprinted from [22]. © IOP Publishing. Reproduced with permission. All rights reserved.

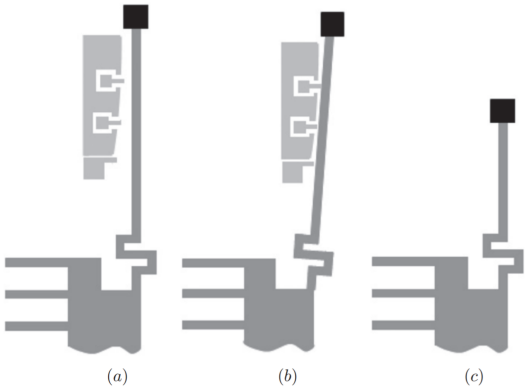

Figure 2.24: (a) The spring state at zero voltage. (b) The spring state when the actuator is under bias. (c) The equivalent spring. Reprinted from [22]. © IOP Publishing. Reproduced with permission. All rights reserved.

Table 2.3: Theoretical stiffness for the different configurations. (Not provided in original paper)

Configuration	Theoretical Stiffness (N/m)
Zero bias	3.2
Two actuators	12.0
Four actuators	20.9

2.3.2.2. MECHANICALLY: ENGAGING EXTRA SPRINGS

Mueller-Falcke *et al.*[23, 58] proposed a mechanical way to add stiffness to a system. The application of this device is scanning probe microscopy. Usually, a cantilever is used in scanning probe applications, but instead of using a cantilever that moves out of plane, an in plane motion was used. The device has two operating modes; a soft- and a stiff mode. In the soft mode, the probe is suspended by two pairs of flexure beams (flexure 1 and 3). By applying a voltage of 130 V a third pair of flexure beams (flexure 2) can be engaged, see figures 2.25 and 2.26. When these flexures are engaged, the probe is in stiff mode. The device covers an area of 500 µm × 650 µm. The proposed design has an unadjusted stiffness of 0.01 $\mathrm{N\,m^{-1}}$ and an adjusted stiffness of 0.1 $\mathrm{N\,m^{-1}}$.

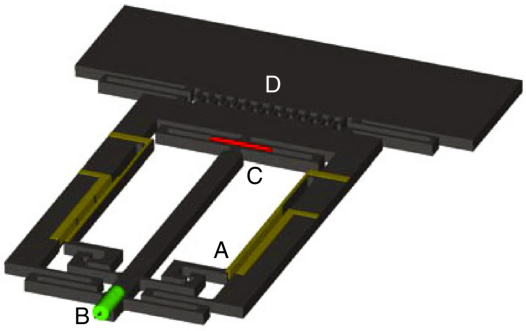

Figure 2.25: In-plane probe design (A, electrostatic clutch; B, high aspect ratio carbon nanotube tip; C, capacitive sensor; D, comb-drive actuator). Reprinted from [58]. © IOP Publishing. Reproduced with permission. All rights reserved.

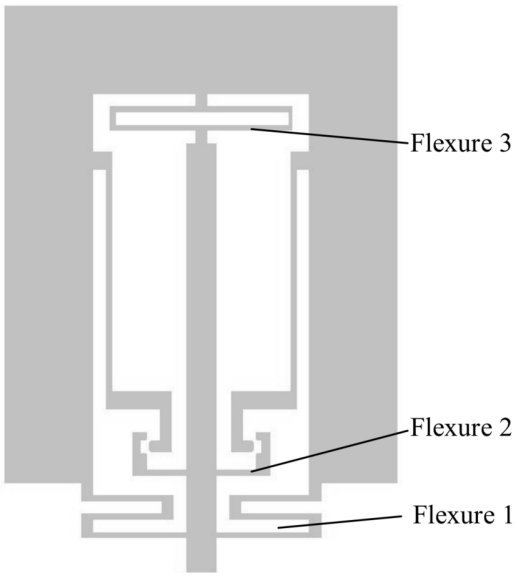

Figure 2.26: Plain structure of the AFM probe without sensors, actuators, tip. Reprinted with permission from [23].

2.3.3. CHANGE SECOND MOMENT OF INERTIA

The stiffness of a beam depends on its material properties, length, boundary conditions and cross section as shown in figures 2.19a and 2.19b. The influence of the cross section is described with the second moment of inertia I. The general expression of the second moment of inertia for an arbitrary shape, with respect to the x-axis:

$$I_x = \iint_A y^2 \, \mathrm{d}x \, \mathrm{d}y \tag{2.22}$$

For a simple rectangular beam this is defined as:

$$I = \frac{w t^3}{12} \tag{2.23}$$

Where w and t are the width and thickness respectively. From these equations it can be concluded that a small part of surface area of $\mathrm{d}x\,\mathrm{d}y$ contributes more to the second moment of inertia and stiffness when it is further away from the center. Deforming the cross-section results in a change of the second moment of inertia. This results in a change in stiffness. By deforming the cross section such that the surface area moves further away from the center a stiffer system is obtained. This method is applied by Kawai *et al.* [59]. It is applied to an Atomic Force Microscope (AFM) cantilever that can be used to analyze the mass of atoms and molecules. First, a surface is scanned with the cantilever in AFM mode in order to find a certain molecule or atom. This requires a stiff cantilever. When the atom or molecule is found, it is picked up with the tip of the cantilever and it is ejected in a TOF mass analyzer. But in order to reach for the TOF mass analyzer, the probe must undergo a large deflection. The high stiffness of the cantilever is disadvantageous in this case, since it requires a lot of force. In order for the cantilever to switch from a soft state to a stiff state, a piezoelectric layer is used to deform the cross sectional shape, as shown in figure 2.27. The longitudinal piezoelectric layers are used to bend the cantilever upwards, while the transverse piezoelectric part is used to modify the cross section of the probe. By applying a voltage to the piezoelectric layer it contracts, while the underlying layer resists this contracting motion. Due to this difference in contraction, bending will occur. A schematic figure of the device and the procedure of operation can be seen in figure 2.27. The stiff mode is 14% more stiff than the neutral mode.

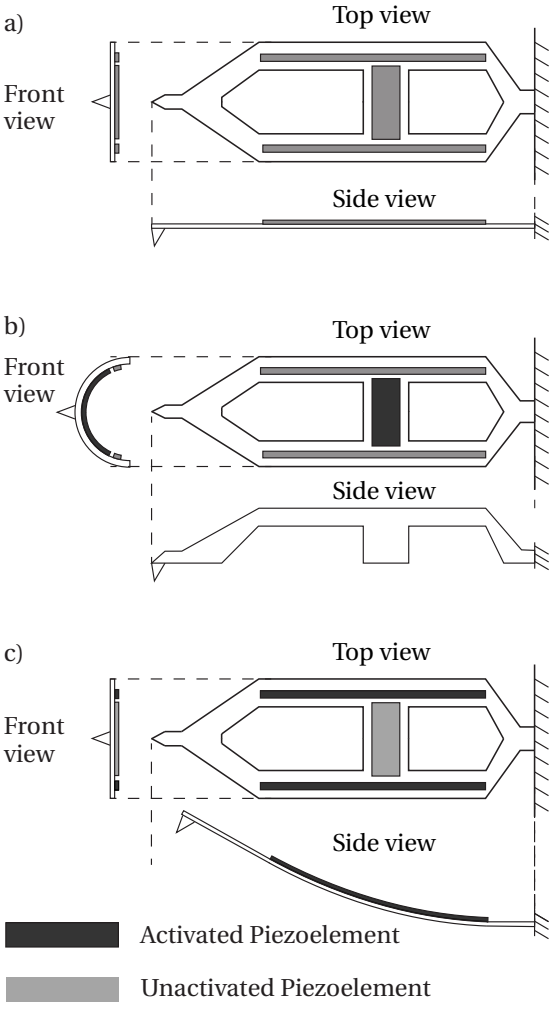

Figure 2.27: Schematic figure of the probe. In state a) the probe is in its undeformed shape. In b) the piezoelement in the center is activated and the probe deforms into a U-shape. This is the stiff mode. In c) the probe is in soft mode and uses the two longitudinal piezo actuators on the side to bend upwards [59].

2.3.4. STRESSING EFFECTS

The stiffness of an element is influenced by stressing effects. Both a positive and a negative change in stiffness can be achieved by applying either a tensile or compressive load respectively. The effects of induced stress can be seen in the result of micro fabrication process [60–62], due to differences in thermal expansion coefficients between subsequent layers and stresses that are inherent to the deposition processes. This is usually an unwanted effect and often the cause of failure in MEMS. Stressing effects can also be caused by adsorption of (bio-)molecules [63–69] and is used in sensing applications. These devices will not be included in this review, because the change is stiffness is not controlled, but the effect is used for sensing. Stressing effects can also be used to change the stiffness in a controlled way. The stress can for instance be applied by thermal expansion, piezoelectric effects or electrostatic loads. These methods is discussed in sections 2.3.4.1 to 2.3.4.3. As was already mentioned in the introduction of the review, systems that show stiffness changes due to dynamic effects will not be discussed, but might be of interest to the reader. There is a large group of devices that use non-linear dynamics for resonance frequency tuning [4, 5]. By increasing the resonance amplitude of a resonator, there will be a stiffening effect due to the increased stress. These devices will not be discussed, because this effect only occurs in a dynamic state. Nano-resonators that use both electrostatic softening and stressing effects were already discussed in section 2.3.1.1.

The effect of a uniform axial load on the stiffness can be understood by taking the dimensionless linear equation of motion for a beam element and dropping the damping terms and external forcing, as derived by Younis [70]. The shape of the beam is expressed by $w(x,t)$, where x is the position along the beam and t is time:

$$\frac{\partial^4 w}{\partial x^4} + \frac{\partial^2 w}{\partial t^2} - N_{\text{non}} \frac{\partial^2 w}{\partial x^2} = 0 \tag{2.24}$$

with $N_{\text{non}} = l^2 N/(EI)$ (positive N means tensile force, negative means compressive), where l, N, E and I are the length, load, Young's modulus and second moment of inertia respectively. The axial load only contributes to the spatial term, which shows its influence on the stiffness. For a uniform load, a tensile force is limited by the strength of the material, while compressive load is limited by the buckling limit of the beam. When the buckling load is reached, the stiffness approaches zero.

2.3.4.1. STRESSING EFFECTS: PIEZOELECTRIC STRESSING.

Piezoelectric materials show mechanical deformation when an electric field is applied [71]. This

deformation can be used to apply a stress to change the stiffness of a system.

Karabalin *et al.* [72] developed a new model to predict stiffness changes in micro- and nanocantilever beams due to surface stress. The validity of this model has been confirmed with measurements. The device is a single chip with series of both cantilevers with a free end and doubly clamped beams as shown in figure 2.28. All have the same width of 900 nm and have the same stack of materials: 20 nm aluminum nitride, 100 nm molybdenum, 100 nm aluminum nitride, and 100 nm molybdenum. The lengths are 6, 8 and 10 µm. A voltage is applied between the molybdenum layers, such that the aluminum nitride layer will apply a stress to the stack due to its piezoelectric properties. Both a compressive and a tensile stress can be applied. This stress causes the beam to bend, because it is applied above the neutral axis of the stack. An AC voltage to the same piezo stack is used for actuation. Interferometric measurements are used to detect the resonance frequency. In table 2.2 only the 10 µm doubly clamped beam is included, as two separate devices; one for positive tuning voltage (a) and one for negative tuning voltage (b). Similar experiments, with an off-center piezoelectric stack on a silicon nitride doubly clamped beam were done by Olivares *et al.* [73].

2.3.4.2. Stressing effect: Thermal expansion.

Most materials expand when the temperature is increased. It is a result of the increase in kinetic energy in the molecules. When a doubly clamped beam is subjected to an increase in temperature, the expansion of the material will lead to an increased internal stress, which can be used for stiffness tuning.

Two devices that made use of stressing effects by thermal expansion were presented by Syms *et al.* [24]. A one degree- (figure 2.29) and two degree of freedom device were made. The first device is explained in more detail. A mass is suspended by folded flexures and is tunable in the y-direction. This is done by applying a DC-voltage between the anchors of the flexures such that a current will start to flow. Due to Joule heating, these flexures will heat up. Whether compressive or tensile stress will arise depends on the ambient pressure. This is a result of the dominant cooling mechanism; under high pressure this is convection, while thermal conduction dominates at low pressures. When the cooling is dominated by convection, the temperature will be higher in the flexures than in the suspended part, because the surface of the latter is much greater, which results in a faster cooling. The thermal expansion will be larger in the flexures than in the suspended part, so compressive stress will arise. When the pressure is low, the convective cooling will be negligible and conduction to the bulk of the chip will be the dominant cooling mechanism. The flexures and the suspended parts will have the same uniform temperature in steady state. Now the thermal expansion of the suspended part will be larger, since it is longer than the flexures; the flexures will be under tensile stress. For a compressive stress, the stiffness will decrease, while a tensile stress will result in an increased stiffness. The unadjusted stiffness of the device is not mentioned in the paper, but can be derived from the geometry. The stiffness for such a set of doubly clamped beams is shown in equation (2.21). Assuming that the silicon has a Young's modulus of 169 GPa [74], this results in a stiffness of $k_{sys} = 0.2\,\mathrm{N\,m^{-1}}$. For the lowest pressure of 10 mTorr, the increase in resonance frequency is almost 50%, resulting in $0.45\,\mathrm{N\,m^{-1}}$. For the highest pressure of 500 mTorr, the decrease in resonance frequency is almost 10%, resulting in $0.16\,\mathrm{N\,m^{-1}}$. In table 2.2 the device is shown as two separate devices; one for the increase in stiffness(a), the other for the decrease in stiffness (b). The two degree of freedom device has a different flexure geometry. The mass is suspended by two sets of beams instead of one and the length of the beams is smaller compared to the other device. By using the equation of equation (2.21) we get $k = 0.69\,\mathrm{N\,m^{-1}}$. The resonance frequency in the y-direction changes from 1.56 kHz to 2.29 kHz for 3 mW of tuning power. By applying equation (2.3), a tuned stiffness of $1.49\,\mathrm{N\,m^{-1}}$ is found. This device can be found in table 2.2 as device (c).

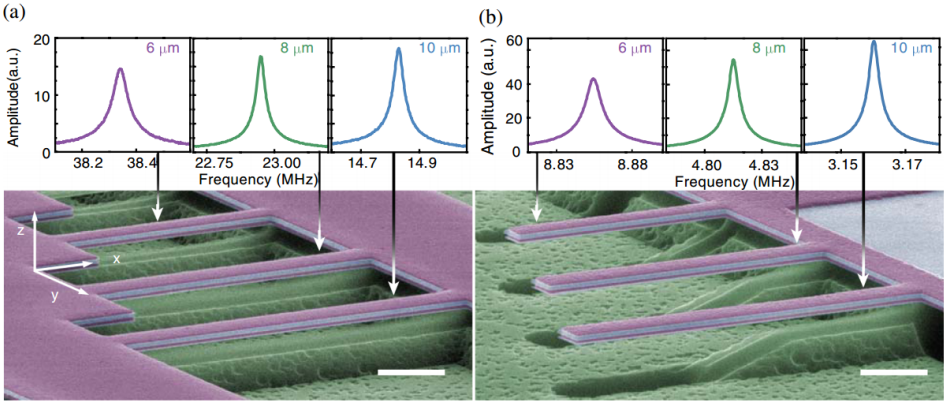

Figure 2.28: Resonant response of piezoelectric beams. a, SEM micrograph of the doubly clamped beams used for the experiments. On top of the micrograph, we show resonant responses of each of the beams, yielding resonant frequencies of 38.3 MHz (length 6 μm, purple), 22.9 MHz (8 μm, green) and 14.8 MHz (10 μm, blue). Experimental details are provided in the supplementary material of [72]. b, SEM micrograph of the cantilever beams used for the experiments. Respective resonant responses are also shown for each cantilever, yielding natural frequencies of 8.85 MHz (length 6 μm), 4.82 MHz (8 μm), 3.16 MHz (10 μm). Both types of beams have the same composition (320 nm of total thickness) and width (900 nm). Lengths are 6, 8, or 10 μm for both types of devices, causing the boundary conditions to be the only difference, thus allowing proper comparison of the experimental results for the two configurations. Scale bars: 2 μm. Reprinted with permission from [72]. Copyright by the American Physical Society.

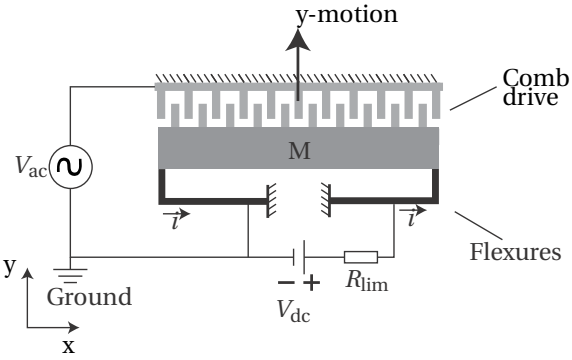

Figure 2.29: Schematic drawing of device with one degree of freedom. The mass is suspended by the folded flexures. A DC voltage can be applied to the flexures, and due to Joule heating the beams will heat up and expand. Depending on the surrounding air pressure, convective or conductive cooling will be dominant. For conductive cooling, the flexures will be subjected to tensile stress, because the mass expands more than the flexures. For convective cooling the flexures will expand more than the mass, resulting in a compressive stress. Compressive stress decreases the stiffness, tensile stress increases the stiffness. The AC voltage is used to actuate the device.[24]

The stiffness of the device designed by Remtema *et al.* [75] is tuned by thermally induced stressing effects. The configuration of the device can be seen in figure 2.30. A mass is suspended by 'beam 1' and by a folded flexure mechanism that consists of 'beam 2' and 'beam 3'. The folded flexure mechanism results in a high stiffness in x direction and a low (linear) stiffness in w direction. By applying a current to the suspension beams, the temperature will increase due to Joule heating and the beams will expand. The expansion of 'beam 2' and 'beam 3' is in opposite direction, so no compressive stress is developed. 'Beam 1' however, will be stressed due to the thermal expansion. This stress results in the change in stiffness. On top of the stressing effect there is a second mechanism that decreases the stiffness of the structure. The Young's modulus of silicon has a negative temperature dependency as is described in section 2.3.5; by increasing the temperature in the suspension beams both the compressive stress as the decrease in Young's modulus will decrease the stiffness. (Because the compressive stress has the dominant effect, the device is placed in this category). The results of the change in resonance frequency of the device can be seen in figure 2.31. The maximum change in frequency

is 14%, so according to equation (2.3), this is an increase of 30% in stiffness.

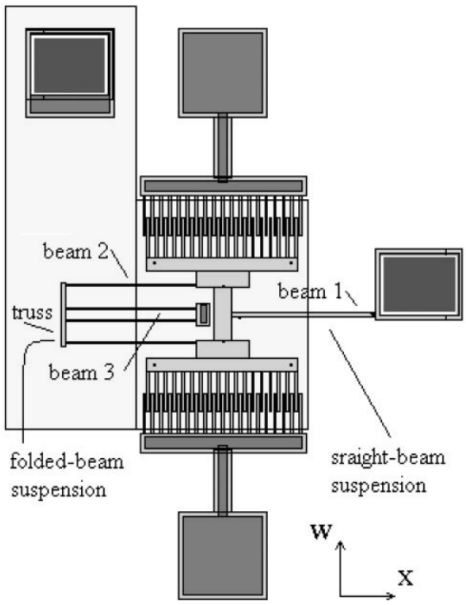

Figure 2.30: Schematic diagram of a comb-shape micro resonator with a straight-beam for active frequency tuning via localized stressing effects. Reprinted from [75], with permission from Elsevier.

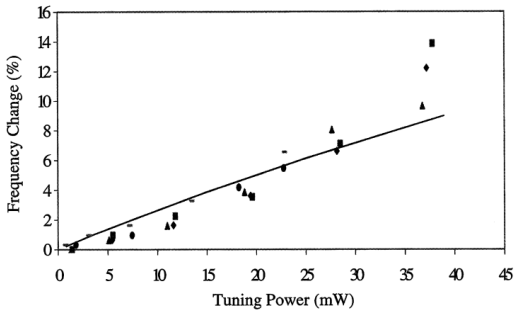

Figure 2.31: Measured frequency change versus tuning power for five different devices compared to the theoretical model. Reprinted from [75], with permission from Elsevier.

Previously discussed devices use uniform heating and uniformly thermal expansion by using the suspension beam itself as the heater. This requires an electrical conductive suspension beam. Sviličić *et al.* [76, 77] and Mastropaolo *et al.* [78] used non-uniform thermal expansion, by using a separate electro-thermal electrode on top of the structural element that supplies the thermal energy. So thermally induced stress can also be applied to non-conductive material. This method has been applied to a doubly clamped beam [76], a cantilever beam [77–81] and a disk [78]. In the case of a cantilever beam, the expansion not fully restricted. The thermal stress is induced due to the difference in thermal expansion coefficient between the electrode and the support material. This results in a stress gradient and out of plane bending of the structure.

Thermally induced stressing effects have also been applied on nano resonators. Jun *et al.* [82] used 12 µm long doubly clamped composite beams consisting of 30 nm 3C-SiC and 30-195 nm aluminum. A current was applied to the resonator itself, resulting in Joule heating and thermally induced stress. Mei *et al.* [83] used carbon nanotubes in similar experiments.

2.3.4.3. STRESSING EFFECT: ELECTROSTATIC FORCE.

Cabuz *et al.* [84] presented a MEMS resonator of which the stiffness can be tuned by using stressing effects. This stress is applied by using electrostatic attraction. A silicon structure with a thin, doubly clamped cantilever resonator is installed in a glass package, as shown in figure 2.32. One of the sides of the structure is clamped in, the other side is suspended by a torsion bar. Electrodes are situated close to the top and bottom of the free hanging part of the silicon structure. These electrodes can exert a force on the structure, such that the structure can rotate around the torsion bar. An axial force will be induced to the resonator. A third electrode is placed close to the resonator to detect the deflection of the resonator by capacitive measurement. The applied voltage attracts the bottom of the free end. This induces a tensile stress in the resonator, resulting in an increase of resonance frequency. For 15 V the frequency increased with 14.5 Hz. Tuning with the upper electrode is not demonstrated, but a similar change in frequency, in opposite direction may be expected. The untuned resonance frequency is not mentioned in the paper. Yao *et al.* [27] mentioned the use of electrostatic actuators for applying an axial force for stiffness tuning. No experi-

mental data was provided though.

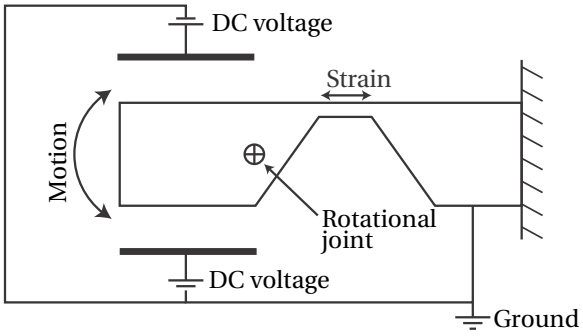

Figure 2.32: Schematic of device [84].

2.3.5. CHANGE YOUNG'S MODULUS

The stiffness of a mechanical structure is depending on the geometry, configuration and Young's modulus (elasticity of a material). Zhang *et al.* [85, 86] designed a device of which the stiffness can be changed by tuning the Young's modulus. A mass is suspended by four flexural beams that are connected to a crossbars as shown in figure 2.33. By applying a voltage to the electrodes of the device, a current will run through the crossbars and flexural beams. The flexural beams will heat up, due to Joule heating. The beams will expand, but this will not result in an axial stress, because the motion is not restricted due to the compliance of the crossbars. The flexural beams are made out of silicon, which has a negative temperature coefficient of modulus. The increase in temperature will therefore lead to a decrease in Young's modulus, and thus stiffness as shown in equations (2.20) and (2.21). Two sets of comb drives are attached to the mass. One of these comb drives is used to actuate the mass, the other is used to measure the motion. The untuned mechanical stiffness can be calculated using equation (2.21). For flexural beams with a size of ($l \times w \times t$) $410 \times 25 \times 7\,\mu$m and a Young's modulus at room temperature of 169 GPa, which gives $k_0 = 84.1\,\mathrm{N\,m^{-1}}$. For an input of 54 mW the resonance frequency drops 1.1%. According to equation (2.3) this means that the tuned stiffness is 97.8% of the untuned stiffness. The tuned stiffness is $82.25\,\mathrm{N\,m^{-1}}$. Devices that use thermally induced axial stress (section 2.3.4.2) usually have this effect of change in Young' modulus as well. But the effect on the change in stiffness is stronger for stressing effects than for the change in Young' modulus.

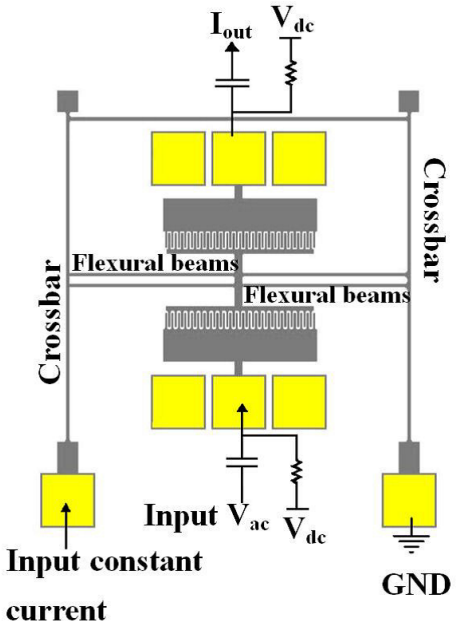

Figure 2.33: Schematic of MEMS resonator with integral crossbar heaters including biasing configuration used. Reprinted from [85], with permission from Elsevier.

2.4. DISCUSSION

The results will be discussed for each physical principle. They are compared in table 2.4.

2.4.1. ELECTROSTATIC

Electrostatic tuning is the most used method for stiffness tuning. It is very versatile; almost all ranges of stiffness can be achieved. But this all comes at a cost of size. The change in stiffness is directly related to the surface area of the electrodes. So in order to achieve large changes in stiffness, a large device is needed. The most simple way of electrostatic stiffness tuning is by using the '*parallel plate*' type (section 2.3.1.1). The range of motion of this device is limited by the risk of pull-in. This range can be extended by using branched fingers instead of straight ones. The risk of pull-in remains though, and precautions like safety pins or other mechanical stoppers are required to ensure a long lifetime [9].

Table 2.4: Comparison of the categories

		Stiffness adjustment					
Category	Sub-category	Positive	Negative	Continuous	Discrete	Advantages	Disadvantages
Electrostatic	Parallel plate	×	✓	✓	×	Simple, effective	Risk of pull-in, relative large tuning mechanism
	Varying gap	✓	✓	✓	×	Freedom of design	Risk of pull-in, relative large tuning mechanism
	Varying surface	✓	✓	✓	×	Freedom of design	Risk of pull-in, relative large tuning mechanism
	Non-interdigitated	✓	✓	✓	×	Low risk of colliding electrodes	Complex design, less efficient, relative large tuning mechanism
Mechanical	Effective length	×	×	✓	✓	Large tuning range	Mechanical contact and high voltage required
	Mechanical springs	×	×	×	✓	Large tuning range	Mechanical contact and high voltage required
Second moment of inertia		✓	×	✓	×	Size efficient solution, applicable to cantilever	
Stressing effects	Piezoelectric	✓	✓	✓	×	Positive and negative tuning in same device, applicable to cantilever, size efficient	
	Thermal	✓	✓	✓	×	Easily applicable, size efficient	Only small changes in stiffness
	Electrostatic	✓	✓	✓	×		Relatively large
Young's modulus		×	✓	✓	×	Relatively easily applicable	Only small changes in stiffness

The '*varying gap*' and '*varying overlapping electrode surface*' have more freedom of design than the '*parallel plate*' devices. The voltage-stiffness relation can be designed by choosing the rate of change in gap or overlapping electrode surface. This might enhance the performance.

Non-interdigitated comb fingers are less efficient than the other electrostatic tuning methods. The advantage is that the risk of colliding comb fingers is low, because they are not overlapping.

2.4.2. MECHANICAL

Mechanical tuning is an effective way of achieving large changes in stiffness for a limited device size. These devices are often discrete. This might be a limiting factor for certain applications. But when continuous stiffness tuning is not needed and a large change in stiffness is required, mechanical stiffness adjustment is a suitable method. Mechanical contact is inevitable for these methods, which could lead to stiction- and wear problems. Most of the devices that use mechanical tuning use electrostatic pull-in to establish the mechanical contact, which requires a high voltage.

2.4.3. SECOND MOMENT OF INERTIA

The second moment of inertia describes the influence of the cross section on the stiffness of an element. By deforming the cross section, the stiffness can be changed. There is only one device in this category in this review. It uses piezoelectric elements to control the cross-sectional curvature of a cantilever. not many tuning methods are applicable to cantilevers. The piezo actuator is very small because it is integrated in the structure. Therefor it is a size efficient solution.

2.4.4. STRESSING EFFECTS

Stressing effects can be applied by either piezoelectric elements, thermal expansion or by electrostatic forces. The piezoelectric devices can tune the stiffness both positively and negatively in a single device, because both tensile and compressive stresses can be developed, depending on the direction of the electric field. For this reason it is a versatile method. Thermal stressing can also

be used to tune both in the positive and negative direction, but this can not be done in the same device under constant conditions. When the thermal expansion of the suspension element is larger than the surrounding structure, the stress will be compressive. When the expansion of the suspension is lower than the surrounding structure, tensile stress will be present. Inducing stress through electrostatic forces can also be used for positive and negative stiffness tuning, depending on the actuation direction of the actuator. The tuning range of devices in this category is relatively small.

2.4.5. YOUNG'S MODULUS

The Young's modulus is the elasticity of a material, which influences the stiffness. The Young's modulus is depending on the temperature, so it can be tuned by controlling the temperature. The Young's modulus of silicon, which is widely used for MEMS, has a negative temperature dependency. However, the effect is weak and only small changes in stiffness can be achieved because the tuning is limited by the melting temperature. This tuning method is easily applicable, because a heater is the only additional part that is needed. Devices using thermal expansion for stressing effects also show stiffness change due to a change in the Young's modulus, but this effect is much stronger.

2.5. CONCLUSION

Stiffness adjustment is broadly applied in MEMS and the applications and physical principles are numerous. The results in this paper can be used as a selection tool for the reader to find a suitable concept for a new application. The categorization as it stands now can successfully map the current state of art, but might need extra categories or sub-categories if the field develops. The field of stiffness tuning is dominated by electrostatic methods and most of the applications can be found in resonating structures like accelerometers, energy harvesters and mechanical filters.

If a large tuning range is required (more than one order of magnitude), electrostatic tuning or mechanical tuning are the most suitable methods. Electrostatic tuning requires a large device though, and mechanical tuning is often in discrete steps and requires a large tuning voltage. If a small tuning range (up to one order of magnitude) is required electrostatic tuning, stressing effects, change in second moment of inertia or tuning of the Young's modulus could be a suitable method. Table 2.2 provides an overview of the different devices and their key properties. Figure 2.1 provides a graphical overview of the devices and their absolute and normalized change in stiffness. The different categories are compared in table 2.4. These graph and tables serve as a selection tool for stiffness tuning.

REFERENCES

[1] M. Winthrop, W. Baker, and R. Cobb, "A variable stiffness device selection and design tool for lightly damped structures," *Journal of Sound and Vibration*, vol. 287, pp. 667–682, nov 2005.

[2] D. Zhu, M. J. Tudor, and S. P. Beeby, "Strategies for increasing the operating frequency range of vibration energy harvesters: a review," *Measurement Science and Technology*, vol. 21, p. 022001, feb 2010.

[3] W.-M. Zhang, K.-M. Hu, Z.-K. Peng, and G. Meng, "Tunable Micro- and Nanomechanical Resonators.," *Sensors (Basel, Switzerland)*, vol. 15, no. 10, pp. 26478–566, 2015.

[4] R. M. C. Mestrom, R. H. B. Fey, K. L. Phan, and H. Nijmeijer, "Simulations and experiments of hardening and softening resonances in a clamped-clamped beam MEMS resonator," *Sensors and Actuators, A: Physical*, vol. 162, no. 2, pp. 225–234, 2010.

[5] V. Kaajakari, T. Mattila, A. Oja, and H. Seppa, "Nonlinear Limits for Single-Crystal Silicon Microresonators," *Journal of Microelectromechanical Systems*, vol. 13, pp. 715–724, oct 2004.

[6] S. G. Adams, F. M. Bertsch, K. A. Shaw, P. G. Hartwell, F. C. Moon, and N. C. MacDonald, "Capacitance based tunable resonators," mar 1998.

[7] D. a. Horsley, R. Horowitz, and A. P. Pisano, "Microfabricated electrostatic actuators for hard disk drives," *IEEE/ASME Transactions on Mechatronics*, vol. 3, no. 3, pp. 175–183, 1998.

[8] H. Torun, K. K. Sarangapani, and F. L. Degertekin, "Spring constant tuning of active atomic force microscope probes using electrostatic spring softening effect," *Applied Physics Letters*, vol. 91, no. 25, p. 253113, 2007.

[9] I. Park, C. Lee, H. Jang, Y. Oh, and B. Ha, "Capacitive sensing type surface micromachined silicon accelerometer with a stiffness tuning capability," in *Proceedings MEMS 98. IEEE. Eleventh Annual International Workshop on Micro Electro Mechanical Systems. An Investigation of Micro Structures, Sensors, Actuators, Machines and Systems (Cat. No.98CH36176)*, no. m, pp. 637–642, IEEE, 1998.

[10] Y. Zhao, F. E H Tay, G. Zhou, and F. Siong Chau, "A study of electrostatic spring softening for dual-axis micromirror," *Optik - International Journal for Light and Electron Optics*, vol. 117, no. 8, pp. 367–372, 2006.

[11] K. Schwab, "Spring constant and damping constant tuning of nanomechanical resonators using a single-electron transistor," *Applied Physics Letters*, vol. 80, no. 7, pp. 1276–1278, 2002.

[12] J. B. C. Engelen, H. de Boer, J. G. Beekman, L. C. Fortgens, D. B. de Graaf, S. Vocke, and L. Abelmann, "The Micronium—A Musical MEMS Instrument," *Journal of Microelectromechanical Systems*, vol. 21, pp. 262–269, apr 2012.

[13] C. Guo and G. K. Fedder, "A quadratic-shaped-finger comb parametric resonator," *Journal of Micromechanics and Microengineering*, vol. 23, no. 9, p. 095007, 2013.

[14] B. Jensen, S. Mutlu, S. Miller, K. Kurabayashi, and J. Allen, "Shaped comb fingers for tailored electromechanical restoring force," *Journal of Microelectromechanical Systems*, vol. 12, pp. 373–383, jun 2003.

[15] K. B. Lee, L. Lin, and Y.-H. Cho, "A closed-form approach for frequency tunable comb resonators with curved finger contour," *Sensors and Actuators A: Physical*, vol. 141, pp. 523–529, feb 2008.

[16] C.-L. Dai and W.-C. Yu, "A micromachined tunable resonator fabricated by the CMOS post-process of etching silicon dioxide," *Microsystem Technologies*, vol. 12, pp. 766–772, jul 2006.

[17] P.-H. Kao, C.-L. Dai, C.-C. Hsu, and C.-Y. Lee, "Fabrication and Characterization of a Tunable In-plane Resonator with Low Driving Voltage," *Sensors*, vol. 9, pp. 2062–2075, mar 2009.

[18] K. B. Lee and Y.-H. Cho, "A triangular electrostatic comb array for micromechanical resonant frequency tuning," *Sensors and Actuators A: Physical*, vol. 70, no. 1-2, pp. 112–117, 1998.

[19] B. Morgan and R. Ghodssi, "Vertically-Shaped Tunable MEMS Resonators," *Journal of Microelectromechanical Systems*, vol. 17, pp. 85–92, feb 2008.

[20] D. Scheibner, J. E. Mehner, B. Brämer, T. Gessner, and W. Dötzel, "Wide range tuneable resonators for vibration measurements," *Microelectronic Engineering*, vol. 67-68, pp. 542–549, jun 2003.

[21] S. Adams, F. Bertsch, K. Shaw, P. Hartwell, N. MacDonald, and F. Moon, "Capacitance Based Tunable Micromechanical Resonators," *Proceedings of the International Solid-State Sensors and Actuators Conference - TRANSDUCERS '95*, vol. 1, pp. 438–441, 1995.

[22] I. Zine-El-Abidine and P. Yang, "A tunable mechanical resonator," *Journal of Micromechanics and Microengineering*, vol. 19, p. 125004, dec 2009.

[23] C. Mueller-Falcke, Y.-A. Song, and S.-G. Kim, "Tunable Stiffness Scanning Microscope Probe," in *SPIE 5604, Optomechatronic Micro/Nano Components, Devices, and Systems* (Y. Katagiri, ed.), vol. 5604, pp. 31–37, oct 2004.

[24] R. R. A. Syms, "Electrothermal frequency tuning of folded and coupled vibrating micromechanical resonators," *Journal of Microelectromechanical Systems*, vol. 7, pp. 164–171, jun 1998.

[25] H. J. Zhang and C. J. Qiu, "Characterization and MEMS application of low temperature TiNi(Cu) shape memory thin films," *Materials Science and Engineering A*, vol. 438-440, pp. 1106–1109, nov 2006.

[26] S. Sonmezoglu, S. E. Alper, and T. Akin, "An automatically mode-matched MEMS gyroscope with wide and tunable bandwidth," *Journal of Microelectromechanical Systems*, vol. 23, no. 2, pp. 284–297, 2014.

[27] J. J. Yao and N. C. MacDonald, "A micromachined, single-crystal silicon, tunable resonator," sep 1999.

[28] S. Evoy, D. W. Carr, L. Sekaric, A. Olkhovets, J. M. Parpia, and H. G. Craighead, "Nanofabrication and electrostatic operation of single-crystal silicon paddle oscillators," *Journal of Applied Physics*, vol. 86, p. 6072, dec 1999.

[29] Y. P. Zhao, L. S. Wang, and T. X. Yu, "Mechanics of adhesion in MEMS—a review," *Journal of Adhesion Science and Technology*, vol. 17, pp. 519–546, jan 2003.

[30] B. Lassagne, D. Garcia-Sanchez, A. Aguasca, and A. Bachtold, "Ultrasensitive Mass Sensing with a Nanotube Electromechanical Resonator," *Nano Letters*, vol. 8, pp. 3735–3738, nov 2008.

[31] Q. Wang and B. Arash, "A review on applications of carbon nanotubes and graphenes as nano-resonator sensors," *Computational Materials Science*, vol. 82, pp. 350–360, feb 2014.

[32] K. Eom, H. S. Park, D. S. Yoon, and T. Kwon, "Nanomechanical resonators and their applications in biological/chemical detection: Nanomechanics principles," *Physics Reports*, vol. 503, pp. 115–163, jun 2011.

[33] C.-C. Nguyen, "Frequency-selective MEMS for miniaturized low-power communication devices," *IEEE Transactions on Microwave Theory and Techniques*, vol. 47, no. 8, pp. 1486–1503, 1999.

[34] Jihan Kwon, Jungwook Choi, Kwanoh Kim, Jaesam Sim, Jinho Kim, and Jongbaeg Kim, "Frequency Tuning of Nanowire Resonator Using Electrostatic Spring Effect," *IEEE Transactions on Magnetics*, vol. 45, pp. 2332–2335, may 2009.

[35] J. L. Lopez, J. Verd, A. Uranga, J. Giner, G. Murillo, F. Torres, G. Abadal, and N. Barniol, "A CMOS-MEMS RF-Tunable Bandpass Filter Based on Two High-Q 22-MHz Polysilicon Clamped-Clamped Beam Resonators," *IEEE Electron Device Letters*, vol. 30, pp. 718–720, jul 2009.

[36] Jize Yan, A. a. Seshia, K. L. Phan, and J. T. van Beek, "Internal electrical phase inversion for FF-beam resonator arrays and tuning fork filters," in *2008 IEEE 21st International Conference on Micro Electro Mechanical Systems*, vol. 2, pp. 1028–1031, IEEE, jan 2008.

[37] P. L. Stiller, S. Kugler, D. R. Schmid, C. Strunk, and a. K. Hüttel, "Negative frequency tuning of a carbon nanotube nano-electromechanical resonator under tension," *Physica Status Solidi (B) Basic Research*, vol. 250, no. 12, pp. 2518–2522, 2013.

[38] C. C. Wu and Z. Zhong, "Capacitive spring softening in single-walled carbon nanotube nanoelectromechanical resonators.," *Nano Letters*, vol. 11, no. 4, pp. 1448–51, 2011.

[39] G. Piazza, R. Abdolvand, G. K. Ho, and F. Ayazi, "Voltage-tunable piezoelectrically-transduced single-crystal silicon micromechanical resonators," *Sensors and Actuators A: Physical*, vol. 111, pp. 71–78, mar 2004.

[40] W. Y. Fung, E. N. Dattoli, and W. Lu, "Radio frequency nanowire resonators and in situ frequency tuning," *Applied Physics Letters*, vol. 94, no. 20, p. 203104, 2009.

[41] A. K. Pandey, "Effect of coupled modes on pull-in voltage and frequency tuning of a NEMS device," *Journal of Micromechanics*

and Microengineering, vol. 23, p. 085015, aug 2013.

[42] J. Rieger, T. Faust, M. J. Seitner, J. P. Kotthaus, and E. M. Weig, "Frequency and Q factor control of nanomechanical resonators," *Applied Physics Letters*, vol. 101, no. 10, p. 103110, 2012.

[43] H. S. Solanki, S. Sengupta, S. Dhara, V. Singh, S. Patil, R. Dhall, J. Parpia, A. Bhattacharya, and M. M. Deshmukh, "Tuning mechanical modes and influence of charge screening in nanowire resonators," *Physical Review B*, vol. 81, p. 115459, mar 2010.

[44] S. Fardindoost, A. Alipour, S. Mohammadi, S. Gokyar, R. Sarvari, A. Iraji zad, and H. V. Demir, "Flexible strain sensors based on electrostatically actuated graphene flakes," *Journal of Micromechanics and Microengineering*, vol. 25, no. 7, p. 075016, 2015.

[45] I. Kozinsky, H. W. C. Postma, I. Bargatin, and M. L. Roukes, "Tuning nonlinearity, dynamic range, and frequency of nanomechanical resonators," *Applied Physics Letters*, vol. 88, no. 25, p. 253101, 2006.

[46] M. A. Rosa, S. Dimitrijev, and H. B. Harrison, "Improved Operation of Micromechanical Comb-Drive Actuators through the Use of a New Angled Comb Finger Design," *Journal of Intelligent Material Systems and Structures*, vol. 9, pp. 283–290, apr 1998.

[47] Wenjing Ye, S. Mukherjee, and N. MacDonald, "Optimal shape design of an electrostatic comb drive in microelectromechanical systems," *Journal of Microelectromechanical Systems*, vol. 7, pp. 16–26, mar 1998.

[48] W. Ye and S. Mukherjee, "Design and Fabrication of an Electrostatic Variable Gap Comb Drive in Micro-Electro-Mechanical Systems," 2000.

[49] D. Scheibner, J. E. Mehner, D. Reuter, T. Gessner, and W. Dötzel, "A spectral vibration detection system based on tunable micromechanical resonators," *Sensors and Actuators, A: Physical*, vol. 123-124, pp. 63–72, sep 2005.

[50] S. Shmulevich, I. Hotzen, and D. Elata, "A perfect electrostatic anti-spring," in *2013 IEEE SENSORS*, no. 1, pp. 1–4, IEEE, nov 2013.

[51] S. Hu, Z. Jin, H. Zhu, H. Wang, and M. Ma, "A Slot-Structure MEMS Gyroscope Working at Atmosphere With Tunable Electrostatic Spring Constant," *Journal of Microelectromechanical Systems*, vol. 22, pp. 909–918, aug 2013.

[52] Y. Eun, J. Kim, and L. Lin, "Resonant-frequency tuning of angular vertical comb-driven microscanner," *Micro and Nano Systems Letters*, vol. 2, no. 1, p. 4, 2014.

[53] W. Zhang, R. Baskaran, and K. L. Turner, "Effect of cubic nonlinearity on auto-parametrically amplified resonant MEMS mass sensor," *Sensors and Actuators A: Physical*, vol. 102, pp. 139–150, dec 2002.

[54] B. E. DeMartini, J. F. Rhoads, K. L. Turner, S. W. Shaw, and J. Moehlis, "Linear and Nonlinear Tuning of Parametrically Excited MEMS Oscillators," *Journal of Microelectromechanical Systems*, vol. 16, pp. 310–318, apr 2007.

[55] J. F. Rhoads, S. W. Shaw, K. L. Turner, and R. Baskaran, "Tunable Microelectromechanical Filters that Exploit Parametric Resonance," *Journal of Vibration and Acoustics*, vol. 127, p. 423, oct 2005.

[56] S. M. M. Kafumbe, J. S. Burdess, and A. J. Harris, "Frequency adjustment of microelectromechanical cantilevers using electrostatic pull down," *Journal of Micromechanics and Microengineering*, vol. 15, pp. 1033–1039, may 2005.

[57] M. Zalalutdinov, B. Ilic, D. Czaplewski, A. Zehnder, H. G. Craighead, and J. M. Parpia, "Frequency-tunable micromechanical oscillator," *Applied Physics Letters*, vol. 77, no. 20, p. 3287, 2000.

[58] C. Mueller-Falcke, S. D. Gouda, S. S.-G. Kim, and S. S.-G. Kim, "A nanoscanning platform for bio-engineering: an in-plane probe with switchable stiffness.," *Nanotechnology*, vol. 17, pp. S69–S76, feb 2006.

[59] Y. Kawai, T. Ono, E. Meyers, C. Gerber, and M. Esashi, "Piezoelectric Actuator Integrated Cantilever with Tunable Spring Constant For Atom Probe," in *19th IEEE International Conference on Micro Electro Mechanical Systems*, no. January, pp. 778–781, IEEE, 2006.

[60] M. Kobrinsky, E. Deutsch, and S. Senturia, "Effect of support compliance and residual stress on the shape of doubly supported surface-micromachined beams," *Journal of Microelectromechanical Systems*, vol. 9, pp. 361–369, sep 2000.

[61] W. Fang and J. A. Wickert, "Comments on measuring thin-film stresses using bilayer micromachined beams," *Journal of Micromechanics and Microengineering*, vol. 5, pp. 276–281, dec 1995.

[62] A. Evans and J. Hutchinson, "The thermomechanical integrity of thin films and multilayers," *Acta Metallurgica et Materialia*, vol. 43, pp. 2507–2530, jul 1995.

[63] G. Yoshikawa, T. Akiyama, S. Gautsch, P. Vettiger, and H. Rohrer, "Nanomechanical membrane-type surface stress sensor.," *Nano letters*, vol. 11, pp. 1044–8, mar 2011.

[64] D. Ramos, J. Tamayo, J. Mertens, M. Calleja, and A. Zaballos, "Origin of the response of nanomechanical resonators to bacteria adsorption," *Journal of Applied Physics*, vol. 100, p. 106105, nov 2006.

[65] J. W. Ndieyira, N. Kappeler, S. Logan, M. A. Cooper, C. Abell, R. A. McKendry, and G. Aeppli, "Surface-stress sensors for rapid and ultrasensitive detection of active free drugs in human serum.," *Nature nanotechnology*, vol. 9, pp. 225–32, mar 2014.

[66] S. Cherian and T. Thundat, "Determination of adsorption-induced variation in the spring constant of a microcantilever," *Applied Physics Letters*, vol. 80, p. 2219, mar 2002.

[67] M. K. Ghatkesar, H.-P. Lang, C. Gerber, M. Hegner, and T. Braun, "Comprehensive characterization of molecular interactions based on nanomechanics.," *PloS one*, vol. 3, p. e3610, jan 2008.

[68] A. W. McFarland, M. A. Poggi, M. J. Doyle, L. A. Bottomley, and J. S. Colton, "Influence of surface stress on the resonance behavior of microcantilevers," *Applied Physics Letters*, vol. 87, p. 053505, jul 2005.

[69] K. S. Hwang, K. Eom, J. H. Lee, D. W. Chun, B. H. Cha, D. S. Yoon, T. S. Kim, and J. H. Park, "Dominant surface stress driven by biomolecular interactions in the dynamical response of nanomechanical microcantilevers," *Applied Physics Letters*, vol. 89, p. 173905, oct 2006.

[70] M. I. Younis, *MEMS Linear and Nonlinear Statics and Dynamics*, vol. 20 of *Microsystems*. Boston, MA: Springer US, 2011.

[71] B. Jaffe, *Piezoelectric Ceramics*. Elsevier Science, 2012.

[72] R. B. Karabalin, L. G. Villanueva, M. H. Matheny, J. E. Sader, and M. L. Roukes, "Stress-Induced Variations in the Stiffness of Micro- and Nanocantilever Beams," *Physical Review Letters*, vol. 108, p. 236101, jun 2012.

[73] J. Olivares, J. Malo, S. González, E. Iborra, I. Izpura, M. Clement, A. Sanz-Hervás, J. L. Sánchez-Rojas, and P. Sanz, "Tunable mechanical resonator with aluminum nitride piezoelectric actuation," vol. 6186, pp. 61860K–61860K–12, apr 2006.

[74] M. A. Hopcroft, W. D. Nix, and T. W. Kenny, "What is the Young's Modulus of Silicon?," *Journal of Microelectromechanical Systems*, vol. 19, pp. 229–238, apr 2010.

[75] T. Remtema and L. Lin, "Active frequency tuning for micro resonators by localized thermal stressing effects," *Sensors and Actuators A: Physical*, vol. 91, pp. 326–332, jul 2001.

[76] B. Sviličić, E. Mastropaolo, B. Flynn, and R. Cheung, "Electrothermally Actuated and Piezoelectrically Sensed Silicon Carbide Tunable MEMS Resonator," *IEEE Electron Device Letters*, vol. 33, pp. 278–280, feb 2012.

[77] B. Sviličić, E. Mastropaolo, R. Zhang, and R. Cheung, "Tunable MEMS cantilever resonators electrothermally actuated and

piezoelectrically sensed," *Microelectronic Engineering*, vol. 145, pp. 38–42, 2015.

[78] E. Mastropaolo, G. S. Wood, I. Gual, P. Parmiter, and R. Cheung, "Electrothermally Actuated Silicon Carbide Tunable MEMS Resonators," *Journal of Microelectromechanical Systems*, vol. 21, pp. 811–821, aug 2012.

[79] A. Rúa, R. Cabrera, H. Coy, E. Merced, N. Sepúlveda, and F. E. Fernández, "Phase transition behavior in microcantilevers coated with M1-phase VO2 and M2-phase VO2:Cr thin films," *Journal of Applied Physics*, vol. 111, p. 104502, may 2012.

[80] G. Zhang, L. Zhao, L. Xu, Z. Jiang, Y. Zhao, X. Wang, and Z. Liu, "Active Frequency Tuning for Magnetically Actuated and Piezoresistively Sensed MEMS Resonators," *IEEE Electron Device Letters*, vol. 34, pp. 921–923, jul 2013.

[81] N. Manca, L. Pellegrino, T. Kanki, S. Yamasaki, H. Tanaka, A. S. Siri, and D. Marré, "Programmable mechanical resonances in MEMS by localized joule heating of phase change materials.," *Advanced materials (Deerfield Beach, Fla.)*, vol. 25, pp. 6430–5, nov 2013.

[82] S. C. Jun, X. M. H. Huang, M. Manolidis, C. a. Zorman, M. Mehregany, and J. Hone, "Electrothermal tuning of Al–SiC nanomechanical resonators," *Nanotechnology*, vol. 17, no. 5, pp. 1506–1511, 2006.

[83] J. Mei and L. Li, "Frequency self-tuning of carbon nanotube resonator with application in mass sensors," *Sensors and Actuators B: Chemical*, vol. 188, pp. 661–668, 2013.

[84] C. Cabuz, K. Fukatsu, H. Hashimoto, S. Shoji, T. Kurabayashi, K. Minami, and M. Esashi, "Fine frequency tuning in resonant sensors," in *Proceedings IEEE Micro Electro Mechanical Systems An Investigation of Micro Structures, Sensors, Actuators, Machines and Robotic Systems*, pp. 245–250, IEEE, 1994.

[85] W. Zhang and J. E. Y. Lee, "Frequency tuning in a MEMS resonator via an integral crossbar heater," in *Procedia Engineering*, vol. 47, pp. 949–952, jan 2012.

[86] W. Zhang and J. E.-Y. Lee, "Characterization and modeling of electro-thermal frequency tuning in a mechanical resonator with integral crossbar heaters," *Sensors and Actuators A: Physical*, vol. 202, pp. 69–74, nov 2013.

3

CONCEPTUAL SOLUTIONS FOR STIFFNESS ADJUSTMENT IN AFM PROBES

The literature review shows that there are several approaches possible to achieve stiffness adjustment. In this chapter the results and conclusions of the literature review are discussed. The most promising methods which can be applied to an AFM probe are discussed in section 3.1. Three potential concepts are presented in sections 3.1.1 to 3.1.3. The are compared and the final solution is chosen in section 3.2.

3.1. CONCLUSION FROM THE LITERATURE REVIEW

A categorization for stiffness adjustment methods in MEMS was presented in the literature review in section 2.2.2. In this section the most promising categories are selected, based on the obtained results. The selection is made according to three criteria. The first criterion is the change in stiffness Δk and the second is the normalized change in stiffness k_{norm}, which were defined in section 2.2.3. Third is the applicability of a method to a cantilever probe, to ensure compatibility with conventional AFM systems.

In the introduction of the thesis it was stated that at least one order of magnitude in stiffness change is required ($k_{\text{norm}} > 10$). A category qualifies if it already has been proven in literature and will be marked with a check mark (✓) in table 3.1. If it potentially could be applied it will be marked with (~). Categories that do not qualify for a certain criterion will be marked with a cross (×). If the criteria for a certain category are marked with a '✓' or '~', it can potentially be applied for the current application. These categories are indicated with an arrow and are further elaborated in sections 3.1.1 to 3.1.3.

Table 3.1: Comparison of the methods that were presented in the literature review on the applicability for stiffness adjustment of AFM probes. Potentially suitable categories are marked with an arrow.

Physical Principle	**Sub-category**	$\frac{k_{\text{high}}}{k_{\text{low}}}$	Appl. to cantilever	
Electrostatic	Parallel plate	✓	×	
	Varying gap	✓	×	
	Varying electrode shape	~	×	
	Non-interdigitated	~	×	
Mechanical	Change effective length	✓	✓	←
	Engaging mechanical springs	✓	~	←
Second moment of inertia	-	~	✓	←
Stressing effects	Piezoelectrically induced	×	✓	
	Thermally induced	×	×	
	Electrostatically induces	✓	×	
Young's modulus	-	×	✓	

3.1.1. ENGAGING MECHANICAL SPRINGS

Mechanical tuning, by engaging extra mechanical springs was applied by Mueller-Falcke et al. [1, 2], as shown in section 2.3.2.2. The device is capable of switching the stiffness from $0.01\,\mathrm{N\,m^{-1}}$ to $0.1\,\mathrm{N\,m^{-1}}$. So one order of magnitude change is possible. The tuning in this device is not out of plane, but this is achievable.

Concept:
Two pairs of opposing 'rams' clamp the cantilever. These rams can for instance be actuated by thermal expansion or by piezoelectric actuators. These rams add extra mechanical stiffness. This concept does not yet exist in literature.
Advantages:
- Multiple steps of adjusting.
- Large change in stiffness

Disadvantages:
- Difficult to manufacture (ram and cantilever must be very good aligned)
- High clamping force required

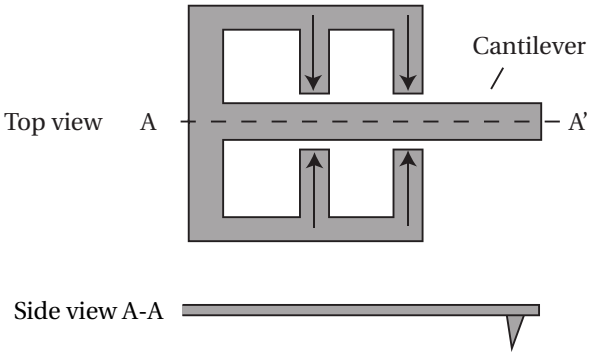

3.1.2. CHANGE EFFECTIVE LENGTH

Change in effective length is a very effective way to achieve a large change in stiffness, as shown in section 2.3.2.1. Out of plane tuning has been proven in literature.

Concept:
Change in effective length by electrostatic clamping. A closely positioned electrode exerts an electrostatic force on the cantilever. The cantilever will pull-in, an insulative layer prevents an electrical connection between the cantilever and electrode.
Advantages:
- Robust
- Large change in stiffness

Disadvantages:
- Only two values of stiffness

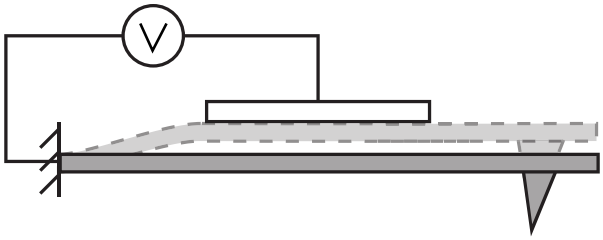

3.1.3. SECOND MOMENT OF INERTIA

Tuning the second moment of inertia was shown in the literature, as discussed in section 2.3.3. A large changes in stiffness and normalized stiffness has not been achieved, but can possibly be implemented in a different configuration.

Concept:
Change in second moment of inertia to change the stiffness. This concept has been proven in literature by Kawai et al. [3]. The second moment of inertia can changed by curing the cantilever along its width. This can be achieved with piezo-electric elements.
Advantages:

- Continuous tuning

Disadvantages:

- High curvature required
- Difficult to manufacture

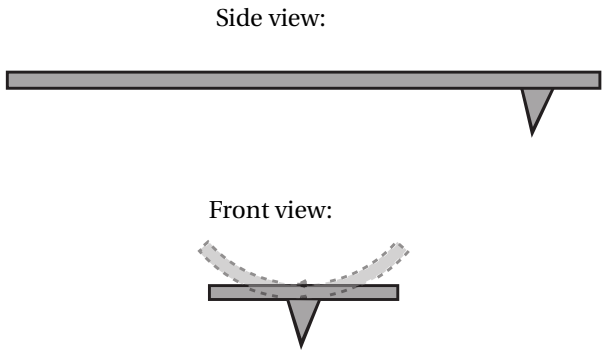

3.2. CONCLUSION

In order to pick the final concept, a comparison is made between the three concepts. This is done for the following three criteria:

- Feasibility: Technological feasibility; a simple design has the advantage over a more complex design
- Tuning Range: The potential tuning range of the device; from untuned to maximally tuned
- Discrete/continuous: Continuous tuning has the preference over discrete switching of stiffness.

Table 3.2: Comparison of the three concepts

Concept	Feasibility	Tuning Range	Discrete/continuous	Total
1	-	+	0	0
2	+	+	-	+
3	-	0	+	0

This analysis shows that concept two, which uses the change in effective length, is the most promising concept. This will be further elaborated over the course of this thesis.

REFERENCES

[1] C. Mueller-Falcke, Y.-A. Song, and S.-G. Kim, "Tunable Stiffness Scanning Microscope Probe," in *SPIE 5604, Optomechatronic Micro/Nano Components, Devices, and Systems* (Y. Katagiri, ed.), vol. 5604, pp. 31–37, oct 2004.

[2] C. Mueller-Falcke, S. D. Gouda, S. S.-G. Kim, and S. S.-G. Kim, "A nanoscanning platform for bio-engineering: an in-plane probe with switchable stiffness.," *Nanotechnology*, vol. 17, pp. S69–S76, feb 2006.

[3] Y. Kawai, T. Ono, E. Meyers, C. Gerber, and M. Esashi, "Piezoelectric Actuator Integrated Cantilever with Tunable Spring Constant For Atom Probe," in *19th IEEE International Conference on Micro Electro Mechanical Systems*, no. January, pp. 778–781, IEEE, 2006.

4

MANUSCRIPT: *In situ* STIFFNESS ADJUSTMENT FOR AFM PROBES UP TO TWO ORDERS OF MAGNITUDE

The concept that was chosen in chapter 3 is further elaborated in this chapter. First, the concept for stiffness tuning is presented, which is followed by characterization of the pull-in behavior with an analytical- and COMSOL model. An experimental setup is presented, which was used to prove the change in stiffness. The cantilever was operated in dynamic mode and the fundamental resonance mode was measured as a function of effective length with a laser Doppler vibrometer. In the results, the outcome of the modeling and experiments are shown. The stiffness was adjusted *in situ* in the range of $0.2\,\mathrm{N\,m^{-1}}$ to $27\,\mathrm{N\,m^{-1}}$, covering two orders of magnitude in a single cantilever. The chapter ends with the discussion and conclusion. This chapter is written in a journal-style format, is submitted to a journal and is under review. Chapters 5 and 6 comprise the supplementary material of the manuscript. The first chapter shows the derivation of the analytical model, which is compared to a stationary COMSOL model and experimental results. This is followed by a time-dependent COMSOL model to study the behavior after pull-in. The second chapter shows details about the experimental setup, shows additional measurement results and a more detailed discussion.

In situ stiffness adjustment for AFM probes up to two orders of magnitude

M L C de Laat[1], H H Pérez Garza[1,2], M K Ghatkesar[1⋆]
[1] Micro and Nano Engineering Group, Faculty of Mechanical, Maritime and Materials (3mE) Engineering, Delft University of Technology, Mekelweg 2, 2628 CD, Delft, The Netherlands
[2] DENSsolutions, Informaticalaan 12, 2628 ZD, Delft, The Netherlands
⋆ E-mail: m.k.ghatkesar@tudelft.nl

Abstract
The choice on which type of cantilever to use for Atomic Force Microscopy (AFM) depends on the type of the experiment being done. Typically, the cantilever has to be exchanged when a different stiffness is required and the entire alignment has to be repeated. In the present work, a method to adjust the stiffness of an AFM cantilever *in situ* is developed. The adjustment is achieved by changing the effective length of the cantilever by electrostatic pull-in. By applying a voltage between the cantilever and an electrode (with an insulating layer at the point of contact), the cantilever snaps to the electrode, reducing the cantilever's effective length. An analytical model was developed to find the pull-in voltage of the system. Subsequently, a time-dependent COMSOL model was developed to study the behavior after pull-in. The working principle of this concept is demonstrated with a proof-of-concept experiment. The electrode was positioned close to a commercially available cantilever by using a robotic nanomanipulator. To confirm the change in stiffness, the fundamental resonance frequency of the cantilever was measured for varying electrode positions. The results match with the theoretical expectations. The stiffness was adjusted *in situ* in the range of 0.2 N/m to 27 N/m, covering two orders of magnitude using one single cantilever. This proof-of-concept is the first step towards a micro fabricated prototype, that integrates the electrode positioning system and cantilever that can be used for actual AFM experiments.

4.1. INTRODUCTION

The Atomic Force Microscope (AFM) was invented by Binnig and Quate in 1986 [1]. AFM is a technology that can image samples with extreme high resolution. In good conditions sub-nanometer resolution can be achieved and it is possible to visualize individual atoms [2]. An AFM uses a silicon based chip with a cantilever beam and a very sharp tip to probe a surface. The forces that act on the tip cause the cantilever beam to deflect, which is measured with a sensor. With this information, the topography of the surface can be reconstructed. It is also possible to calculate the force between tip and sample by using the (known) stiffness of the cantilever by using Hooke's law. This information can for instance be used to measure material properties like Young's modulus [3] and molecular interaction force [4, 5].

The stiffness of the cantilever is very important to the type of measurement that needs to be performed; for a different type of measurement a different stiffness is needed [6]. The range of cantilever stiffness for different type of measurements is shown figure 4.1. In practice, users have to exchange the cantilever if they want to switch to a different stiffness; this consumes a lot of time, the alignment of the sensor has to be repeated and

the sample needs to be relocated. It would provide a great advantage if the stiffness of an AFM probe could be changed *in situ*. The change in stiffness should at least be one order of magnitude to be of any significance. An example of a potential application is Peak Force tapping mode, which is used for simultaneous imaging and Young's modulus mapping [7]. The stiffness of the cantilever should match the Young's modulus for high accuracy measurements. Samples with high Young's modulus variability cannot be accurately measured with a single cantilever. A tunable stiffness probe would provide the solution to successfully measure these samples.

Earlier attempts to design an *in situ* tunable stiffness probe were done. Mueller-Falcke *et al.* designed a switchable stiffness probe [8, 9]. This probe can switch between $0.01\,\mathrm{N\,m^{-1}}$ and $0.1\,\mathrm{N\,m^{-1}}$. This change in stiffness is sufficiently large to switch to a different AFM mode, but the probe is not compatible with conventional AFM systems. This probe does not use a cantilever beam, but an in-plane moving shuttle. So in order to do AFM measurements with this probe, the system must be adapted to this type of probe. Kawai *et al.* presented an AFM probe of which the stiffness can be tuned by changing the second moment of inertia [10]. A piezoelectric actuator can change the curvature of this cantilever. It is compatible with conventional AFM systems. But the proven change in stiffness is only 14%, which is too small to switch to another mode. An AFM probe with *in situ* adjustable stiffness, which is both compatible with conventional AFM systems and that has a large tuning range will be presented in this paper. A conceptual design will be proposed and the working principle will be demonstrated. The change in stiffness is achieved by reducing the effective

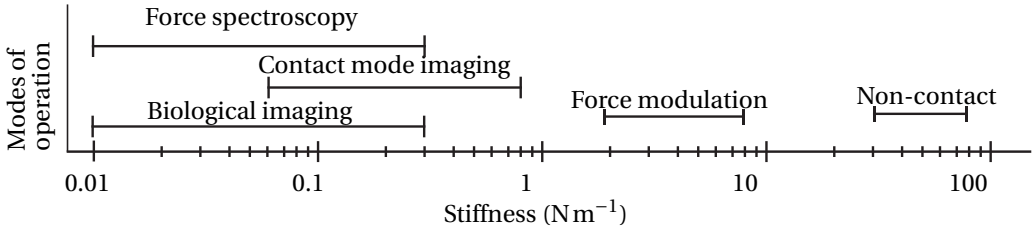

Figure 4.1: The range of stiffness for the AFM cantilever for different imaging modes.

length of the cantilever. This is done by placing a parallel electrode close to the cantilever and applying a bias voltage V_{DC} between the cantilever and this electrode as shown in figure 4.2. The cantilever pulls-in to the electrode (dashed line). The insulator makes sure that there is no electrical contact between the cantilever and electrode. When the voltage is further increased, the cantilever will end up in the final state (solid line). The cantilever is clamped to the electrode due to the electrostatic force. The change in effective length of the cantilever results in a change in stiffness. The stiffness of a cantilever beam is governed by the following equation:

$$K_{\mathrm{eff}} = \frac{3EI}{{L_{\mathrm{eff}}}^3} \tag{4.1}$$

Where E is the Young's modulus, I the second moment of inertia and L_{eff} the effective length. So if the effective length is reduced, the stiffness will increase. For example; in order to increase the stiffness one order of magnitude, the effective length should decrease $\sqrt[3]{10} = 2.15$ times.

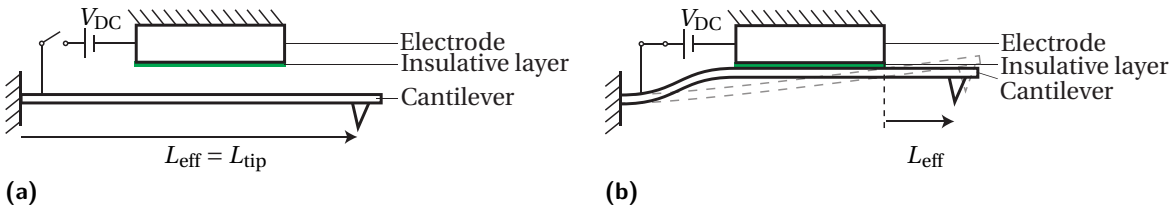

Figure 4.2: In (a) the cantilever is in unadjusted state. When the bias voltage V_{DC} is applied, the cantilever will start bending towards the electrode. When the bias voltage is bigger than the pull-in voltage, the cantilever will pull-in towards the electrode (b). The cantilever will hit the electrode (dashed line) and will be in a stable state. When the voltage is further increased, the cantilever will finally be in the tuned state. The effective length L_{eff} of the cantilever has decreased, and the stiffness is increased.

4.2. EXPERIMENTAL SECTION

4.2.1. MODELING

When a voltage is applied, the cantilever will start bending towards the electrode. The mechanical restoring forces will increase linearly with displacement, while the electrostatic force increases inversely quadratic with displacement. When the electrostatic force is larger than the mechanical restoring force, pull-in will occur. This corresponds with the state which is indicated with the dashed line in figure 4.2. A model is developed to determine the required voltage to achieve electrostatic pull-in. The model is based on Do *et al.* [11] and is modified such that it can be used for this particular system. The derivation of this model and experimental verification are found in the supplementary materials. The required bias voltage V_{DC} for equilibrium is expressed as:

$$V_{\mathrm{DC}} = \sqrt{\frac{12\hat{E}I\,y(L_{\text{c-el}})}{\epsilon_{\mathrm{air}}\epsilon_{\mathrm{ins}}{}^2\, w_{\mathrm{eff}} \int_{L_{\text{c-el}}-\alpha L_{\text{c-el}}}^{L_{\text{c-el}}} \frac{x^2(3L_{\text{c-el}}-x)}{(\epsilon_{\mathrm{air}} d_{\mathrm{ins}}+\epsilon_{\mathrm{ins}}(g_0-y(x)))^2}\,\mathrm{d}x}} \tag{4.2}$$

The pull-in voltage (V_{PI}) is found when V_{DC} is at its maximum. For voltages higher than V_{PI}, the system is unstable. The geometric parameters are shown in figure 4.3a. $\hat{E}$ is the effective Young's modulus ($\hat{E} = E/(1-\nu^2)$ with $E$and ν the Young's modulus and Poisson's ratio respectively), I the second moment of inertia, ϵ_{air} and ϵ_{ins} are the dielectric permittivity in air and insulator respectively. The effective width of the cantilever w_{eff} compensates for fringe field effects [12]:

$$w_{\mathrm{eff}} = w\Big(1+0.65\frac{(1-y(L_{\mathrm{tip}})/g_0)g_0}{w}\Big) \tag{4.3}$$

In order to be able to calculate the electrostatic force, an assumption is made on the shape of the cantilever $y(x)$, which is fitted to FEM results and is found to be:

$$y(x) = \Big(2.56 - \frac{16.127}{4(x/L_{\mathrm{tip}}+0.00185)^2+6.2786}\Big)y(L_{\mathrm{tip}}) \tag{4.4}$$

The deflection at the tip $y(L_{\mathrm{tip}})$ is found by linearly extrapolating the deflection at $y(L_{\text{c-el}})$:

$$y(L_{\mathrm{tip}}) = y(L_{\text{c-el}}) + \frac{\mathrm{d}y(x)}{\mathrm{d}x}\Big|_{L_{\text{c-el}}}(L_{\mathrm{tip}} - L_{\text{c-el}}) \tag{4.5}$$

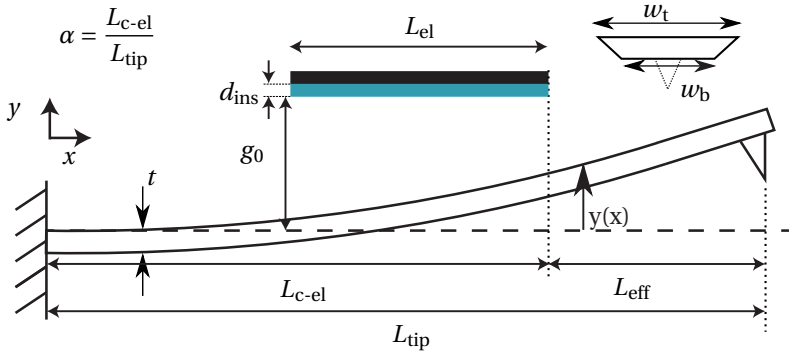

(a) Geometry of the COMSOL model for time dependent simulation

Parameter	Value (μm)
L_{tip}	455.7
L_{el}	229.4
L_{eff}	52
d_{ins}	1.6
g_0	6
t	2
w_{t}	57.8
w_{b}	46.7

(b) Summary of parameters used for the simulation.

Figure 4.3: Schematic of the system. The parameters which are used for the modeling are shown in the table.

A COMSOL model was developed for comparison with the analytical model and to study post-pull-in behavior. First, a stationary study is performed, up to the pull-in voltage. Beyond the pull-in voltage, a time dependent study is performed. This model is based on the 'Pull-in of an RF MEMS Switch' of the COMSOL library. The configuration of the model and the corresponding parameters are shown in figure 4.3.

4.2.2. EXPERIMENTAL SETUP

An experimental setup was developed to prove the change in stiffness of the cantilever. The setup is shown in figure 4.4. A commercially available silicon probe was used for this experiment (BudgetSensors ContAl 0.2 N m^{-1}, E = 169 GPa, ν = 0.28). It was mounted on top of a stack of a prototyping PCB, a piezo actuator, an insulative 125 µm thick sheet of polydimethylsiloxane (PDMS) from Shielding Solutions. A small spring was used to apply a clamping force on this stack. A remotely controlled robotic nanomanipulator (miBot) from Imina Technologies was used to position the electrode relative to the cantilever. This manipulator can move in-plane and has an arm that determines the height of the electrode. The electrode is made by laser cutting of a 150 µm thick sheet of spring steel. It is covered by a 1.6 µm layer of photo resist (AZ9260), with a dielectric constant of 4.03. It is important that this layer has a high dielectric strength, such that the insulative properties remain intact when the cantilever is pulled-in. According to specifications the dielectric strength is 694 V µm^{-1}, which is sufficient. The electrode and cantilever should be perfectly parallel. This is controlled by placing the stack with the cantilever on a compliant hinge. In order to apply the bias voltage between the cantilever and electrode there are electrical connections that connect the system to a voltage source of maximum 60 V. In order to protect the system in case of a short circuit, a current limiting resistor of 68 kΩ is added to the circuit. The setup is placed in a Polytec MSA-400 lased doppler vibrometer. This system is used to measure the resonance frequency and modes of the cantilever. The piezo actuator under the cantilever is used to actuate the system, using a frequency sweep. The vibrometer measures the response of the cantilever. The response of the cantilever is measured for a varying electrode position. The fundamental resonance frequency is compared to the theoretical value. More details of this experimental setup are shown in the supplementary materials.

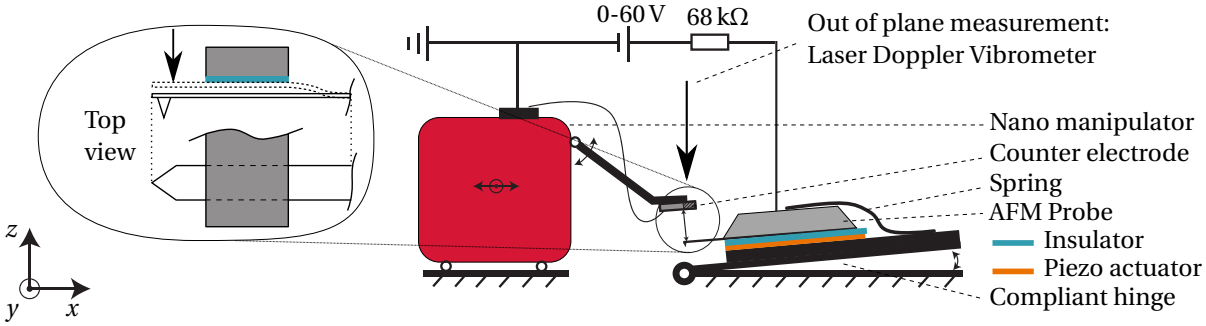

Figure 4.4: Experimental setup. A robotic nano-manipulator is used to position the electrode relative to a a commercially available cantilever. The AFM probe is actuated with a piezoelectric actuator and the frequency response is measured with a laser doppler vibrometer for a varying electrode position along the length of the cantilever.

4.3. RESULTS

4.3.1. MODELING RESULTS

The shape of the cantilever for a varying voltage is shown in figure 4.5. In figure 4.6 the deflection at the tip in steady state is shown as a function of the bias voltage. The COMSOL results are compared with the analytical model. The pull-in voltage of this system is found to be 21 V. When the voltage is further increased to 65 V, the system is in the stiffness adjusted state. More details of the model are found in the supplementary materials.

4.3.2. EXPERIMENTAL RESULTS

The position of the electrode relative to the cantilever ($L_{\text{c-el}}$) is varied by using the nano-manipulator. For each position the cantilever is pulled-in as shown in figure 4.7. The frequency response is measured for each of these positions, which is shown in figure 4.8. This plot shows that the resonance frequency increases, for a

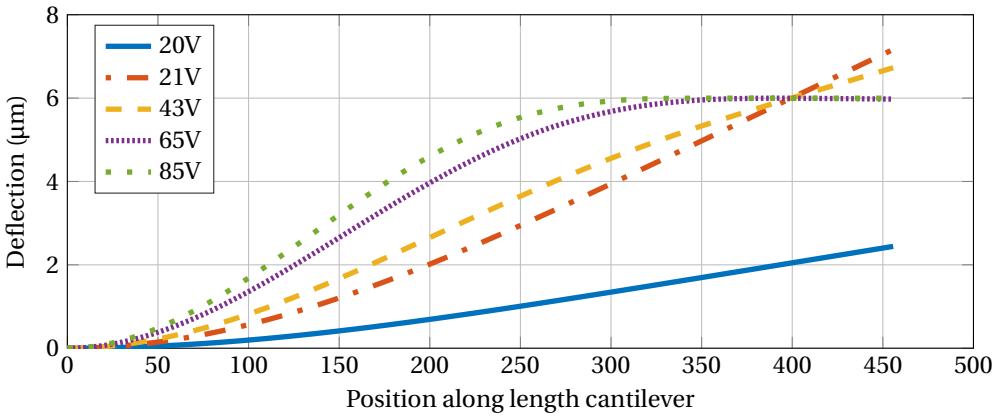

Figure 4.5: The shape of the cantilever is shown as a function of the position along the length of the cantilever. This is shown for a varying voltage.

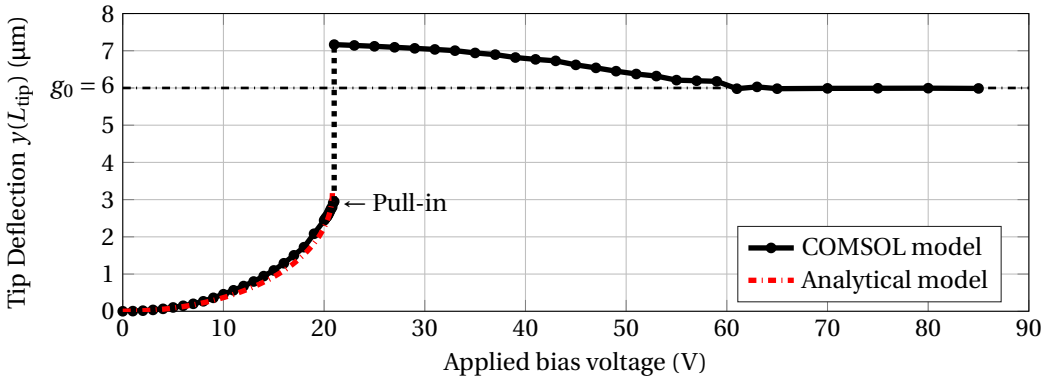

Figure 4.6: COMSOL modeling results. Tip deflection as a function of applied voltage. Up to pull-in the system is simulated as a stationary system, while after pull-in it is simulated with a time-depended study. For this part, the deflection at steady state is shown.

decreasing effective length, as was expected. The measured resonance frequency that is shown in figure 4.8 is compared with the theoretical resonance frequency in figure 4.9. The corresponding theoretical stiffness is indicated as well, to show which value of stiffness corresponds to a certain value of resonance frequency. The effective length is measured with an optically calibrated microscope. The error bars indicate the uncertainty on the measurement of the effective length. More details and results are shown in the supplementary materials.

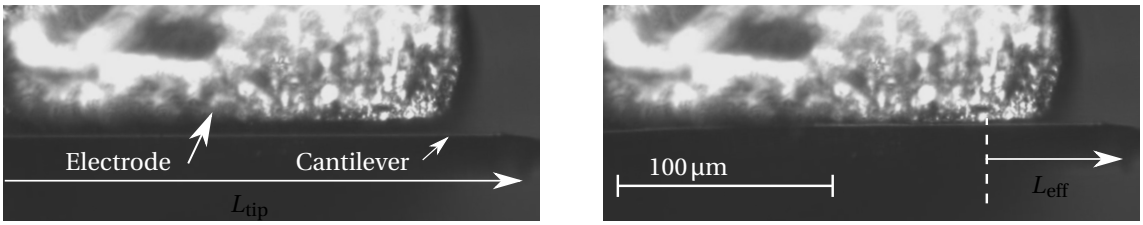

(a) **(b)**

Figure 4.7: Micrograph of the cantilever and electrode in unadjusted (a) and adjusted state (b) in side view. These states correspond to the ones shown in figure 4.2.

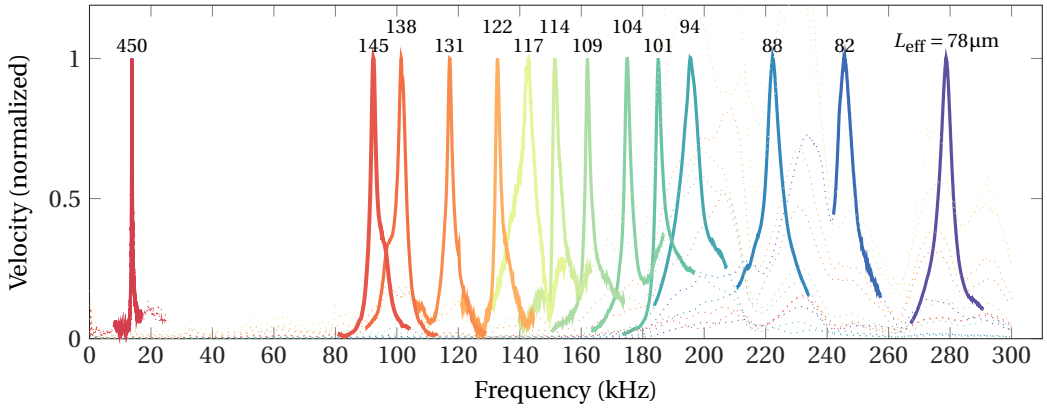

Figure 4.8: The electrode position is varied and the cantilever is pulled-in for these positions, reducing its effective length. The cantilever is actuated with a frequency sweep and the response is shown in this figure. The numbers above the peaks indicate the effective length of the cantilever (in µm). Only the peaks are shown in a solid line, while the rest of the bandwidth is plotted as a dotted line for clarity. More data and a detailed discussion is found in the supplementary material

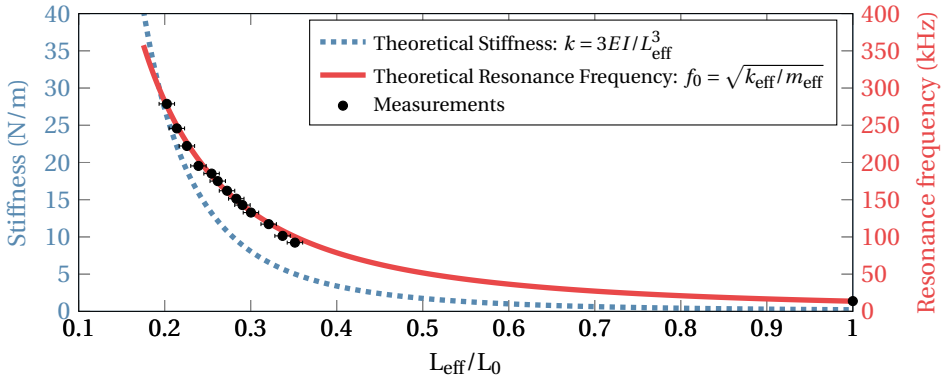

Figure 4.9: Theoretical stiffness and resonance frequency compared with the measurements as a function of the normalized effective length. The measurement points correspond with the peaks found in figure 4.8

4.4. DISCUSSION

The goal of the experiment was to show that the stiffness of the cantilever can be changed by reducing the effective length due to electrostatic pull-in. In figure 4.7 it is shown that the cantilever pulls in as expected. In figure 4.8 the frequency response of the cantilever is shown for a varying effective length. It is shown that the resonance frequency of the cantilever shifts to higher values, when the effective length of the cantilever is reduced. The measurement point that are shown in this figure are used in figure 4.9 to show the change in resonance as a function of the change in effective length. This is compared with the theoretical resonance frequency. The measurements do match the theory very good. The error bars on the measurements indicate the uncertainty on the optical measurement on the effective length. The resolution is limited, and the exact point of clamping is not exactly known, due to the curved shape of the electrode near the edge. It is assumed that this point is known within ±10 pixels, which is a conservative estimate. The uncertainty on the resonance frequency of the measurement is determined by the resolution of the Laser Doppler Vibrometer, which is 78.125 Hz for the bandwidth that was used for the measurements. This is negligible compared to the measured frequencies. During the measurements it was observed that when the electrode was in close proximity ($\sim 5-10$µm), but the cantilever was not pulled-in, most of the first resonance mode was damped,. Squeeze-film damping could be the phenomenon causing this behavior. The air is trapped between the cantilever and electrode due to the small gap and viscous forces on the cantilever are increased. The squeeze-film damping effect is further elaborated in the supplementary materials. In some cases the cantilever was not restored to its unadjusted state after the voltage was released. This is caused by stiction. In order to prevent this, precautions should be taken in following experiments. This can for instance be done by decreasing contact area

by surface roughening or applying dimples, or chemically modifying the surface with an anti-stiction coating [13].

4.5. CONCLUSIONS

The concept of a tunable stiffness AFM probe was presented. The change in stiffness was achieved by a change in effective length by means of electrostatic pull-in. The experiments show that the concept works and that it matches with the theory well. By reducing the unadjusted length of 450 µm to 162 µm the stiffness was changed from 0.2 $\mathrm{N\,m^{-1}}$ to 27 $\mathrm{N\,m^{-1}}$. The experimental setup is used as a proof of concept, and is not capable of performing actual AFM measurements. Further research should focus on the manufacturing of a micro fabricated prototype that integrates the cantilever and electrode in a single device. This can be used in any commercially available AFM setup to perform actual AFM measurements. In order to facilitate the tuning voltage, electrical connections and peripheral electronics are required. As a next step attempts should be made to integrate an electrode which is movable along the length of the cantilever, such that effective length and adjusted stiffness can be continuously tuned *in situ*. Such a device can greatly improve the ease of use of AFM systems and open the door to even more versatile measurements.

REFERENCES

[1] G. Binnig, C. F. Quate, and C. Gerber, "Atomic Force Microscope," *Physical Review Letters*, vol. 56, pp. 930–933, mar 1986.

[2] T. R. Albrecht and C. F. Quate, "Atomic resolution imaging of a nonconductor by atomic force microscopy," *Journal of Applied Physics*, vol. 62, p. 2599, oct 1987.

[3] N. A. Burnham, "Measuring the nanomechanical properties and surface forces of materials using an atomic force microscope," *Journal of Vacuum Science & Technology A: Vacuum, Surfaces, and Films*, vol. 7, p. 2906, jul 1989.

[4] O. H. Willemsen, M. M. Snel, A. Cambi, J. Greve, B. G. De Grooth, and C. G. Figdor, "Biomolecular interactions measured by atomic force microscopy.," *Biophysical journal*, vol. 79, pp. 3267–81, dec 2000.

[5] T. Hugel and M. Seitz, "The Study of Molecular Interactions by AFM Force Spectroscopy," *Macromolecular Rapid Communications*, vol. 22, pp. 989–1016, sep 2001.

[6] Y. F. Dufrêne, D. Martínez-Martín, I. Medalsy, D. Alsteens, and D. J. Müller, "Multiparametric imaging of biological systems by force-distance curve–based AFM," *Nature Methods*, vol. 10, pp. 847–854, aug 2013.

[7] Bruker, "Peak Force Tapping Mode."

[8] C. Mueller-Falcke, Y.-A. Song, and S.-G. Kim, "Tunable Stiffness Scanning Microscope Probe," in *SPIE 5604, Optomechatronic Micro/Nano Components, Devices, and Systems* (Y. Katagiri, ed.), vol. 5604, pp. 31–37, oct 2004.

[9] C. Mueller-Falcke, S. D. Gouda, S. S.-G. Kim, and S. S.-G. Kim, "A nanoscanning platform for bioengineering: an in-plane probe with switchable stiffness.," *Nanotechnology*, vol. 17, pp. S69–S76, feb 2006.

[10] Y. Kawai, T. Ono, E. Meyers, C. Gerber, and M. Esashi, "Piezoelectric Actuator Integrated Cantilever with Tunable Spring Constant For Atom Probe," in *19th IEEE International Conference on Micro Electro Mechanical Systems*, no. January, pp. 778–781, IEEE, 2006.

[11] C. Do, M. Lishchynska, K. Delaney, and M. Hill, "Generalized closed-form models for pull-in analysis of micro cantilever beams subjected to partial electrostatic load," *Sensors and Actuators, A: Physical*, vol. 185, pp. 109–116, 2012.

[12] S. Pamidighantam, R. Puers, K. Baert, and H. A. C. Tilmans, "Pull-in voltage analysis of electrostatically actuated beam structures with fixed-fixed and fixed-free end conditions," *Journal of Micromechanics and Microengineering*, vol. 12, pp. 458–464, jul 2002.

[13] Z. Yapu, "Stiction and anti-stiction in MEMS and NEMS," *Acta Mechanica Sinica*, vol. 19, pp. 1–10, feb 2003.

5

SUPPLEMENTARY MATERIAL: CHARACTERIZATION OF ELECTROSTATIC PULL-IN BEHAVIOR OF AFM PROBES

In order to get a good understanding of the system a study has been performed on the voltage-deflection behavior of a cantilever under an electrostatic load. Experiments were performed on a commercially available cantilever. These measurements were compared with models. In section 5.1 the used probes are characterized.

Two models were developed to study the system. The first model is an analytical model, that is based on previous work in literature [1], which is described in section 5.2. The second model is a COMSOL model which is shown in section 5.3. These models are compared with measurements that were performed on a commercially available AFM cantilever, which is elaborated in section 5.5.

In order to facilitate the modeling, the shape of the cantilever is simplified according to figure 5.1. The shape of the cantilever near the tip is triangularly shaped from top view. This triangle starts at L_{side} and ends at L_{tot}. The tip is located at L_{tip}, which is approximately at the center of this triangle. For the models it is assumed that the cantilever has a constant cross section and has length L_{tip}.

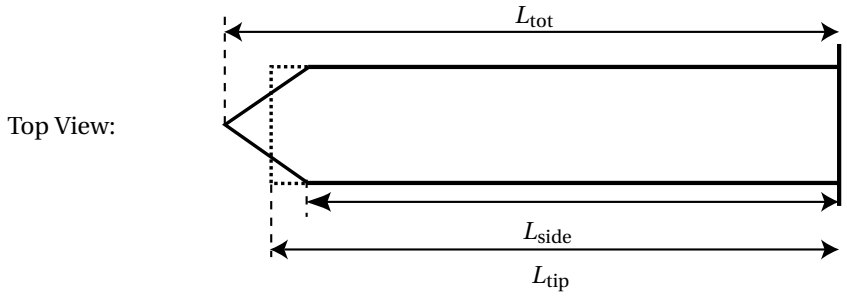

Figure 5.1: Approximation of cantilever geometry for modeling. The solid line is the actual geometry near the tip, while the dashed line shows the approximation used for modeling.

5.1. CANTILEVER CHARACTERIZATION

In order to make a fair comparison between models and measurement, it is important to know the dimensions and properties of the cantilever as accurate as possible. These properties can then be used as input for the model. The dimensions which are in the specifications of the product have a large tolerance as shown in table 5.1. The aluminum reflex coating is neglected. The most important parameters are the geometry of the cantilever (length and thickness) and material properties, because these determine the stiffness of the cantilever. In section 5.1.1 the material properties of the cantilever are presented. In section 5.1.2 the method for measuring the length and with of the cantilever is shown. The measurement of the thickness is explained in section 5.1.3.

Table 5.1: Specifications of the cantilever from the supplier

Property	**Value**	**Range**
Resonance frequency	13 kHz	±4 kHz
Force constant	0.2 N m^{-1}	0.07 to 0.4 N m^{-1}
Length	450 µm	±10 µm
Mean Width	50 µm	±50 µm
Thickness	2 µm	±1 µm
Tip Height	17 µm	±2 µm
Tip Set Back	15 µm	±5 µm
Tip Radius	<10 nm	
Reflex coating	Aluminium relfex coating 30 nm thick	
Half Cone Angle	20° – 25° along cantilever axis	
	25° – 30° from side	
	10° at the apex	

5.1.1. MATERIAL PROPERTIES

The Young's modulus in silicon is anisotropic, in each crystallographic direction the value is different [2]. After inquiry at the manufacturer of the used probes, the cantilevers point in the ⟨110⟩ direction. This corresponds to a Young's modulus of 169 GPa. For wide, thin beams ($w \geq 5t$) an effective Young's modulus $\hat{E}$ is used. This is defined as $\hat{E} = E \setminus (1-\nu^2)$, with ν the Poisson's ratio. Also the Poisson's ratio is not constant in all directions. For the out of plane bending of the cantilever: $\nu = 0.28$. The density of silicon is 2320 kg m^{-3}.

5.1.2. LENGTH AND WIDTH

The length and width of the cantilevers are measured with the Scanning Electron Microscrope (SEM). Since the cantilever has a trapezoidal cross section, this measurement is done both on the top- and bottom side. The definition of these dimensions are shown in figure 5.2. The results are summarized in table 5.2. A typical set of images, used to determine the dimensions are shown in appendix B. These dimensions are assumed to be measured with ±0.5µm accuracy.

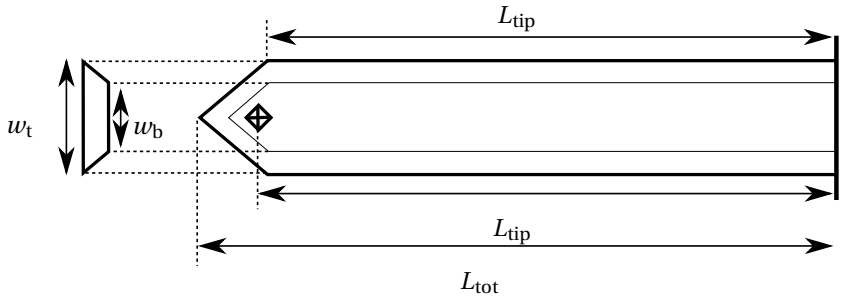

Figure 5.2: The definition of the dimensions that were measured with the SEM.

5.1.3. THICKNESS

In contrast to the length and the width, the thickness is not measurable with the SEM. Because of the trapezoid shape of the cross section of the cantilever, it is not possible to have the entire thickness in focus due to the limited depth of focus. The thickness can be calculated by measuring the resonance frequency, and solving the following equation for the thickness which is the only unknown parameter:

$$f_0 = \frac{1}{2\pi}\sqrt{\frac{k}{m_{\text{eff}}}} \tag{5.1}$$

$$= \frac{1}{2\pi}\sqrt{\frac{3EI(t)}{m_{\text{eff}}(t)}} \tag{5.2}$$

with:

$$I = \frac{{t_c}^3}{36}\frac{{w_t}^2 + 4w_t w_b + {w_b}^2}{w_t + w_b} \tag{5.3}$$

$$m_{\text{eff}} = m_{\text{tip}} + \frac{33}{140}m_{\text{cant}} \tag{5.4}$$

$$= m_{\text{tip}} + \frac{33}{140}(\rho_s L_{\text{tip}} t_c \frac{w_t + w_b}{2}) \tag{5.5}$$

The resonance frequency can be determined very accurate with a laser Doppler vibrometer. The probe is placed on a piezoelectric actuator. A frequency sweep is applied to the actuator and the response of the cantilever is measured. The resolution of the vibrometer is 3.12 Hz.

The exact shape of the cantilever needs to be approximated, because the complex geometry near the end of the cantilever cannot be taken into account by this model. The simplified model is shown in figure 5.3. The volume which is indicated in gray is assumed to be a concentrated mass at L_{tip}. This consists of the tip itself and the triangular end facet of the cantilever. This part is approximated by a triangle with a base width of $\frac{w_t+w_b}{2}$. The volume of the tip is hard to estimate, because the shape is complex. It is approximated by a pyramid shape, with a base of 6 µm and a height of 15 µm, which is estimated with the SEM. The volume of a pyramid is: $V = \frac{l \times w \times h}{3}$. It is assumed that this volume is determined within ±20 % accuracy.

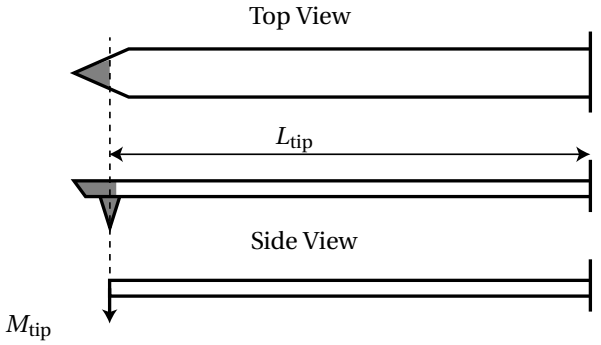

Figure 5.3: The model of the cantilever to calculate the thickness as a function of its resonance frequency. The gray parts are considered to be a concentrated mass at the end of the cantilever. The length is assumed to be equal to the length upto the tip.

5.1.4. CONCLUSIONS

The length and with of the cantilever were measured by using a SEM. The thickness of the cantilever is determined by measuring the resonance frequency with a laser Doppler vibrometer, and solving equation (5.2) for

the thickness. The measurements with the SEM are assumed to be accurate within ±0.5µm. The measurement of the resonance frequency is assumed to be accurate within ±3Hz. The volume, which is assumed to be a concentrated mass at L_{tip} is assumed to be accurate within ±20%. The measured dimensions, resonance frequencies and resulting thickness and confidence interval are shown in table 5.2.

Table 5.2: Dimensions and resonance frequency of the used cantilevers. This data is acquired by measurement with a Scanning electron microscope and laser doppler vibrometer. The accuracy of the dimensions is assumed to be ±0.5µm, for the resonance frequency ±3.12Hz

Cantilever	L_{side}(µm)	L_{tip}(µm)	L_{tot}(µm)	w_{t}(µm)	w_{b}(µm)	f_0(Hz)	t_{c}(µm)
C1	438.8	453.0	471.0	57.8	46.6	13793.75	2.045 ±0.029
C3	436.0	446.0	476.5	57.7	46.2	13409.38	1.981 ±0.037
C5	437.0	450.6	473.4	57.7	46.8	13481.25	1.999 ±0.032
C7	443.4	455.7	476.9	57.8	46.7	13265.63	2.004 ±0.030

5.2. ANALYTICAL MODEL

Pull-in behavior of micro cantilevers is a well researched topic. Several approaches were presented like simplified closed-form analytical models [3–6], numerical method of solving differential equations [7] and a semi-analytical approach [1]. These (semi-) analytical models provide an advantage over finite element models and numerical methods in terms of speed of calculation, but require more simplifications that might yield less accurate results. The model developed by Do et al. [1] is chosen for the modeling of the system; it includes the possibility to include a partially covering electrode, incorporates fringe fields and a non-uniform electrostatic load. First, the original model will be presented in section 5.2.1. In section 5.2.2 a modification of the model is presented to adapt it to the configuration of the experiments.

5.2.1. THE ORIGINAL MODEL

The schematic view of the model is shown in figure 5.4a, and the cross section of the cantilever in figure 5.4b. It is assumed that the cantilever has a constant cross section. The cantilever of length L_{tip} is fixed on the left side. An electrode of length L_{el} is covering a part of the cantilever. The deflection at each point along the cantilever is described by $y(x)$, and the deflection at the tip as $y(L_{\text{tip}})$. The gap g_0 is defined as the distance between electrode and cantilever in undeflected state. The parameter α is the ratio between the length of the electrode and the length of the cantilever.

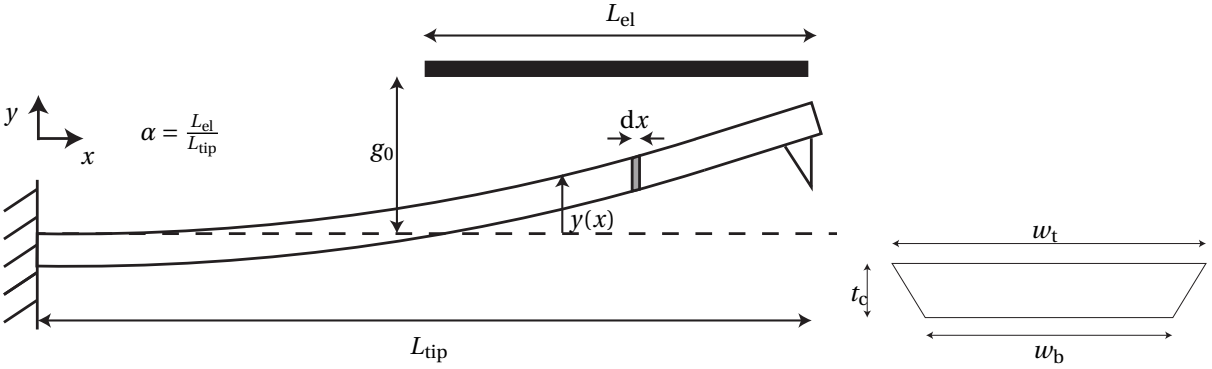

(a) Schematic side view with electrode covering a part of the cantilever. The analytical model is based on this schematic. **(b)** Cross section of the cantilever.

Figure 5.4: Schematic drawing of the model, inspired by [1].

The electrostatic force on a small element of the cantilever of length dx is defined as:

$$q_{\text{elec}}(x) = \frac{\epsilon_{\text{air}} w_{\text{eff}} {V_{\text{DC}}}^2}{2(g_0 - y(x))^2} \mathrm{d}x \tag{5.6}$$

Where V_{DC} is the applied potential between electrode and cantilever and w_{eff} is the effective width of the cantilever, compensated for fringe field effects [8]:

$$w_{\text{eff}} = w_{\text{t}}\big(1 + 0.65\frac{(1 - y(L_{\text{tip}})/g_0)g_0}{w_{\text{t}}}\big) \tag{5.7}$$

The deflection at the tip of a cantilever due to a distributed force is given by [9]:

$$\mathrm{d}y(L_{\text{tip}}) = \frac{q_{\text{elec}}(x)x^2(3L - x)}{6\hat{E}I} \tag{5.8}$$

Where $\hat{E}$ is the effective Young's modulus ($\hat{E} = E \setminus (1 - \nu^2)$ with ν Poisson's ratio, for wide beams ($w_{\text{c}} \geq 5t_{\text{c}}$)) and I the second moment of area. The paper assumes a rectangular shaped cantilever, while in the present work a trapezoidal cantilever is used. To incorporate this, the following expression will be used [7]:

$$I = \frac{{t_{\text{c}}}^3}{36} \frac{{w_{\text{t}}}^2 + 4w_{\text{t}}w_{\text{b}} + {w_{\text{b}}}^2}{w_{\text{t}} + w_{\text{b}}} \tag{5.9}$$

Where t_{c} is the thickness, w_{t} and w_{b} the width at the top and bottom respectively.

The deflection at the end of the cantilever is found by substituting equation (5.6) in equation (5.8) and integrating over the region where the electrode and cantilever overlap:

$$y(L_{\text{tip}}) = \frac{\epsilon_{\text{air}} w_{\text{eff}} {V_{\text{DC}}}^2}{12\hat{E}I} \int_{L_{\text{tip}} - \alpha L_{\text{tip}}}^{L_{\text{tip}}} \frac{x^2(3L_{\text{tip}} - x)}{(g_0 - y(x))^2} \mathrm{d}x \tag{5.10}$$

The total force is found in a similar way, by integrating the distributed load equation (5.6) over the overlapping section:

$$\vec{F}_{\text{e}} = \int_{L_{\text{el}}} q_{\text{elec}}(x) = \frac{\epsilon_{\text{air}} w_{\text{eff}} {V_{\text{DC}}}^2}{2} \int_{L_{\text{tip}} - \alpha L_{\text{tip}}}^{L_{\text{tip}}} \frac{1}{(g_0 - y(x))^2} \mathrm{d}x \tag{5.11}$$

So the effective non-linear stiffness of the entire system can be expressed as:

$$K_{\text{eff}}(y(L_{\text{tip}})) = \frac{\vec{F}_{\text{e}}}{y(L_{\text{tip}})} \tag{5.12}$$

$$= 6\hat{E}I \frac{\int_{L_{\text{tip}} - \alpha L_{\text{tip}}}^{L_{\text{tip}}} 1/(g_0 - y(x))^2 \mathrm{d}x}{\int_{L_{\text{tip}} - \alpha L_{\text{tip}}}^{L_{\text{tip}}} x^2(3L_{\text{tip}} - x)/(g_0 - y(x))^2 \mathrm{d}x} \tag{5.13}$$

Pull-in will occur when the electrostatic force exceeds the mechanical restoring force of the cantilever. This point of instability can be found at:

$$\vec{F}_{\text{e}} = K_{\text{eff}} y(L_{\text{tip}}) \tag{5.14}$$

Solving this equation for the applied voltage yields:

$$V_{\mathrm{DC}} = \sqrt{\frac{12\hat{E}I\,y(L_{\mathrm{tip}})}{\epsilon_{\mathrm{air}}\,w_{\mathrm{eff}}\int_{L_{\mathrm{tip}}-\alpha L_{\mathrm{tip}}}^{L_{\mathrm{tip}}}\frac{x^2(3L-x)}{(g_0-y(x))^2}\,\mathrm{d}x}} \tag{5.15}$$

In order to solve this equation, the shape of the cantilever should be known. This is approximated using a FEM extracted shape function:

$$y(x) = \left(2.56 - \frac{16.127}{4(x/L_{\mathrm{tip}} + 0.00185)^2 + 6.2786}\right) y(L_{\mathrm{tip}}) \tag{5.16}$$

This shape is validated with COMSOl results in section 5.4. A numerical method was presented to find the closed form of the integral. For this thesis the closed-form is not used; Matlab® is used to compute the complicated integral for the FEM extracted shape function.

5.2.2. EXTENDING THE MODEL FOR THE CURRENT SYSTEM

The model as presented in the previous section should be extended such that it can handle a partially covering electrode and an insulative layer, as shown in figure 5.5a. The original model assumes that the end of the electrode and cantilever are aligned. But in the experimental setup this is not the case. In the new model it is assumed that the last part of the cantilever is protruding. The part of the cantilever up to the edge of the electrode is defined as $L_{\text{c-el}}$. Fringe field effects at this edge are neglected. The equation for the distributed electrostatic load (equation (5.6)) should include the influence of the insulating layer. The distributed electrostatic force $q_{\mathrm{elec}}(x)$ is depending on the permittivity of the insulator ϵ_{ins} and layer thickness d_{ins}. (Note that the permittivity in a certain medium is defined as the product of the absolute and relative permittivity. For air the relative permittivity is equal to one, so $\epsilon_{\mathrm{air}} = \epsilon_0$. The permittivity in the insulator is: $\epsilon_{\mathrm{ins}} = \epsilon_{\mathrm{r}}\epsilon_0$.) If we consider the situation of figure 5.5a, a small section of length dx can be shown as figure 5.5b. The displacement vector $\vec{D}$ is equal in both the insulator and the air gap, and the total voltage V_{DC} is the sum of the voltage drop over the insulator and air gap ($g = g_0 - y(x)$):

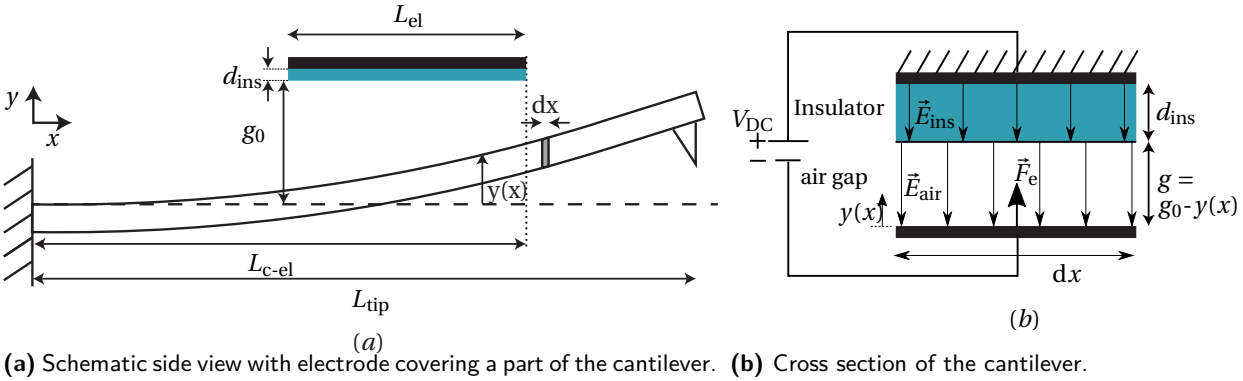

(a) Schematic side view with electrode covering a part of the cantilever. **(b)** Cross section of the cantilever. The electrode is covered with an insulative layer.

Figure 5.5: Modified schematic of the model such that it includes a dielectric layer and a protruding part of the cantilever.

$$V_{\mathrm{DC}} = V_{\mathrm{ins}} + V_{\mathrm{air}} \tag{5.17}$$

$$= \vec{E}_{\mathrm{ins}} d_{\mathrm{ins}} + \vec{E}_{\mathrm{air}} g_0 \tag{5.18}$$

$$= \frac{\vec{D}}{\epsilon_{\mathrm{ins}}} d_{\mathrm{ins}} + \frac{\vec{D}}{\epsilon_{\mathrm{air}}} g = \vec{D}\left(\frac{\epsilon_{\mathrm{air}} d_{\mathrm{ins}} + \epsilon_{\mathrm{ins}} g}{\epsilon_{\mathrm{ins}}\epsilon_{\mathrm{air}}}\right) \tag{5.19}$$

So the displacement vector $\vec{D}$ is be expressed as:

$$\vec{D} = \frac{V_{\mathrm{DC}}\epsilon_{\mathrm{ins}}\epsilon_{\mathrm{air}}}{\epsilon_{\mathrm{air}}d_{\mathrm{ins}} + \epsilon_{\mathrm{ins}}g} \tag{5.20}$$

Now the electric field in the air gap can be derived from the displacement vector $\vec{D}$ and the force on the plate can be calculated:

$$\vec{E}_{\mathrm{air}} = \frac{V_{\mathrm{DC}}\epsilon_{\mathrm{ins}}}{\epsilon_{\mathrm{air}}d_{\mathrm{ins}} + \epsilon_{\mathrm{ins}}g_0} \tag{5.21}$$

$$\vec{F}_{\mathrm{e}} = \frac{\epsilon_{\mathrm{air}}\vec{E}_{\mathrm{air}}{}^2 A_{\mathrm{cap}}}{2} = \frac{\epsilon_{\mathrm{air}}\epsilon_{\mathrm{ins}}{}^2 V_{\mathrm{DC}}{}^2 A_{\mathrm{cap}}}{2(\epsilon_{\mathrm{air}}d_{\mathrm{ins}} + \epsilon_{\mathrm{ins}}g_0)^2} \tag{5.22}$$

If this electric force is considered for a small slice width w_{t} and length $\mathrm{d}x$, and gap $g(x) = g_0 - y(x)$, the distributed electrostatic force $q_{\mathrm{elec}}(x)$ is expressed as:

$$q_{\mathrm{elec}}(x) = \frac{\epsilon_{\mathrm{air}}\epsilon_{\mathrm{ins}}{}^2 V_{\mathrm{DC}}{}^2 w_{\mathrm{t}}\,\mathrm{d}x}{2(\epsilon_{\mathrm{air}}d_{\mathrm{ins}} + \epsilon_{\mathrm{ins}}(g_0 - y(x)))^2} \tag{5.23}$$

If we substitute equation (5.23) in equation (5.8) and perform the same steps as were described in equations (5.10) to (5.14), the required voltage for equilibrium for a given deflection is:

$$V_{\mathrm{DC}} = \sqrt{\frac{12\hat{E}Iy(L_{\text{c-el}})}{\epsilon_{\mathrm{air}}\epsilon_{\mathrm{ins}}{}^2 w_{\mathrm{eff}}\int_{L_{\text{c-el}}-\alpha L_{\text{c-el}}}^{L_{\text{c-el}}} \frac{x^2(3L_{\text{c-el}}-x)}{(\epsilon_{\mathrm{air}}d_{\mathrm{ins}}+\epsilon_{\mathrm{ins}}(g_0-y(x)))^2}\,\mathrm{d}x}} \tag{5.24}$$

The deflection at the tip $y(L_{\mathrm{tip}})$ is found by linearly extrapolating the deflection at $y(L_{\text{c-el}})$:

$$y(L_{\mathrm{tip}}) = y(L_{\text{c-el}}) + \frac{\mathrm{d}y(x)}{\mathrm{d}x}\Big|_{L_{\text{c-el}}}(L_{\mathrm{tip}} - L_{\text{c-el}}) \tag{5.25}$$

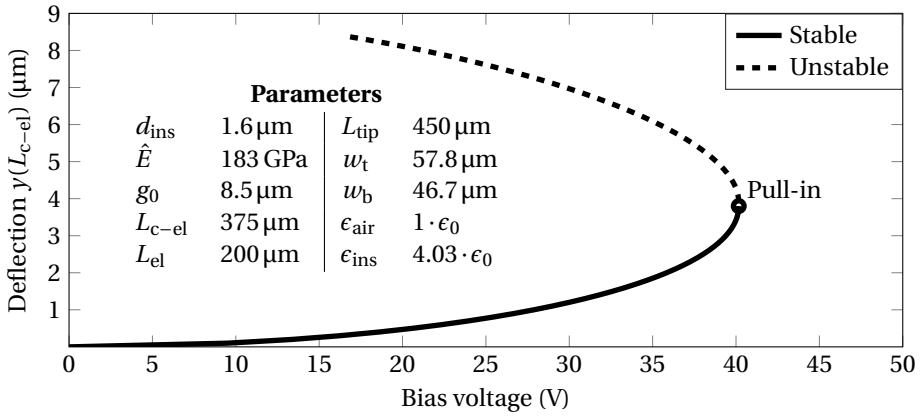

Figure 5.6: The result of equation (5.25). The parameters which are used are shown in the figure. The solid line indicates the stable state of the system, while the dashed line shows the unstable solution of the system. At pull-in, the electrostatic forces exceed the mechanical restoring forces.

5.3. COMSOL MODEL

A 3D COMSOL model has been developed, such that the voltage-deflection behavior can be modeled for the design and the pull-in voltage can be calculated. A 2D model provides insufficient details compared to a 3D model, because the fringe fields and asymmetric electrode as shown in figure 5.7 cannot be taken into account in such a model. In this section the model is presented. The details of this model are found in appendix D.

5.3.1. MODELING

The geometry of the cantilever is modeled according to measurements that are defined in section 5.1. The 3D model is shown in figure 5.7. The electromechanics physics are used to model the system; the base of the cantilever is defined as a fixed constrained as shown in figure 5.7, the electrodes are defined as the electrical ground and the voltage is applied to the entire surface of the cantilever.

In order to determine the pull-in voltage of the system, an inverse problem is solved. Instead of applying a certain voltage and determining the deflection, a deflection Z_{set} is applied to the cantilever (at the tip position), and the required bias voltage for equilibrium is calculated. This method is based on 'Pull-in Voltage for a Biased Resonator' from the COMSOL library [10]. When the pull-in voltage is found from this study, a voltage-deflection study is performed up to this point. A range of voltages is applied, and the resulting deflection is simulated.

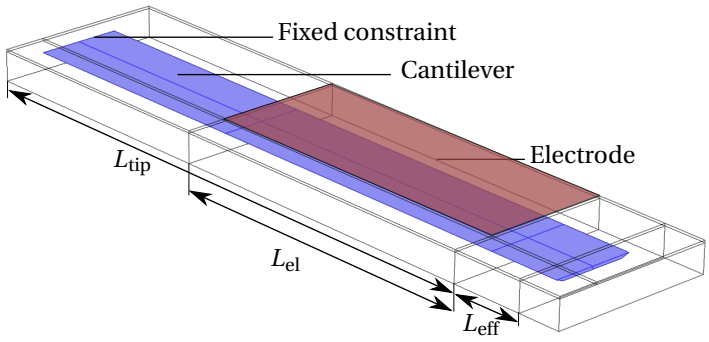

Figure 5.7: 3D COMSOL model with the cantilever and electrodes indicated.

5.3.2. RESULTS

The result of the simulation is a voltage-set point relation as shown in figure 5.8a. The pull-in voltage is at the maximum of this plot; up to this point the system is stable, but after this maximum the system is unstable. Now that the pull-in voltage is known, the voltage-deflection relation is simulated in a separate study, up to the calculated pull-in voltage as shown in figure 5.8b. A 3D representation of the cantilever with maximum deflection before pull-in is shown in figure 5.9. A 2D plot of the potential in the system is shown for two cross sections in figure 5.10.

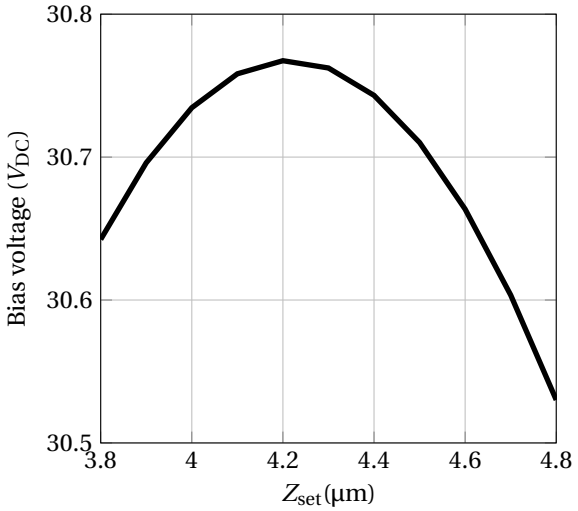

(a) The required bias voltage for equilibrium as a function of the deflection of the cantilever.

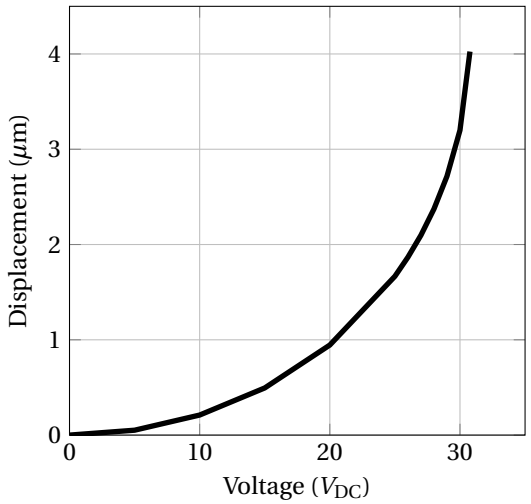

(b) Deflection of the cantilever as a function of the voltage.

Figure 5.8: Results of the COMSOL simulation.

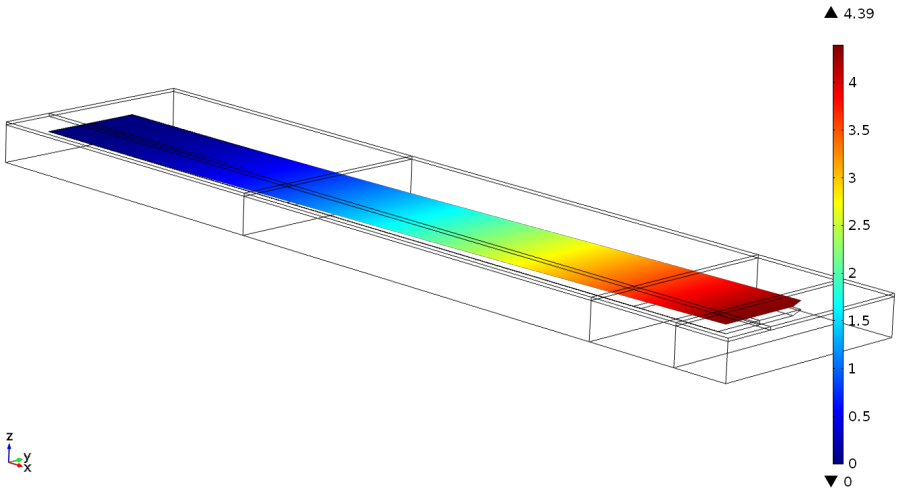

Figure 5.9: 3D representation of cantilever with maximum displacement before pull-in. Deflection is in µm

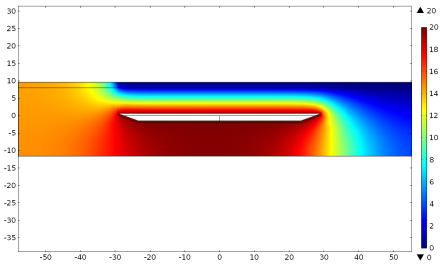

(a) ZY plane cut. Along the width of the cantilever.

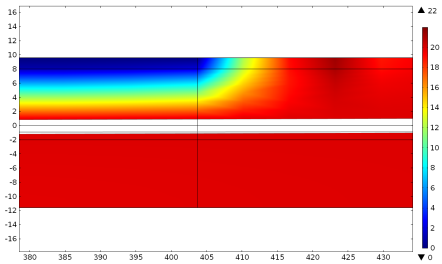

(b) XZ plane cut. Along the length of the cantilever. Zoomed in near the edge of the cantilever.

Figure 5.10: Plane cuts from COMSOL results at 20 V.

5.4. COMPARISON OF THE MODELS

In order to check whether the analytical- and COMSOL are correct, these models are compared. If the results are similar, it is likely that they are correct. The analytical model is based on a shape function (equation (5.16)), which was extracted from FEM results by Do *et al.* [1]. In figure 5.11 the shape of the analytical model and COMSOL model are compared for three different values of tip deflection ($y(L_{\text{tip}})$). The shapes are very similar. The difference between the shape functions is shown in figure 5.12. The difference between the shapes increases for an increasing tip deflection. The maximum error for these shape functions is 15%, which is located at 120 µm. In the experiments, the electrode is covering the cantilever between ~ 141 µm and ~ 370 µm. The shape function only has an influence on the voltage-deflection behavior between this range. The error between this range is smaller than the maximum error. It is concluded that the used function is an appropriate approximation for the shape of the cantilever.

In figure 5.13a the deflection at the tip of the cantilever $y(L_{\text{tip}})$ is shown as a function of the voltage. The two models give a very similar result. The COMSOL model has a slightly higher deflection for any given voltage. The analytical model only considers fringe field effects along the length of the cantilever, while in the COMSOL model the fringe fields along the width of the cantilever are also taken into account as shown in figures 5.13b to 5.13d. These fringe fields add an extra electrostatic force to the system, yielding a slightly higher force for the same voltage for the COMSOL model.

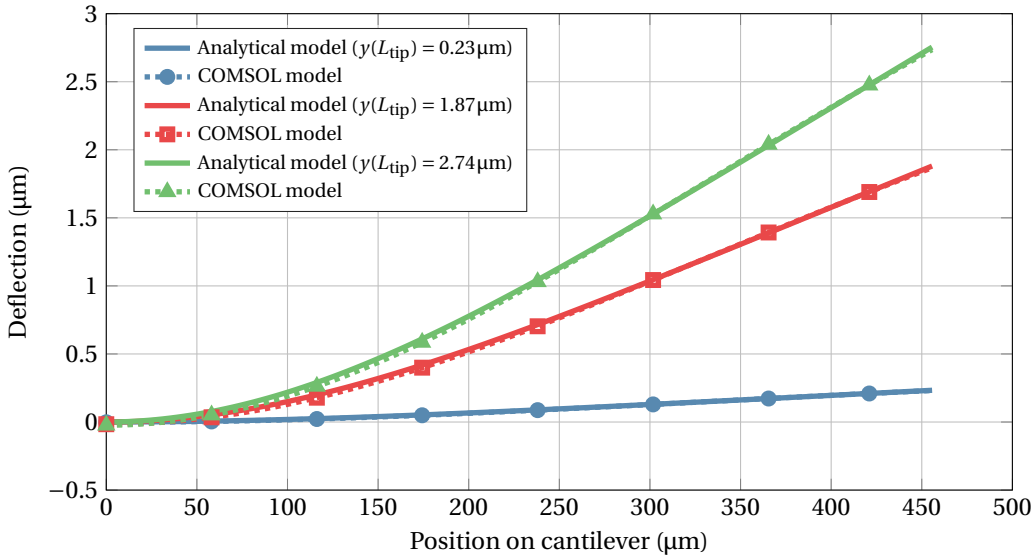

Figure 5.11: Comparison between the analytical model and COMSOL model on the shape of the cantilever for a varying deflection.

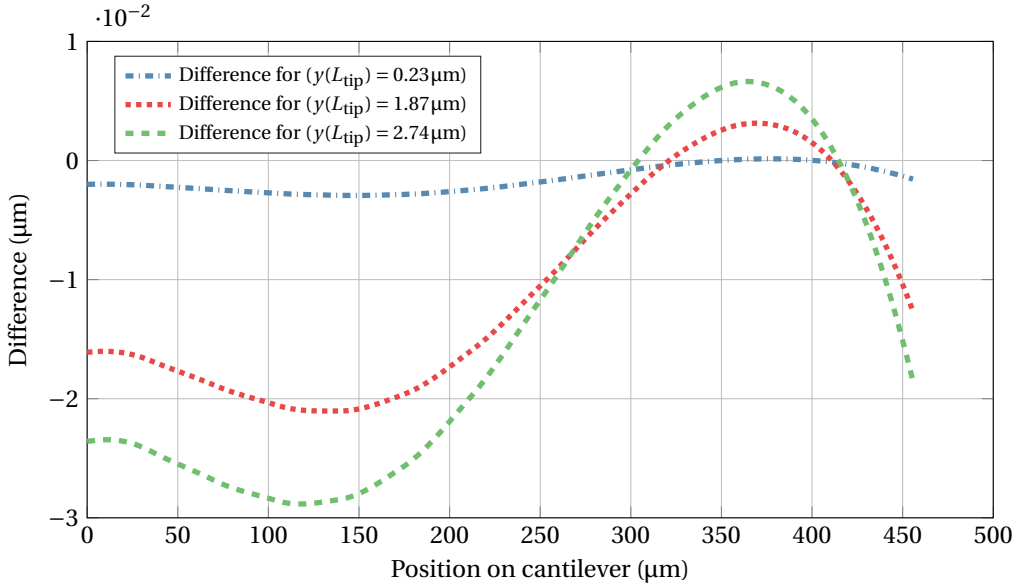

Figure 5.12: The difference between the analytical model and COMSOL model. These plots represent the difference between the corresponding lines of figure 5.11. The difference, expressed as a percentage is constant for all three.

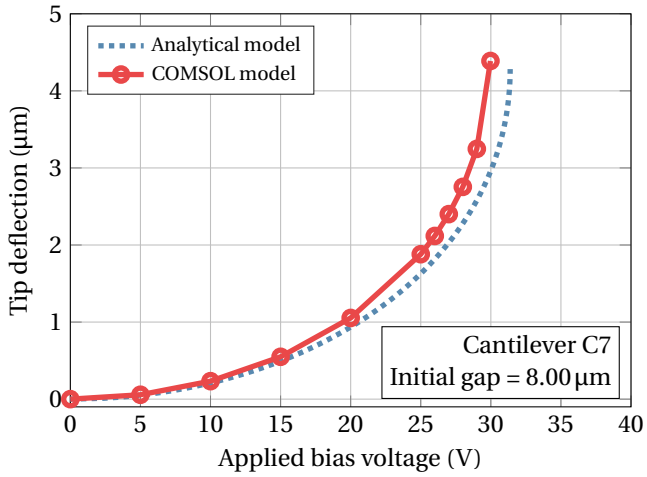

(a) The voltage-deflection behavior of a cantilever. The deflection at the tip is plotted versus the applied voltage.

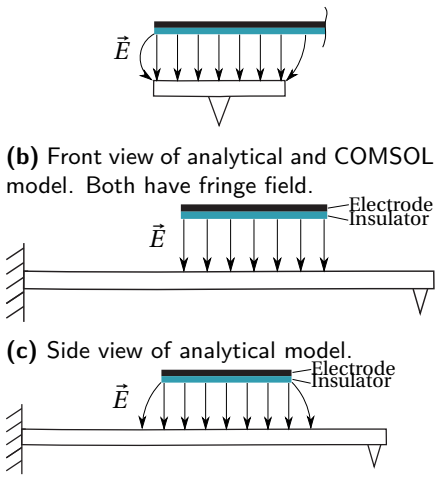

(b) Front view of analytical and COMSOL model. Both have fringe field.

(c) Side view of analytical model.

(d) Side view COMSOL model.

Figure 5.13: The assumptions on the fringe fields for the COMSOL- and analytical model are shown in figures 5.13b to 5.13d. The analytical model assumes that there are no fringe fields near the edges of the electrode along the width of the cantilever. This is possibly the cause of the difference between the voltage-deflection behavior which is shown in figure 5.13a

5.5. EXPERIMENTAL VALIDATION OF THE MODELS

In order to validate the models that were developed in sections 5.2 to 5.4 an experiment was conducted. The materials and methods for this experiment are shown in section 5.5.1. The results are shown in section 5.5.2 and will be discussed in section 5.5.3. The conclusions are found in section 5.5.4.

5.5.1. MATERIALS AND METHODS

First, the components of the experimental setup will be discussed in sections 5.5.1.1 to 5.5.1.6. The integration of these components is discussed in section 5.5.1.7. Next, the measurement procedure and data processing are discussed in section 5.5.1.8.

5.5.1.1. AFM PROBES

Commercially available cantilevers were used for the experiment. In order to reduce the required voltage for snap in cantilevers with a low stiffness and large top surface area were selected. The low stiffness reduces the required electrostatic force for pull-in. The large top surface area results in a relatively large electrostatic force. The used cantilevers are ContAl probes, manufactured by BudgetSensors. More details are found in section 5.1.

5.5.1.2. ELECTRODES

The electrodes used for this experiments are made out of 150 µm thick spring steel and are machined using a LionMetal laser cutter, which was available at the PBM work shop at the faculty of Mechanical Engineering at Delft University of Technology. This laser cutter is not intended for micro meter accuracy, but by tuning the settings of the machine it was possible to manufacture sufficiently small features. The design of the electrodes is shown in figure 5.14a. This design was made in Solid Works, and exported to a *'.dxf'*-file that can be read by the laser cutter. The strips of spring steel were secured on a 5 mm thick steel plate with tape and was placed in the machine as shown in figure 5.14b. The resulting strip of spring steel is shown in figure 5.14c. The resulting beams had a large variability of quality. Some of the beams broke during cutting, due to the strong air flow near the nozzle. Others were much wider or thinner than average. This is because the machine was operating at the edge of its capabilities. The beams were examined in the Scanning Electron Microscope (SEM) as shown in figure 5.15a. On the side of the nozzle there is a clean edge and surface. But on the other side, solidified metal forms a rough edge. The clean side is usable as electrode for the experiments.

In order to be able to focus both the electrode and the cantilever in the optical microscope during the experiments, the end surface of the electrode should be as straight and smooth as possible, such that it remains within the focal depth of the microscope. In order to achieve this, the end of the electrode were cut with sharp pliers, and smoothed with sand paper. Afterwards they were cleaned with ultra sound in DI water (6 min) and iso propanol alcohol (IPA) (6 min).

The insulative coating was applied at the clean room facilities of EKL at Delft University of Technology. Photoresist was chosen as insulator, because it is cheap, easily applicable and has a high dielectric strength. The breakdown voltage is specified as $694\,\mathrm{V\mu m^{-1}}$. But in practice this might be significantly lower due to bad film quality. It was applied with an EVG 101 spray coater, using a 4 layer 1000 mbar 2 mL recipe. The electrodes were mounted on a wafer with Kapton Tape, as shown in figure 5.15b. It was baked in an oven for one hour at 110 °C and one hour at 160 °C. The resulting surface was not as good as expected. Most of the beams had small circular areas that were not covered with photo resist as shown in figure 5.16a. But the layer is good enough to prevent an electrical connection between the cantilever and electrode. The thickness of the insulative layer was measured with a Bruker Dektak Stylus profiler. A scratch was carefully made on the wafer to locally remove the photoresist. A profile measurement was made perpendicular to this line. A typical measurement is shown in figure 5.16b. The average thickness over nine points was 1.60 µm (σ = 0.078 µm).

5.5.1.3. NANOMANIPULATOR

In order to position the electrode relative to the cantilever, a miBot™robotic nanomanipulator is used. This robot can be positioned in-plane with a minimum resolution of 1.5 nm and a maximum speed of $2.5\,\mathrm{mm\,s^{-1}}$.

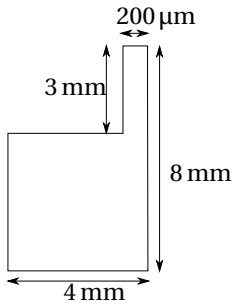

(a) Design of the electrode for the laser cutter.

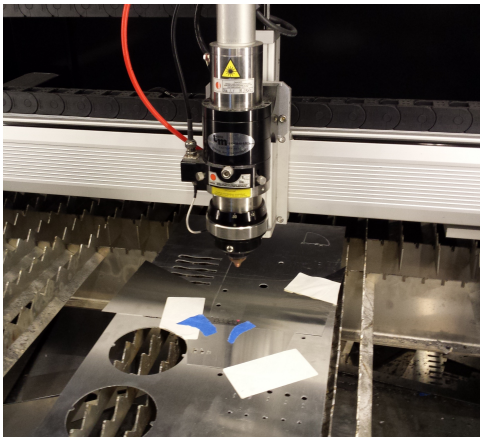

(b) The strip of spring steel secured on a plate of steel in the laser cutter chamber.

(c) Result of the strip of spring steel after laser cutting.

Figure 5.14: Manufacturing of the electrodes from spring steel with a laser cutter.

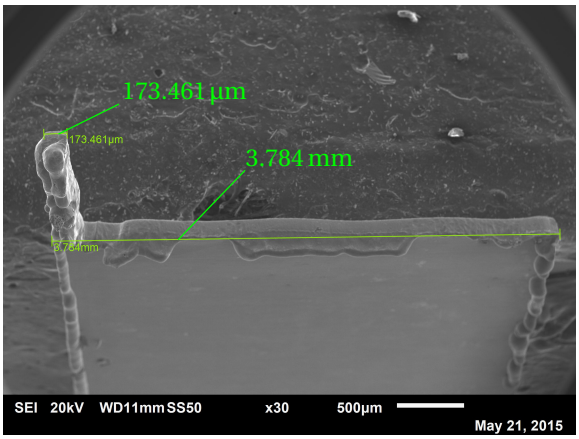

(a) SEM micrograph of the laser cut stainless steel part. The rough edges are solidified droplets of metal. These are formed on the opposite side of the nozzle of the cutter.

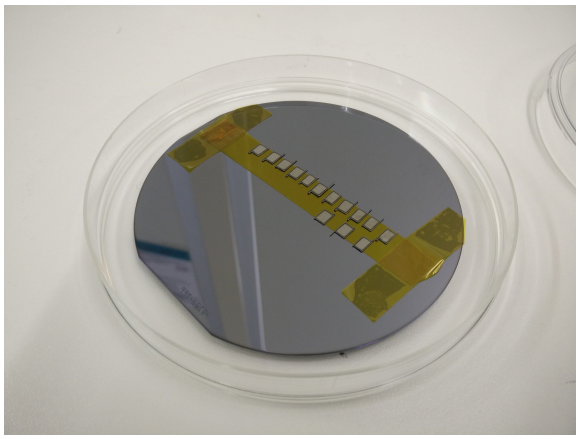

(b) Electrodes secured to a wafer with Kapton tape, before being processed in the spray coater.

Figure 5.15: The result of the electrode after laser cutting (a). The electrodes on a wafer before spray coating photo resist (b).

The robot has an arm which can rotate around its actuator. It has a minimum resolution of 0.24 nrad and a maximum rotating speed of 150 mrad s^{-1} [11]. The robot is connected to a controller box, which is connected to a computer. An external game controller, that is connected to the computer as well, is used as input device. The electrode is connected to the arm of the robot using double sided non-conductive tape.

5.5.1.4. COMPLIANT HINGE

The nano-manipulator can vertically position the electrode. The angle of this electrode is uncontrolled though as shown in figure 5.18. So in order to be adjust the angle of the cantilever relative to the electrode a compliant hinge was made. The schematic drawing of this compliant hinge is shown in figure 5.17. The hinge is made from spring steel and is cut with metal scissors. The holes are punched. The nut is secured with super glue. The metal hinge is placed on a microscope glass with double sided tape. The prototyping PCB is secured with double sided tape as well.

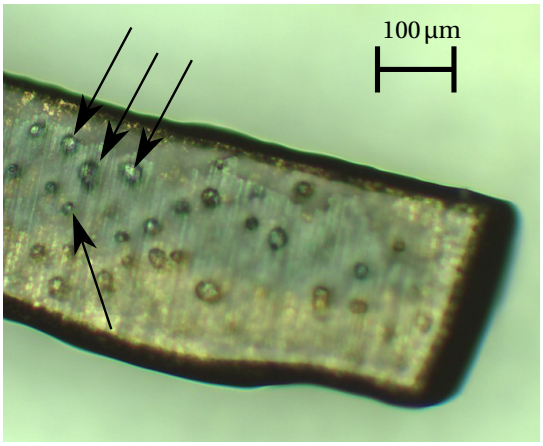

(a) Micrograph of the electrode surface. The layer of photo resist is not homogeneous. Small circular areas appear not to be covered. A few of these areas are indicated with the arrows.

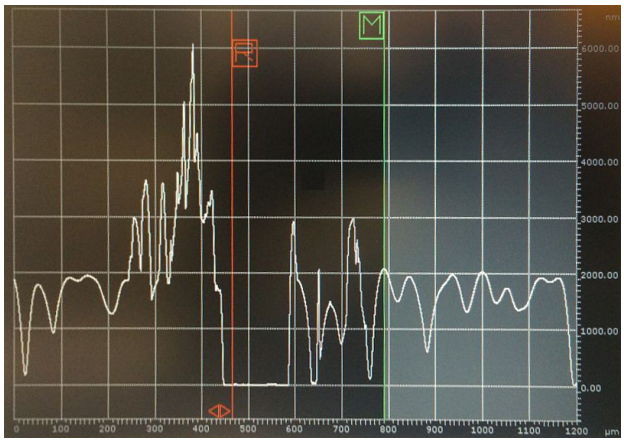

(b) Typical Bruker Dektak profile measurement on the wafer to determine the photoresist layer thickness. A scratch is made in the photo resist and a transverse measurement is done. The red line indicates the location of the scratch, the selected part between 800 and 1200 µm is the where the average value is taken.

Figure 5.16: Micro graph of electrode surface with photo resist (a). Dektak measurement of spray coated photo resist after baking (b).

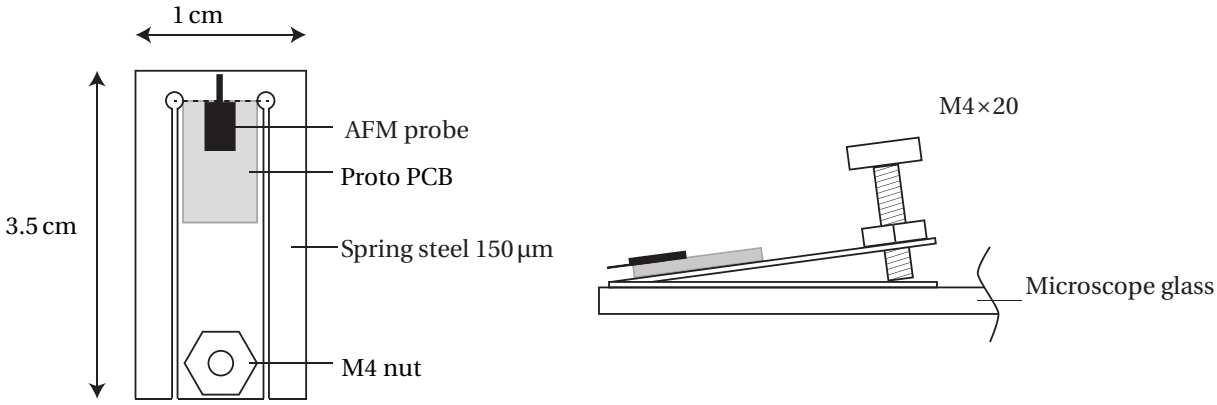

Figure 5.17: The compliant hinge, used to introduce an extra degree of freedom. The left- and right side of the hinge is connected to a microscope glass with double sided tape to give it the required stiffness. The PCB is also connected to the hinge with tape. The nut is fixed to the hinge with super glue. By turning the screw, the angle of the cantilever, relative to the electrode, can be adjusted.

5.5.1.5. ELECTRONICS

As a voltage source, two 'Delta Elektronika ES 030-5' power supplies are used. They can deliver 30 V each. The voltage sources are connected in series, so a total of 60 V can be obtained. The negative side is connected to the ground, and the positive side to a resistor. This resistor is included for safety measures: If the electrode and cantilever would make electrical contact, the current is limited. It is intended to keep the maximum current though the cantilever below 1 mA, such that the temperature due to Joule heating is limited. This current is common in micro systems, so the cantilever should survive this. The resistance of the circuit itself (R_{circ}) is measured by bringing an electrode without photo resist into contact with the cantilever, and measuring the resistance with a multimeter. This yields 70 Ω. So in order to have a maximum current of 1 mA for the maximum voltage of 60 V:

$$R_{\text{PR}} + R_{\text{circ}} = \frac{U}{I} \tag{5.26}$$

$$R_{\mathrm{PR}} = \frac{60}{0.001} - 70 = 59\,930\,\Omega \tag{5.27}$$

The closest available resistance that was a resistor of 68 kΩ.

The electrode is connected to the negative pole of the voltage source and the ground. The electrode is connected to the robot arm with double sided tape. A small piece of prototyping PCB of approximately 5 × 5 mm is connected with double sided tape to the top of the robot. An aluminum wire with a diameter of 30 µm connects the PCB and the electrode. The connection is secured with conductive silver paint. A wire is soldered to the PCB and connects the voltage source. Because the voltage sources are not directly next to the setup, a coax cable is used to connect the source to the setup. This shields the cables from electric and magnetic fields from outside, and provides a clean and compact connection.

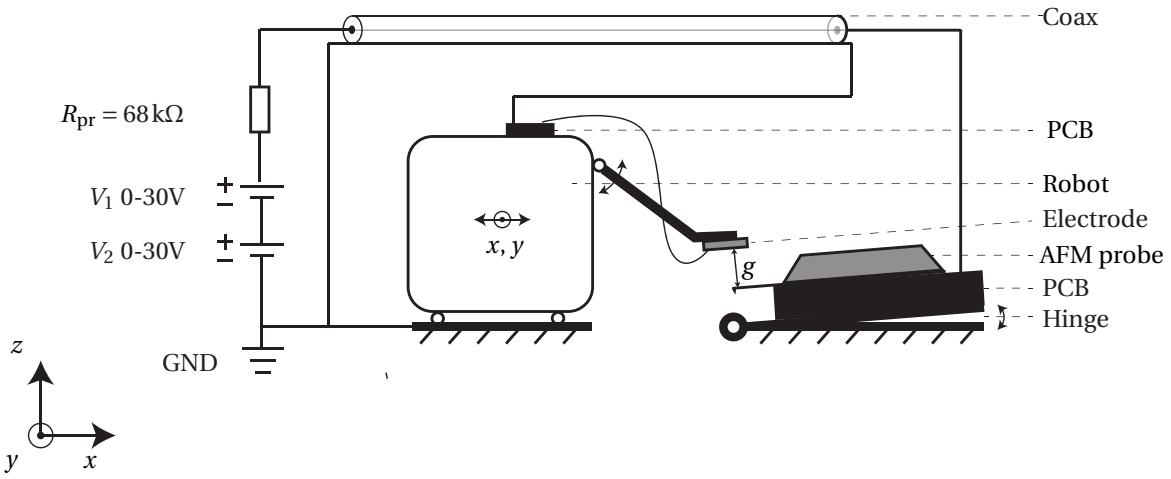

Figure 5.18: A side view of the experimental setup with the robot, electrode, AFM probe, hinge and electronic components.

5.5.1.6. MICROSCOPE

A Motic microscope is used to monitor the system and to take images from the deflecting cantilever. The 'Motic Image Plus 2.0' software is used to acquire screen shots of the system. The software is calibrated with a calibration slide, to determine the size of the pixels for the different objectives. The objective of the microscope points on top of the cantilever. The cantilever is deflecting perpendicular to the optical axis. In order to be able to observe this, a 45° mirror is used, which is placed close to the cantilever.

5.5.1.7. INTEGRATION OF COMPONENTS

The integration of the components is shown in figure 5.19. The nano manipulator is on a metal 'arena', in order for in plane actuator to work at its best. The robot has a flat ribbon connector on the back, that goes to an adapter which is connected to the controller box. The coax connector is secured with tape on the microscope stage, to prevent pulling on the wires during measurement. The cantilever is glued with conductive silver paint to a small plate of prototyping PCB with a conductive top layer. The wire that goes to the voltage source is soldered to the same plate.

5.5.1.8. MEASUREMENT METHOD AND DATA PROCESSING

The goal of this experiment is to measure the voltage-deflection behavior of the cantilever to confirm the validity of the models. The measurement data is gathered as follows:

- Make sure that all the components are connected correctly and that the equipment is switched on.
- Manually bring the robot close to the AFM probe.

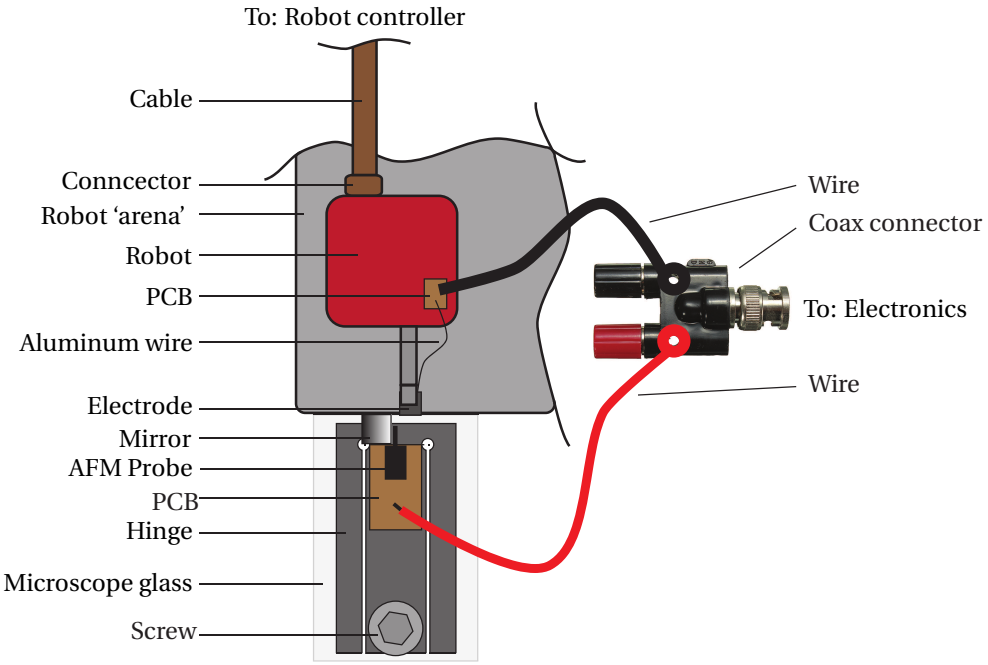

Figure 5.19: A top view of the experimental setup with the main components. The microscope has the same view on the setup as the view in this figure. The electronics are shown in figure 5.18

- Make sure that the electrode is above the cantilever. Use the miBot controller to bring the electrode close to the cantilever. And align the electrode with the cantilever in top-view. Approximate alignment is sufficient for this step.
- Go to side-view of the cantilever by looking through the mirror. Lower the electrode and approach the cantilever to $\sim 50\,\mu m$.
- Focus on the cantilever. Use the in plane motion of the robot to bring the edge of the electrode to the same focal plane.
- Rotate the camera of the microscope, such that the electrode is horizontally aligned on the computer screen. The grid in the microscope software can be used as a reference.
- Raise the arm of the robot such that the electrode is far away from the cantilever.
- Use the compliant hinge to bring the cantilever in a horizontal position relative to the grid, such that it becomes parallel to the electrode.
- Bring the electrode to the required position for the experiment, and verify if the cantilever and electrode are parallel and horizontal.
- Apply the required bias voltage with the voltage sources and make screen shots with the microscope software. Increase the voltage to the next value and repeat until the cantilever is pulled-in.

A number of images is collected, that correspond to a known, varying, bias voltage. A typical measurement is shown in appendix C. The next step is to post-process these images, to get the voltage-cantilever deformation relation. This was done with Matlab. The basic idea is to compare the images of the cantilever under a bias voltage with the 0 V-image. An optical displacement technique, developed by Kokorian et al. [12] was used to achieve sub-pixel resolution displacement measurements.

Optical displacement measurement method The goal of the measurement is to track the measurement point as a function of the bias voltage. This is done by converting the image to gray scale, and looking at the pixel intensity profile along the direction of motion. This is illustrated in figure 5.20. This method uses the

fact that the shape of this intensity profile remains constant while the cantilever deflects. The shape of the intensity profile is compared for the subsequent images.

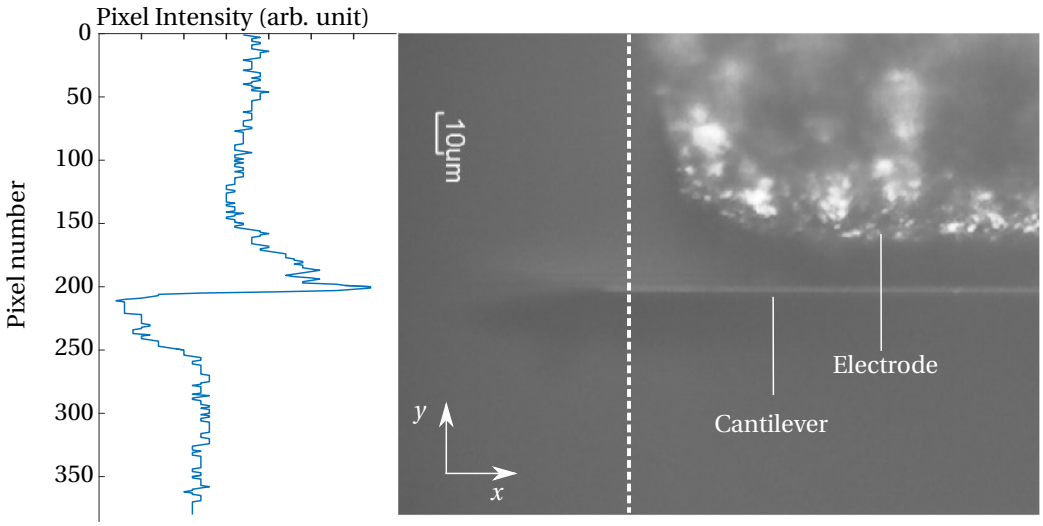

Figure 5.20: The converted gray scale image with the pixel intensity profile along the dashed line. When the cantilever will deflect, the shape of this peak will remain the same, but the position will change.

First, the intensity profile is averaged for 10 pixels. Then a mathematical function $s(x)$ is generated to describe the peak of the cantilever at 0 V. This is the reference image for the measurement. A spline-based template function is used; this is a numerical function with piecewise polynomial functions. These functions are connected in the 'knots'. In between these knots, a cubic line is fitted. The derivatives of two segments in one knot are equal, such that a smooth function is generated. In order to determine the deformation, the intensity profile of the next image is compared with a shifted version of the spline $s'_{x_0} = s(x - x_0)$, where x_0 is chosen such that the spline fits the new intensity profile. In figure 5.21 a typical dataset can be found. The original data, and the fitted spline function $s(x)$ are shown. An intensity profile of a deformed cantilever is added to this figure. The shift x_0 is calculated by solving a least square problem:

$$\text{minimize} \sum_{i=1}^{n} \left(s(x_i - x_0) - I_{\text{def}_i} \right)^2 \tag{5.28}$$

Where i is the i-th pixel, x_0 the shift of the spline and I_{def_i} is the i-th pixel of the intensity profile of the deformed cantilever, n is the number of pixels in the intensity profile. The spline shift x_0 can be converted into micrometers using optical calibration of the microscope.

Measurement error The deflection measurements have a finite accuracy. The error sources are:

- Mechanical error source: The measurement setup is placed on a granite isolation table. This should prevent external vibrations to influence the measurement. It is possible though that mechanical disturbances were transmitted through this isolation table, or that vibrations were induced by the user while performing the measurements. The mechanical loop between the cantilever and electrode is not rigid, which has a negative influence on the measurement. The cantilever and electrode could move relative to each other due to this bad mechanical loop. By measuring the motion of the cantilever, relative to the electrode these error sources are minimized.
- Camera noise: The camera has a limited resolution (3 mega pixels) and is subjected to photon shot noise. This is an error source for the displacement measurement. The pixels of the cantilever and electrode that are used for the measurement are averaged in the horizontal direction, such that optical noise is reduced.

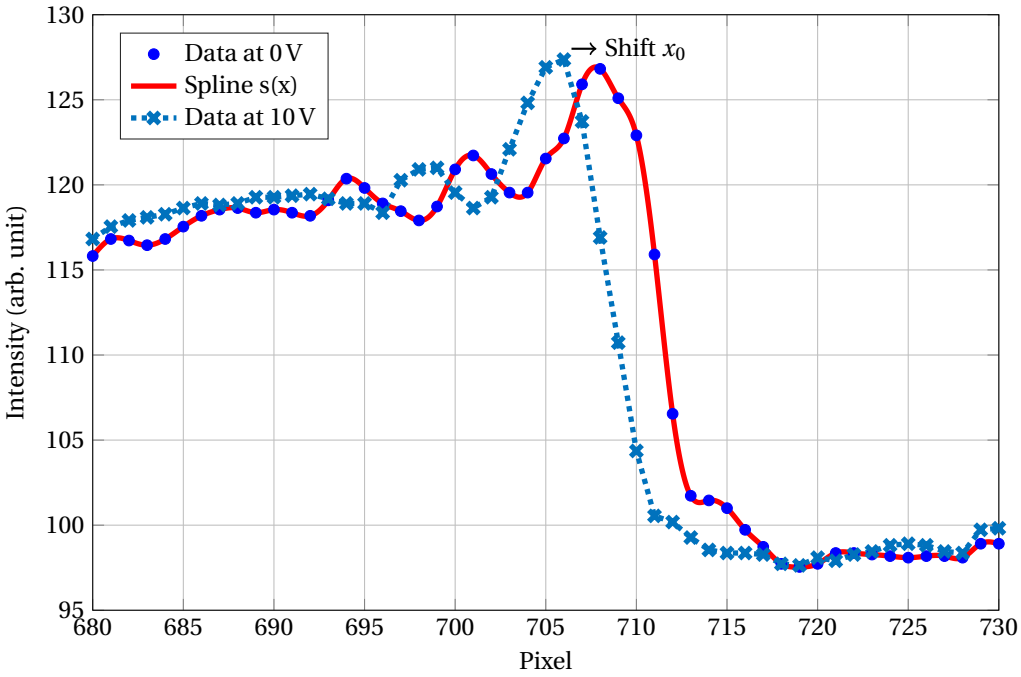

Figure 5.21: The original intensity profile of the reference image at 0 V, and the fitted spline function $s(x)$ are shown in this figure. The intensity profile data of the deformed cantilever is shown in the same figure. In order to calculate the deformation of the cantilever a least square problem is solved, such that a shifted version of the spline $s'(x_0)$ has the best fit with the new dataset. This x_0 is the amount of pixels that the end of the cantilever has deformed; this value does not need to be an integer, and sub-pixel resolution is achieved.

- Optical calibration: In order to convert the displacement of the cantilever in pixels to micro meters, the microscope is optically calibrated with a calibration slide. This calibration is a limit to the resolution of the measurement. The 20× objective that was used for the measurements, was calibrated with a 150 µm circle on the calibration slide. This resulted in 0.3106 µm px^{-1} for the x-direction and 0.3125 µm px^{-1} for the y-direction. The circle is approximately 484 px in diameter and it is estimated that this is at least within ±5 px accuracy. So the confidence interval for the optical calibration is $\frac{5}{484} \cdot 100\% = \pm 1\%$.
- Read-out of voltmeter: A volt meter is used to determine the applied bias voltage. The resolution is limited to two digits up to 20 V and one digit for voltages higher than 20 V.

The largest error source are the optical calibration of the microscope and the resolution of the volt meter. The other error sources will be considered to be negligible compared to these errors. The confidence interval for the bias voltage is ±0.05 V. The confidence interval for the optical calibration is ±1%. The gap between the cantilever and electrode is estimated on pixel-level. It is estimated that this is done within 2 px accuracy, which corresponds with 0.62 µm. The estimate for the gap is used for the models.

Matlab implementation The analytical model, read out of COMSOL results, and optical deflection method are implemented in a MATLAB code. The code and explanation of the code are found in appendix E.

5.5.2. RESULTS

The described experiment was performed for different configurations. A total of 16 datasets were collected. Two electrode positions were used. And for each position two initial gaps g_0 were tested (this is an approximate gap, because the exact gap can only be determined in the post-processing step). For each of these configurations four data sets were collected. These measurements are summarized in table 5.3, where the pull-in deflection and voltage are given. The voltage-deflection behavior for the datasets are compared with the analytical- and COMSOL model in figures 5.22 to 5.25. Typical micrographs that were collected are shown

in figure 5.26. A full data set of micrographs is shown in appendix C.

Table 5.3: The results of the experiments. The maximum deflection before pull-in d and the corresponding voltage V are given for the measurements (subscript 'meas') and model (subscript 'mod'). The difference between measurement and model are indicated for the maximum deflection and voltage. This difference is normalized for the value found in the model. and the averages are expressed as a percentage.

L_{eff}	$g_{0\text{-avg}}$	g_0	d_{mod}	d_{meas}	V_{mod}	V_{meas}	Δd	$\frac{\Delta d}{d_{\text{mod}}}$	$\left(\frac{100\%\cdot\Delta d}{d_{\text{mod}}}\right)_{\text{avg}}$	ΔV	$\frac{\Delta V}{V_{\text{mod}}}$	$\left(\frac{100\%\cdot\Delta V}{V_{\text{mod}}}\right)_{\text{avg}}$
50	8.00	8.034	4.31	3.35	30.82	24	0.96	0.22	15%	6.82	0.23	11%
		7.959	4.26	4.04	30.41	33	0.22	0.05		-2.59	-0.07	
		7.650	4.07	3.52	29.00	26	0.55	0.14		3.00	0.11	
		8.350	4.43	3.56	32.80	28	0.87	0.20		4.80	0.16	
	11.29	11.525	6.16	4.81	52.38	46	1.35	0.22	17%	6.38	0.12	9%
		11.213	5.97	5.14	49.33	49	0.83	0.14		0.33	0.02	
		10.900	5.81	4.73	47.40	42	1.08	0.19		5.40	0.13	
		11.525	6.13	5.38	51.29	48	0.75	0.12		3.29	0.08	
75	8.48	8.088	4.74	4.11	35.47	32	0.63	0.13	19%	3.47	0.11	13%
		8.713	5.09	3.95	39.38	35	1.14	0.22		4.38	0.12	
		8.088	4.74	3.69	35.47	31	1.05	0.22		4.47	0.14	
		9.025	5.26	4.34	41.38	36	0.92	0.18		5.38	0.14	
	10.20	10.588	6.17	5.33	51.86	46	0.84	0.14	16%	5.86	0.13	12%
		9.963	5.80	4.61	47.58	43	1.19	0.21		4.58	0.11	
		9.963	5.80	4.95	47.58	43	0.85	0.15		4.58	0.11	
		10.275	5.99	5.18	49.70	45	0.81	0.14		4.70	0.11	

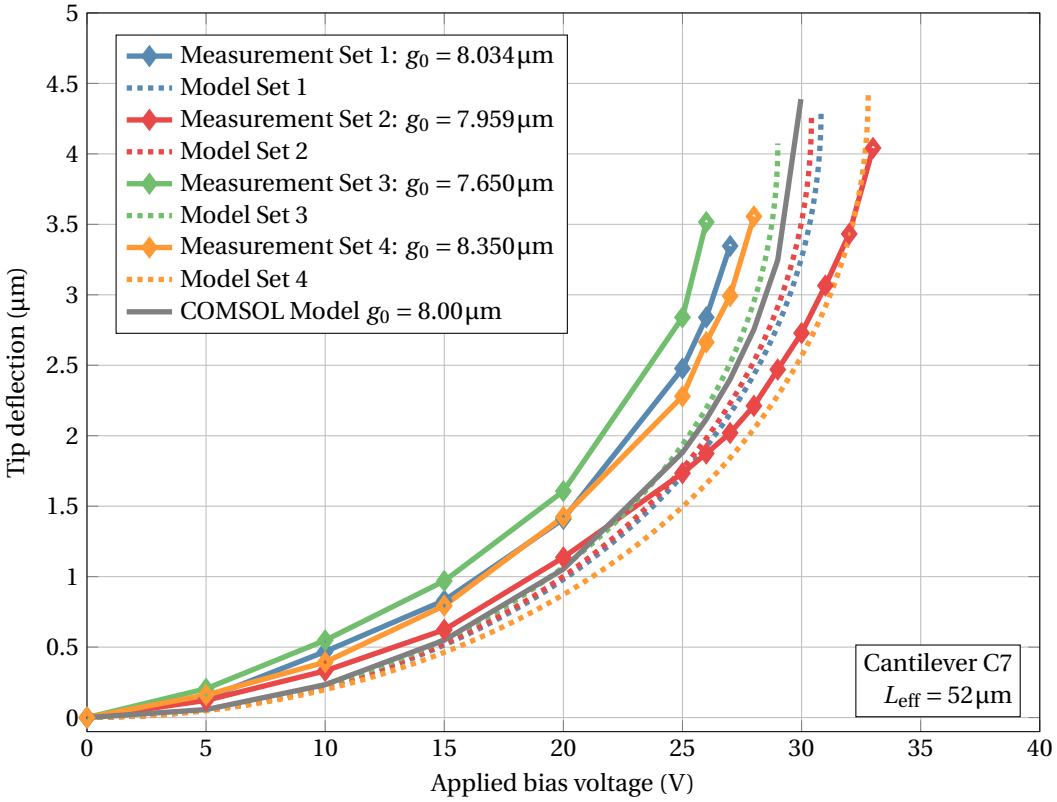

Figure 5.22: Voltage-deflection behavior of typical measurement.

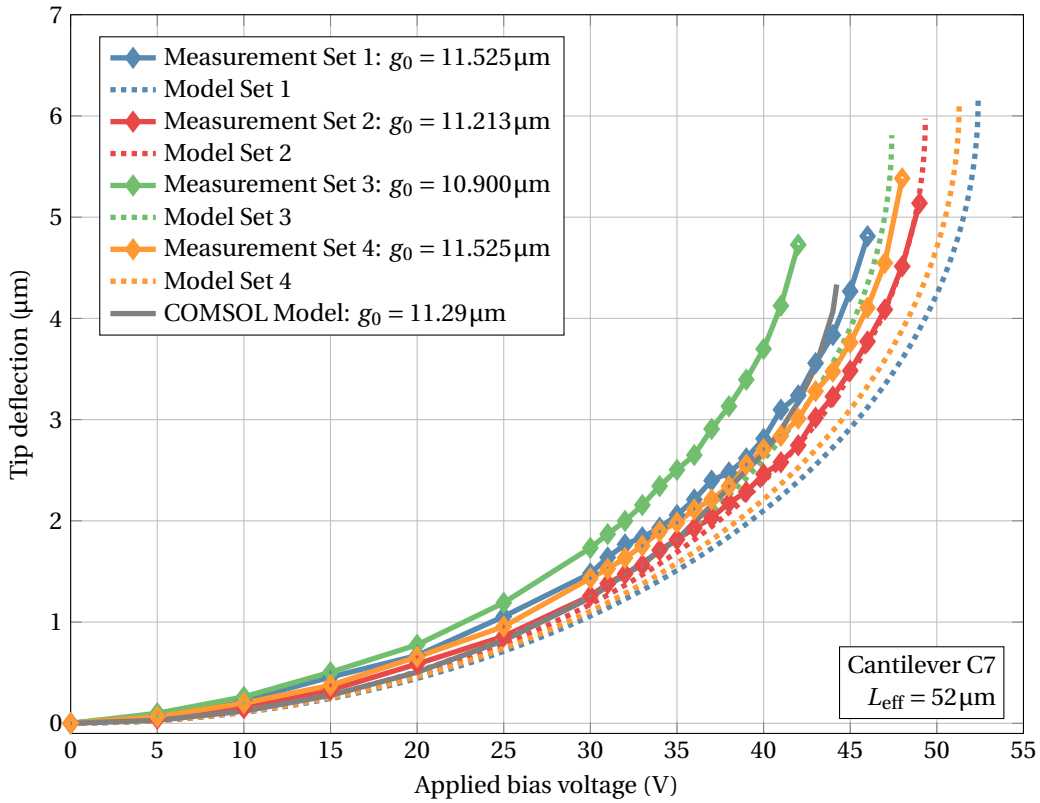

Figure 5.23: Voltage-deflection behavior of typical measurement.

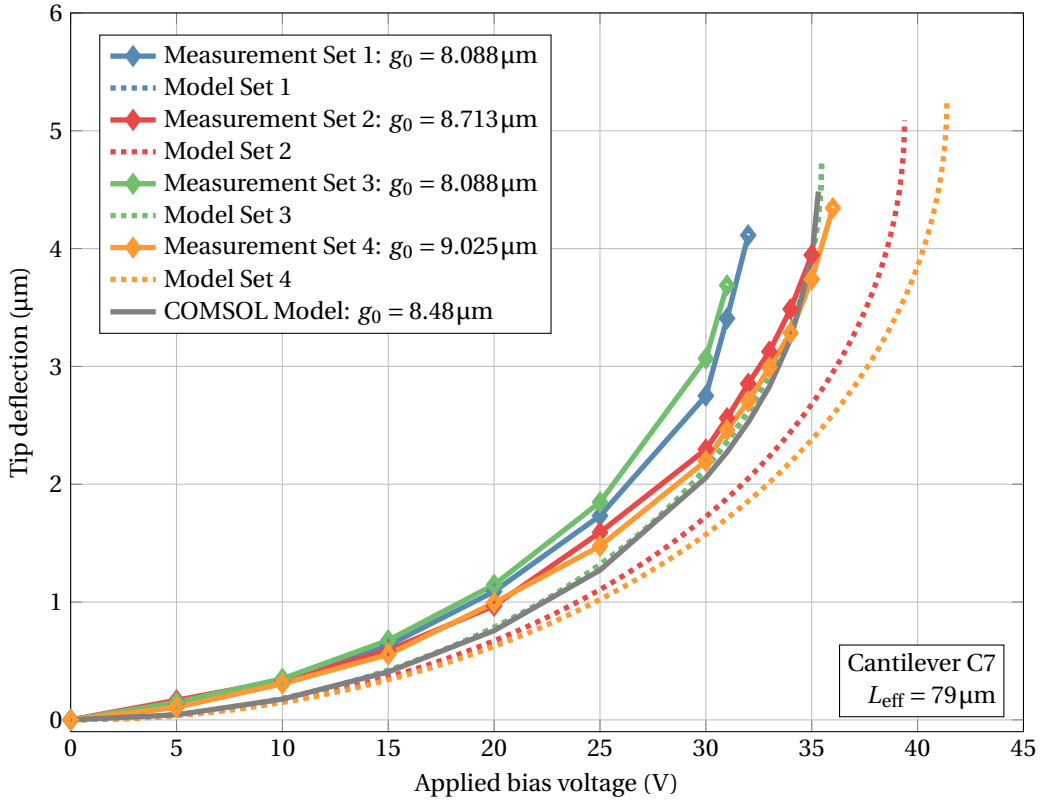

Figure 5.24: Voltage-deflection behavior of typical measurement.

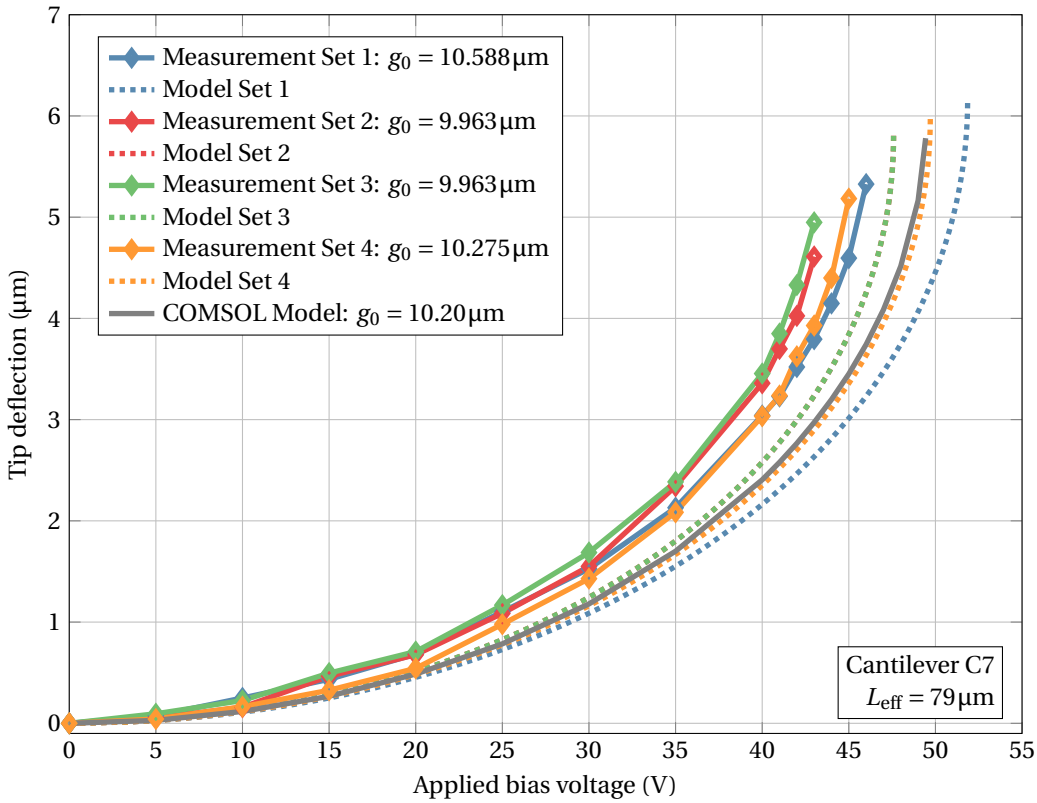

Figure 5.25: Voltage-deflection behavior of typical measurement.

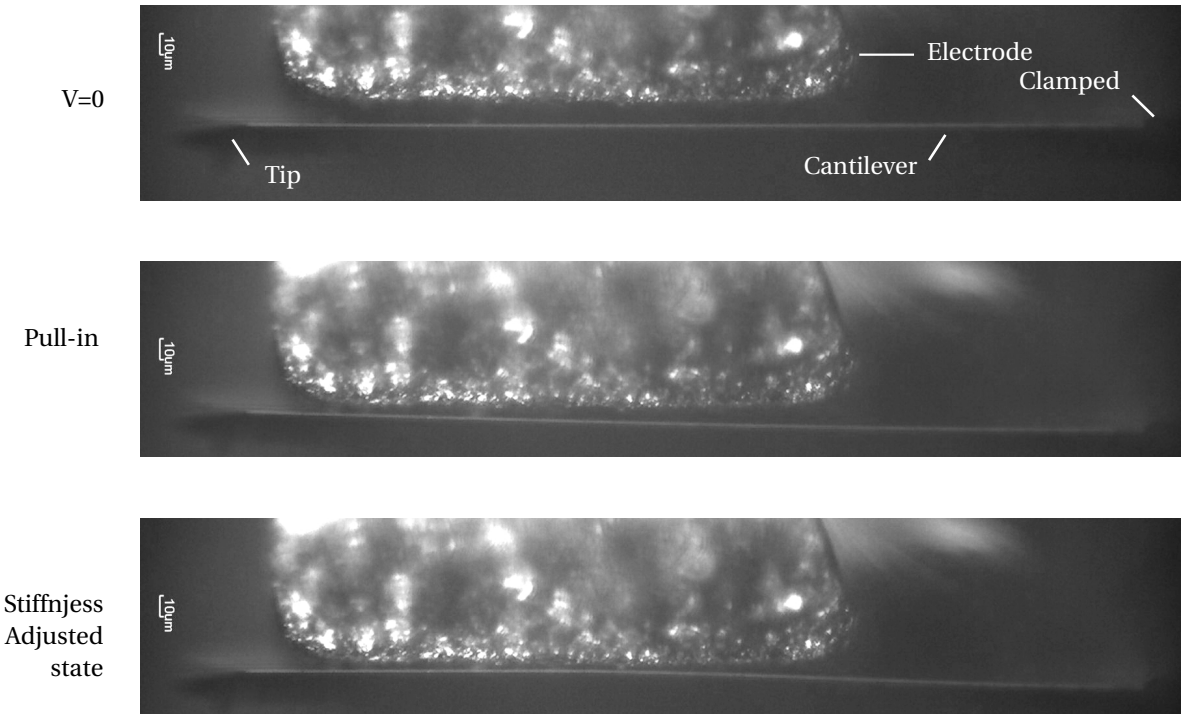

Figure 5.26: Micro graphs of the cantilever under varying bias voltage. For $V = 0$ the cantilever is in neutral state. When $V = V_{PI}$ the cantilever is pulled-in to the electrode. When the voltage is increased further, the cantilever will be in adjusted state.

5.5.3. DISCUSSION

In figures 5.22 to 5.25 the voltage-deflection behavior of the cantilever under an electrostatic load is compared for the models and measurements. For each data set, the measurement is compared with the analytical model, in the same configuration. For each set of four measurements, the COMSOL model is showing the average configuration. For all of the measurements (except for set 2, figure 5.22), the deflection for a given voltage is higher for the measurement compared to the analytical model. So the analytical model underestimates the electrostatic force of the measurement. There are two possible causes for the difference between the analytical model and the measurements. In section 5.4 it was already concluded that the analytical model underestimates the electrostatic force compared to the COMSOL model, because not all the fringe fields are taken into account. Secondly, the shape of the cantilever is approximated by a constant cross section, as was discussed in the introduction of chapter 5. This simplification might lead to an underestimation of the electrostatic force.

There are some other causes that explain the differences between the models and measurements. In the models it is assumed that the electrode is perfectly flat, and that it has sharp edges. In the experimental setup, the edges of the electrode are slightly rounded. It is assumed that those rounded edges do not contribute to the electrostatic force, while they might be of significance.

In table 5.3 the pull-in deflection and corresponding voltages are shown. The pull-in deflection of the model is on average 17% higher than the measurement and the pull-in voltage is 11% higher. The measurement is performed in discrete steps of 1 V. So the actual point of pull-in for the measurement is somewhere between the last measured voltage and 1 V higher. The measurement always underestimates the pull-in voltage. When the system is close to pull-in, a small change in bias voltage causes a large change in deflection. So the underestimation of the deflection at pull-in has a significant influence on the measured pull-in point.

It was observed that when the cantilever pulled-in to the electrode, that it did not end up in the expected configuration. There is a intermediate stable state, where the cantilever is touching the electrode, as shown in figure 5.26. The voltage needs to be increased beyond the pull-in voltage that was found with the analytical- and COMSOL model to reach the desired state. In order to investigate this behavior, a time dependent COMSOL model was developed, to model the behavior after pull-in. This is further elaborated in section 5.6.

5.5.4. CONCLUSIONS

The analytical model can predict the voltage-deflection behavior and pull-in voltage. In all measurements there was an average error of 11% in pull-in voltage and 17% in deflection before pull-in. These differences can be explained by the fact that the measurement is performed in steps of 1 V, and will therefor always underestimate these values. Secondly, the analytical model is underestimating the electrostatic force, most likely due to the fact that not all the fringe fields are taken into account and the cantilever geometry is simplified.

The shape of the electrode is not perfectly flat. The edged are not well defined, and the surface quality is not so good. This introduces effects, that are not included in the model. In order to be able to draw definite conclusions about the model, the experiment should be repeated for a more ideal electrode. The electrode should be perfectly straight and have a well defined edge. This could be achieved by micro machining.

The cantilever does not end up in the required state after pull-in. The voltage needs to be increased beyond the pull-in voltage. The models that were developed in this section give insight into the behavior of the system up to the pull-in voltage. Further investigation on post pull-in behavior should be performed. This is done in section 5.6.

5.6. COMSOL MODEL: 3D TIME DEPENDENT STUDY

In order to gain more insight into the behavior on how the cantilever pulls-in to the electrode, a time dependent simulation was performed. The goal of the simulation is to see how the cantilever is pulled-in to the electrode. This model is based on 'Pull-in of an RF MEMS Switch' of the COMSOL library.

5.6.1. MODELING

The contact between the cantilever and electrode is modeled as a penalty based force, that rapidly increases when the gap between the electrode and cantilever approaches zero. Only half of the cantilever is modeled, using a symmetry plane in the middle of the with of the cantilever. This reduces the computation time. The model is shown in figure 5.27. The mesh which represents the air between the cantilever and electrode is compressed when the cantilever is pull-ed in. This mesh is collapsed into a layer, which has the same thickness as the insulative layer. The insulative layer is not explicitly defined, but is formed by this collapsing mesh. The dielectric constant of this domain is equal to that of air, and rapidly approaches the value of the insulative layer, when the mesh is compressed. The contact between cantilever and electrode is modeled with a penalty based method [13]. The force F_c increases rapidly, when the gap g between cantilever and insulative layer approaches zero. The sign of the force changes, when the gap is smaller than, or equal to zero:

$$F_c = t_n - e_n \cdot g \qquad g \leq 0 \tag{5.29}$$

$$F_c = t_n + \exp\left(-\frac{e_n}{t_n} \cdot g\right) \qquad g > 0 \tag{5.30}$$

With e_n the penalty stiffness and t_n an input estimate of contact force. The voltage is applied in a smooth step, going from zero to the set voltage in 1×10^{-5} s. The simulation is performed with a time dependent study, ranging from $0 - 15 \times 10^{-5}$ s in steps of 2.5×10^{-7} s. The parameters of the system that were used for the simulation is summarized in figure 4.3b. For this configuration, the pull-in voltage is 20.5 V, according to the analytical model. Up to the pull-in voltage the system is studied with a stationary study. Beyond pull-in a time dependent study is performed. The stationary study is performed from zero to pull-in voltage in steps of 1 V. The time dependent study is done in steps of 2 V between the pull-in voltage and 65 V and steps of 5 V up to 85 V.

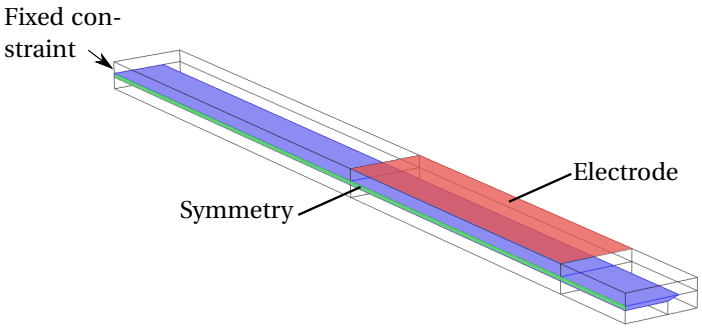

Figure 5.27: Geometry of the COMSOL model for time dependent simulation

5.6.1.1. MESH

The mesh is based on the original model. A quad mesh is applied to the cantilever, and the air at the bottom side as shown in figure 5.28a. This mesh is swept trough the geometry as shown in figure 5.28b. The top surface of the cantilever is swept to the top boundary of the geometry as shown in figure 5.28c.

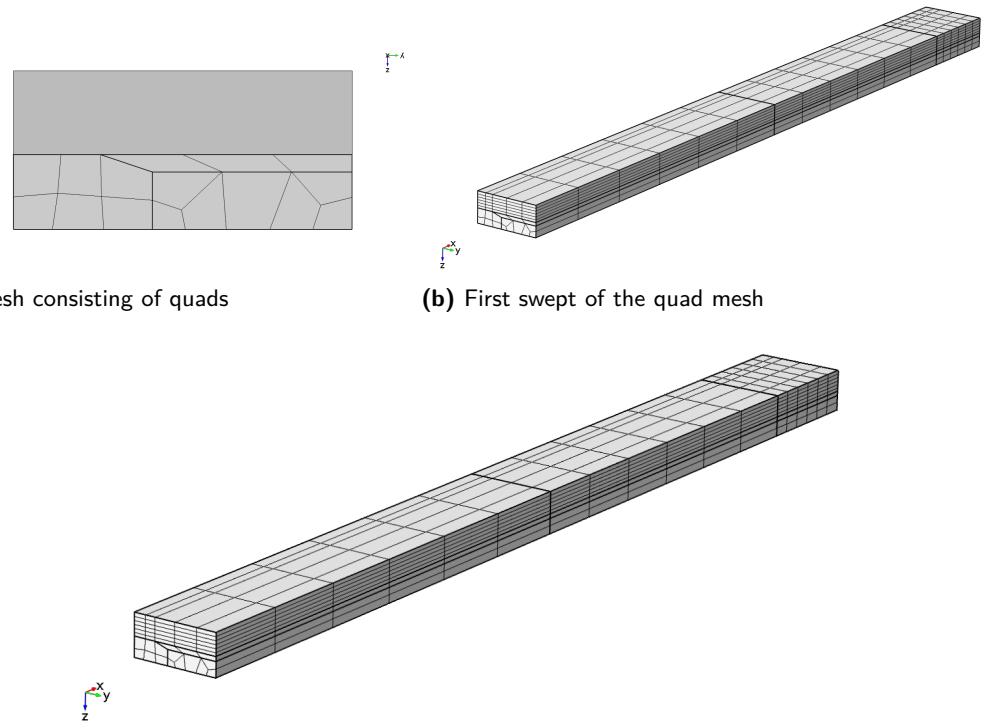

(a) Mesh consisting of quads

(b) First swept of the quad mesh

(c) Swept of the air gap between cantilever and electrode.

Figure 5.28: Mesh of the time dependent COMSOL model.

5.6.2. RESULTS

In section 4.3 the main results of the model are shown. The shape of the cantilever and tip displacement were shown as a function of applied bias voltage. Additional results are shown in this section. In figure 5.29, the tip deflection is shown as a function of time. This is compared for a voltage before pull-in, right after pull-in and beyond pull-in. For voltages higher than pull-in, the damping is higher, due to the contact with the electrode. But for voltages smaller than pull-in, the cantilever keeps oscillating and is only lightly damped. Therefor a static analysis is performed up to pull-in voltage (0-21 V). In figure 5.30 the final, stable states for 35 and 80 V are shown, which are before, right after and way beyond the pull-in voltage of 20.5 V.

5.6.3. DISCUSSION

The pull-in voltage that was found for the time-dependent study was smaller than the one found for the stationary study. In the stationary study, the system finds the maximum deflection where it is still possible to find equilibrium. For any given voltage below pull-in in the time dependent study, the cantilever overshoots the final position that it would have in the stationary study. This is due to inertia. For the stationary study pull-in is at approximately 22 V, for the time dependent at approximately 21 V.

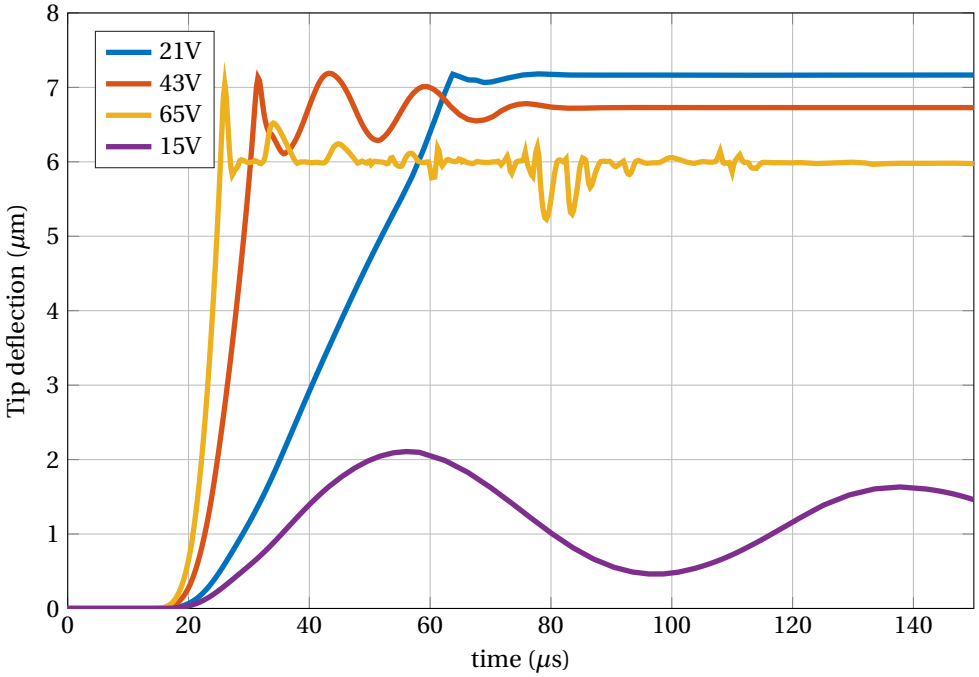

Figure 5.29

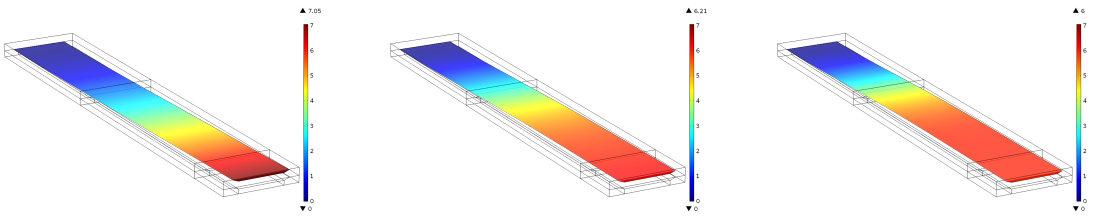

(a) Deflected 3D COMSOL model in steady state for 30 V **(b)** Deflected 3D COMSOL model in steady state for 55 V **(c)** Deflected 3D COMSOL model in steady state for 80 V

Figure 5.30

REFERENCES

[1] C. Do, M. Lishchynska, K. Delaney, and M. Hill, "Generalized closed-form models for pull-in analysis of micro cantilever beams subjected to partial electrostatic load," *Sensors and Actuators, A: Physical*, vol. 185, pp. 109–116, 2012.

[2] M. A. Hopcroft, W. D. Nix, and T. W. Kenny, "What is the Young's Modulus of Silicon?," *Journal of Microelectromechanical Systems*, vol. 19, pp. 229–238, apr 2010.

[3] O. Bochobza-Degani and Y. Nemirovsky, "Modeling the pull-in parameters of electrostatic actuators with a novel lumped two degrees of freedom pull-in model," *Sensors and Actuators, A: Physical*, vol. 97-98, pp. 569–578, 2002.

[4] A. Yildiz, C. Ak, and H. Canbolat, "New Approach to Pull-In Limit and Position Control of Electrostatic Cantilever Within the Pull-In Limit," 2007.

[5] S. C. Saha, U. Hanke, G. U. Jensen, and T. Sœther, "Modeling of spring constant and pull-down voltage of non uniform RF MEMS cantilever," *BMAS 2006 - Proceedings of the 2006 IEEE International Behavioral Modeling and Simulation Workshop*, no. August 2015, pp. 56–60, 2007.

[6] S. Chowdhury, M. Ahmadi, and W. C. Miller, "A closed-form model for the pull-in voltage of electrostatically actuated cantilever beams," *Journal of Micromechanics and Microengineering*, vol. 15, no. 4, pp. 756–763, 2005.

[7] H. Sadeghian, G. Rezazadeh, and P. Osterberg, "Application of the Generalized Differential Quadrature Method to the Study of Pull-In Phenomena of MEMS Switches," *Journal of Microelectromechanical Systems*, vol. 16, no. 6, pp. 1334–1340, 2007.

[8] S. Pamidighantam, R. Puers, K. Baert, and H. A. C. Tilmans, "Pull-in voltage analysis of electrostatically actuated beam structures with fixed-fixed and fixed-free end conditions," *Journal of Micromechanics and Microengineering*, vol. 12, pp. 458–464, jul 2002.

[9] J. Gere and B. Goodno, *Mechanics of Materials*. CL-Engineering; 7 edition edition (2008), 7th ed., 2008.

[10] I. COMSOL, "No Title."

[11] "Imina technologies."

[12] J. Kokorian, F. Buja, U. Staufer, and W. M. van Spengen, "An optical in-plane displacement measurement technique with sub-nanometer accuracy based on curve-fitting," in *2014 IEEE 27th International Conference on Micro Electro Mechanical Systems (MEMS)*, pp. 580–583, IEEE, jan 2014.

[13] M. A. Crisfield, *Non-linear finite element analysis of solids and structures, Volume 2*. Wiley, 1997.

6

SUPPLEMENTARY MATERIAL: DYNAMIC MODE CHARACTERIZATION OF STIFFNESS CHANGE

In section 4.2 the experimental setup was presented that was used to measure the change in resonance frequency of the cantilever for a varying electrode position. In this chapter the details of this experiment are presented. In section 6.1 the experimental setup is discussed. This is followed by obtained results in section 6.2, which are additional to the ones presented in section 4.3.

6.1. EXPERIMENTAL SETUP

The experimental setup was presented in section 4.2. In this section more details about the setup are shown, as well as on how the measurements were conducted.

6.1.1. PIEZO ACTUATION OF CANTILEVER

In section 4.2 it was mentioned that the cantilever was actuated using a piezoelectric actuator. The cantilever was placed on a stack of a piece of prototype PCB, the piezoelectric actuator and a sheet of 125 µm PDMS from Shielding Solutions. The piezoelectric actuator is manufactured by Piezo Systems Inc. and is cut from a large sheet of 0.005 in thick. It was clamped by a small mechanical spring. This spring is secured to the rest of the stack with tape. The stack is placed on the compliant hinge, that was shown in detail in section 5.5.1.4. This stack is shown in more detail in figure 6.1.

6.1.2. LASER DOPPLER VIBROMETER

The experimental setup is shown in figure 6.2. The system was placed in a Polytec-MSA-400 laser Doppler vibrometer. The system uses the Doppler effect to detect vibrations. The system sends a laser beam through a microscope objective. The beam can be deflected by the scan head, such that multiple measurement points can be taken automatically. The reflection of the laser used to measure the Doppler shift, which is a measure for the velocity of the vibrating sample. The internal signal generator of the system was used to drive the piezoelectric actuator. This signal was also used as a trigger for the system, by connecting the 'sync' port to the 'trigger in' port. This makes sure that a new measurement starts synchronous with a new input signal. A 'burst chirp' signal was used with frequencies from 1 kHz to 500 kHz and a voltage of 10 V. The measurement points were averaged 10 times (Complex averaging), the bandwidth was set from 0 kHz to 500 kHz. The velocity of the vibrometer was set to 25 $\mathrm{mm\,s^{-1}\,V^{-1}}$, such that it can handle the large bandwidth.

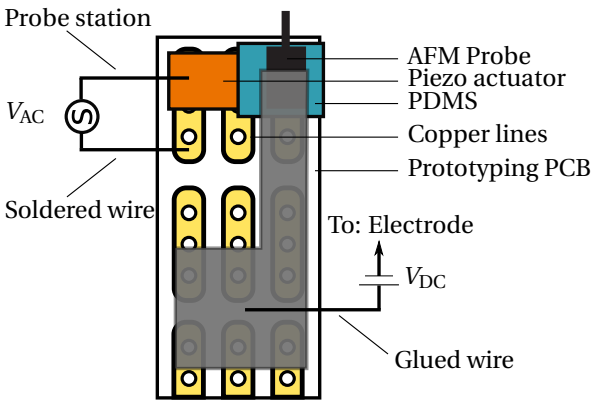

(a) Schematic of stack.

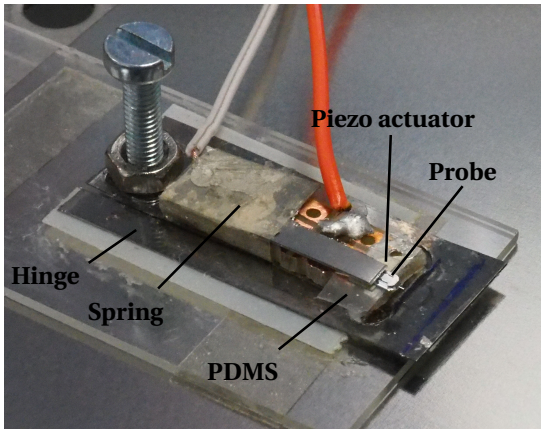

(b) Photo of stack.

Figure 6.1: Stack of a piece of prototyping PCB, with the piezoelectric actuator, PDMS, cantilever and spring. The electrical connections are indicated.

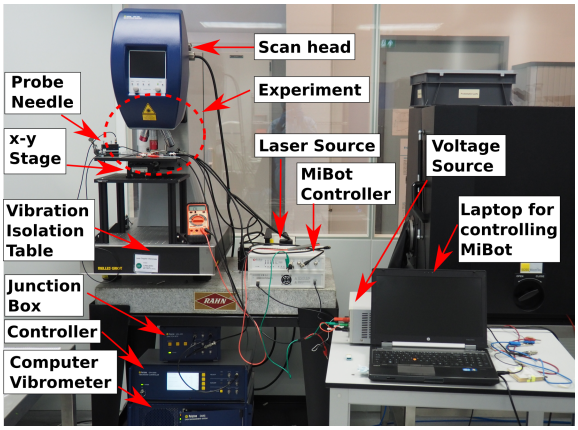

(a) Photo of measurement setup.

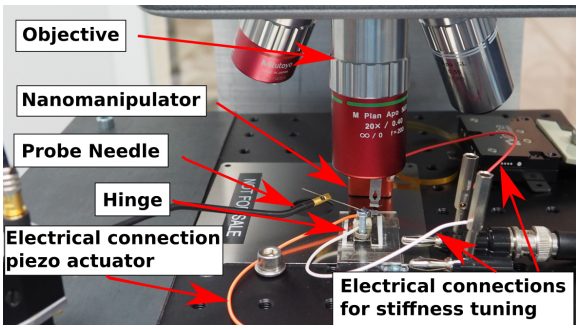

(b) Close up of measurement setup.

Figure 6.2: Experimental setup for vibration measurements.

6.1.3. MEASUREMENT PROCEDURE

The measurement procedure is similar to the one used for the voltage-deflection experiment of section 5.5.1.8. The steps of a measurement:

- Manually position the nanomanipulator close to the probe.
- Make sure that the electrode is higher than the probe
- Use the controller of the nanomanipulator to bring the electrode close to the probe. The electrode should be aligned from the top view
- Go to the side view, by using the $x-y-$stage and focus on the cantilever.
- Bring the electrode close to the cantilever and bring it into focus by moving the nanomanipulator in plane.
- Check if the cantilever is perfectly parallel by comparing the cantilever before and after pull-in. The software tool 'Meazure' was used to mark the position of the cantilever before and after pull-in. (see figure 6.3)
- If needed, use the hinge to adjust the angle of the cantilever relative to the electrode.
- Test the pull-in behavior and estimate the last point of contact between electrode and cantilever. By

varying the applied voltage, a rotation point can be observed, which is the last point of contact. The effective length is determined according to this point. This point is assumed to be found within ±10 px.

- Bring the electrode close to the cantilever (~ 5µm). Choose the right position along the length of the cantilever and measure the effective length. Apply a voltage for pull-in.
- Return to top view by using the stage, focus and choose the measurement points. (see figure 6.4). Run the measurement.
- Go back to side view, and repeat the final three steps until all measurement points are completed.

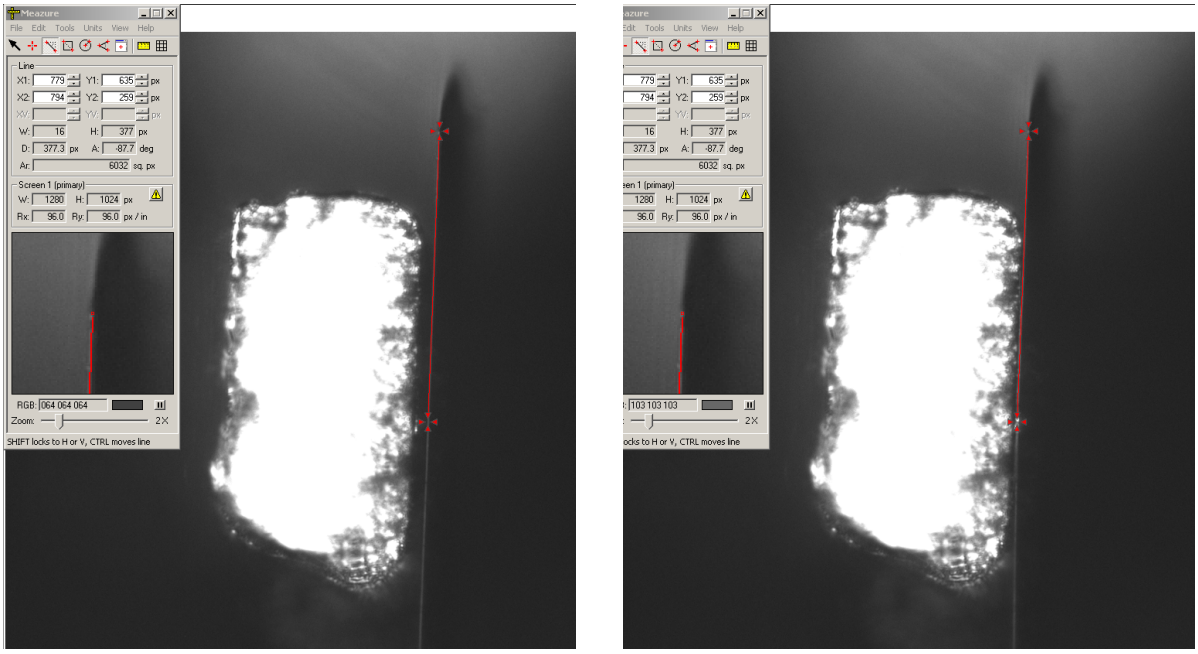

(a) Cantilever in untuned state. The tool 'Meazure' is used to indicate the position of the cantilever.

(b) The cantilever is in tuned state. The stage of the vibrometer is used to bring the cantilever to the red line that was drawn with the tool 'Meazure', and it is verified that the cantilever and electrode are parallel.

Figure 6.3: Verification that electrode and cantilever are parallel.

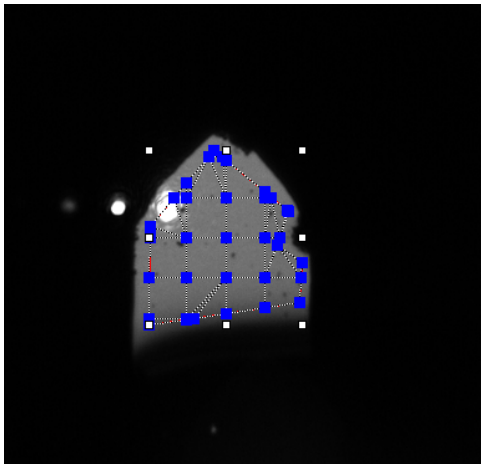

Figure 6.4: Measurement point on cantilever in tuned state. Only a part of the effective length is visible, due to the shape of the electrode and the shade on the cantilever.

6.2. RESULTS

In this section, additional results are presented. First, the higher order resonance frequencies and modes of a cantilever without adjustments are shown in section 6.2.1. In section 4.3 the results of a single measurement were presented. A second data set with similar results is shown in section 6.2.2.

6.2.1. HIGHER ORDER MODES

A measurement was performed to find the higher order modes of the cantilever. This was done without the electrode in close proximity. The bandwidth of the measurement is 500 kHz.

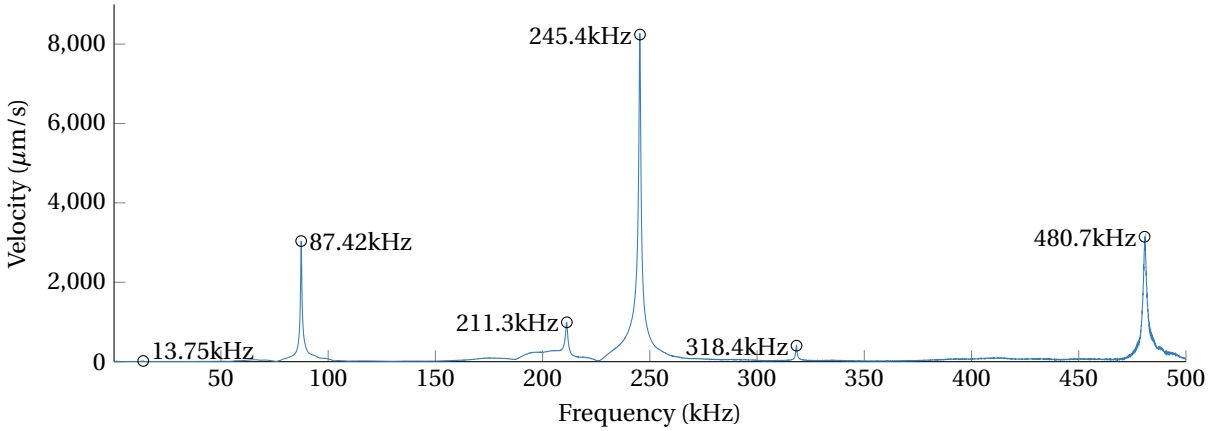

Figure 6.5: Resonance frequencies of the cantilever for a bandwidth of 500 kHz.

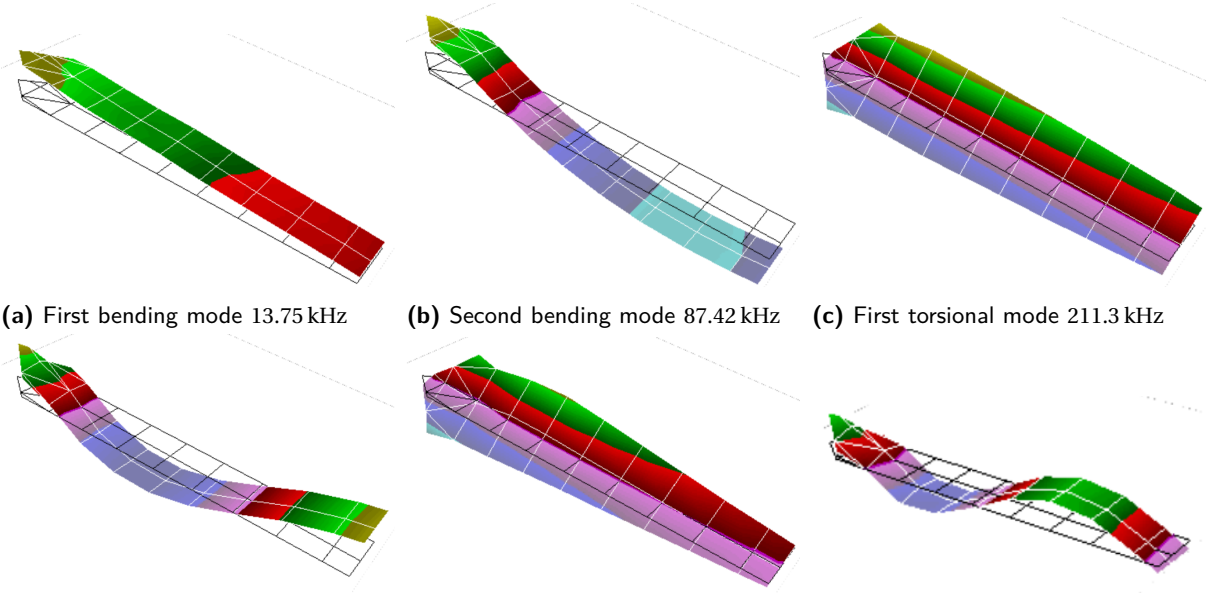

(a) First bending mode 13.75 kHz **(b)** Second bending mode 87.42 kHz **(c)** First torsional mode 211.3 kHz

(d) Third bending mode 245.4 kHz **(e)** Second torsional mode 318.4 kHz **(f)** Fourth bending mode 480.7 kHz

Figure 6.6: Mode shapes of the cantilever, that corresponds with the modes from figure 6.5

6.2.2. ADDITIONAL DATA SET

In section 4.3 the results of the measurements were presented. The measurement was repeated, which is shown in figures 6.7 and 6.8.

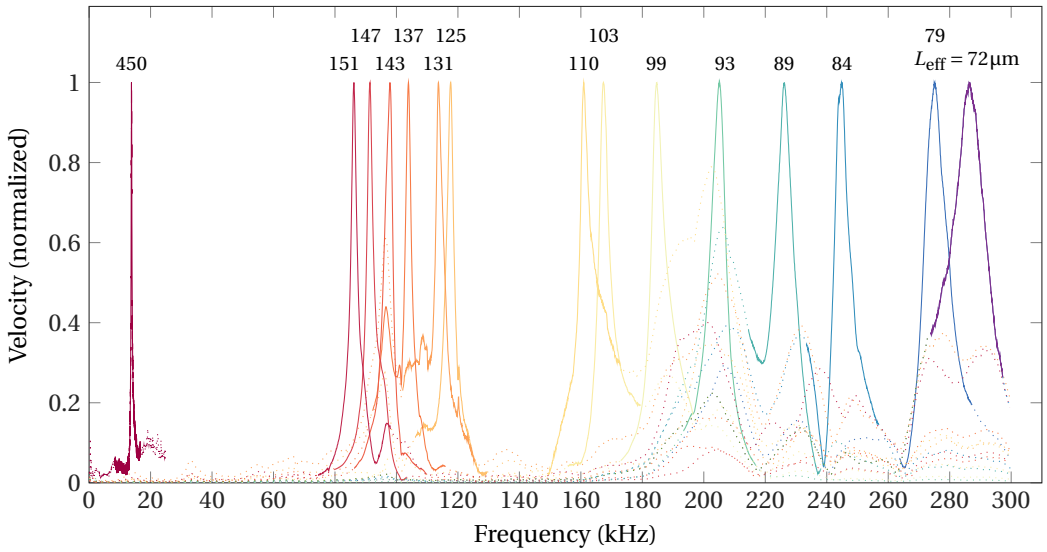

Figure 6.7: The fundamental resonance frequency obtained for different adjusted lengths of the cantilever. The electrode position is varied and the cantilever is pulled-in for these positions, reducing its effective length. The cantilever is actuated with a frequency sweep and the response is shown in this figure. The numbers above the peaks indicate the effective length of the cantilever (in µm). Only the resonance peaks of the cantilever are shown in a solid line, while the rest of the bandwidth is plotted as a dotted line for clarity. All the measurements were made at an applied voltage of 60 V. This data set is additional to the one shown in the main article.

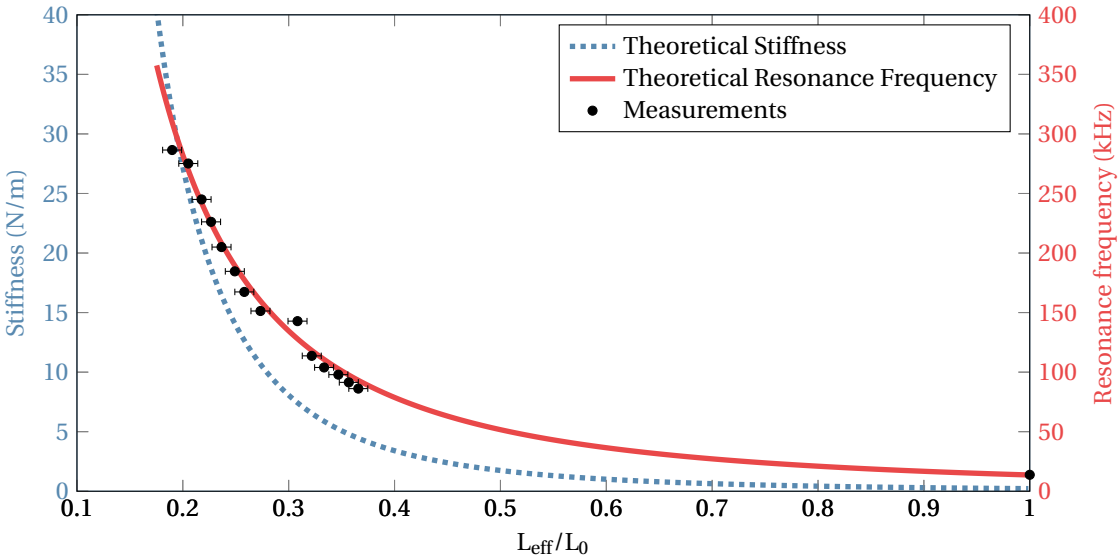

Figure 6.8: Theoretical stiffness and resonance frequency compared with the measurements as a function of the normalized effective length. The measurement points correspond with the peaks found in **??**. The error bars correspond to the measurement uncertainty on the effective length.

6.3. DISCUSSION AND CONCLUSION

The results are very similar to the results of section 4.3. There is one data point in figure 6.8 at $L_{\text{eff}}/L_0 \sim 0.3$, which deviates from the expected trend. It is uncertain what has caused this. The behavior of the resonating cantilever at other frequencies than the resonance frequency was not discussed in section 4.4. Between 80 – 120 kHz and 180300 kHz the spectrum is not flat outside of the resonance peaks. It was assumed that this is caused by vibrations in the rest of the system. This was confirmed by performing a frequency response measurement on top of the electrode, which is shown in figure 6.9. The non-normalized frequency responses are shown for both the cantilever with varying effective length, and the top of the electrode. There are two regions where the frequency response of the electrode is significant (around 100 kHz and 200 kHz). There are two observations: The resonance peaks of the cantilever become higher when they are closer to these regions. And when there is no resonance peak of the cantilever near these spots of the electrode, the cantilever gives a response. For the region around 100 kHz it is a very small effect, but around 200 kHz it is significant. Considered that these spots are all at the same frequency, and that these correspond with the frequency response of the electrode it can be concluded that this effect is caused by vibrations of the electrode.

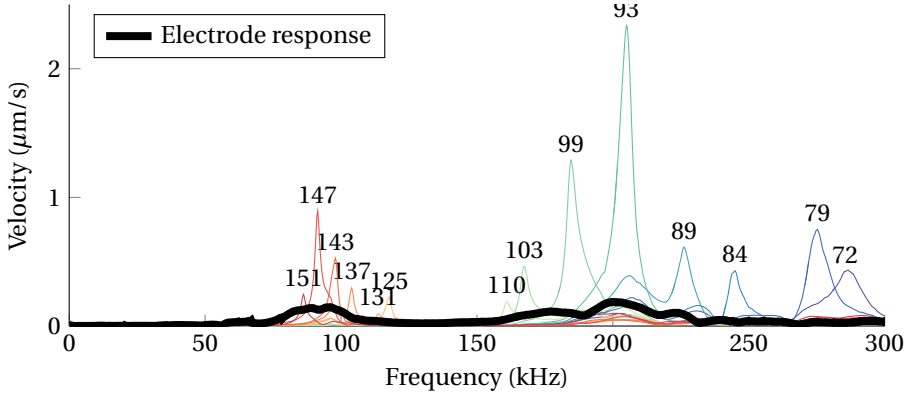

(a) Frequency response of the cantilever for a varying effective length (the numbers near the peak indicate the effective length in μm).

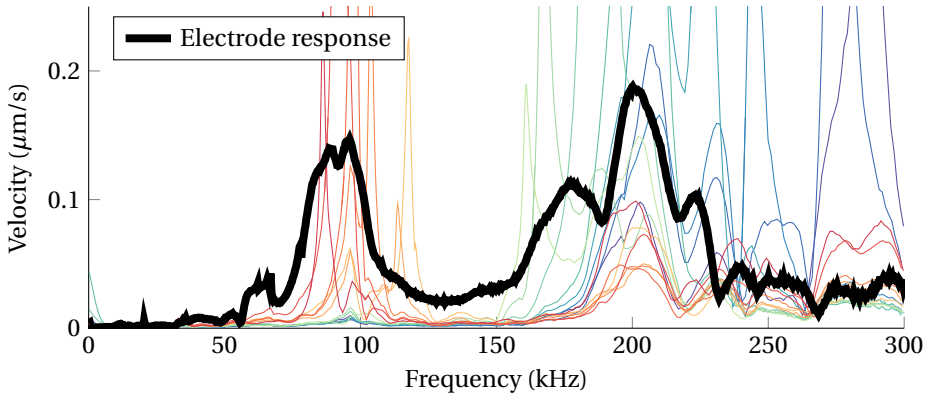

(b) Frequency response, with zoomed in y-axis.

Figure 6.9: Frequency response of the cantilever and electrode

6.3.1. SQUEEZE FILM DAMPING

During the measurement it was observed that when the the cantilever was in unadjusted state, but the electrode was close to the cantilever ($\sim 5-10\,\mu$m), the first resonance mode was heavily damped, while the second mode was apparently unaffected. Squeeze film damping could be the cause of the observed effect. In order to determine if this could be the case, a brief analysis has been performed.

Squeeze film damping is a phenomenon which is often observed in MEMS. When two structures are moving

very close to each other, the air film in between is resulting in a lateral flow as shown in figure 6.10. For slow speeds, the air can escape between the plates, but the viscous forces of the air give a damping effect. For high speeds, the air cannot escape from the gap. The air is compressed and acts like a spring. This results in a stiffening effect of the system.

Pandey *et al.* [1] presented an analytical model that describes the influence of both the resonance frequency and the mode shape of an oscillating micro cantilever on the squeeze film effect. This model was compared with finite element results and experiments. The model predicts the damping ratio ξ within 10% compared to measurements (a low damping ratio results in a high qualtiy factor Q). It was concluded that the damping ratio decreases for an increasing frequency, and that also the mode shape has a significant influence on this damping ratio. In a comparable configuration ($L \times w \times t = 350 \times 22 \times 4\,\mu\text{m}$ and $g_0 = 1.4\,\mu\text{m}$) the damping ratio for the second and third out of plane mode were reduced by 84% and 94% respectively. The model assumes that inertia effects of the squeeze film may be neglected, which is valid when the Reynolds number is smaller than unity. To see if this assumption is also valid for the present system the Reynolds number Re is calculated as:

$$Re = \frac{\rho_a {g_0}^2 \omega}{\mu_{\text{eff}}} \tag{6.1}$$

Where ρ_a the density of air ($1.2\,\text{kg m}^{-3}$), ω the angular resonance frequency and the effective dynamic viscosity μ_{eff}, which is a function of the dynamic viscosity μ and the Knudsen number $Kn = \lambda / g_0$ ($\lambda = 65\,\text{nm}$ the mean free path of air):

$$\mu_{\text{eff}} = \frac{\mu}{1 + 9.683 Kn^{1.159}} \qquad 0.01 < Kn < 0.1 \tag{6.2}$$

The maximum Reynols number is 0.1, for $g_0 = 10\,\mu\text{m}$ and resonance frequency of the second mode $f = 87\,\text{kHz}$. It is concluded that the model which was developed by Pandey *et al.* is valid for the present work, because the assumptions are still valid. So similar results may be expected. The fact that the first order mode is not visible when the electrode is close to the cantilever, while the second order mode seems unaffected can be explained by the squeeze film effect. A more detailed study should be performed before definite conclusions can be drawn.

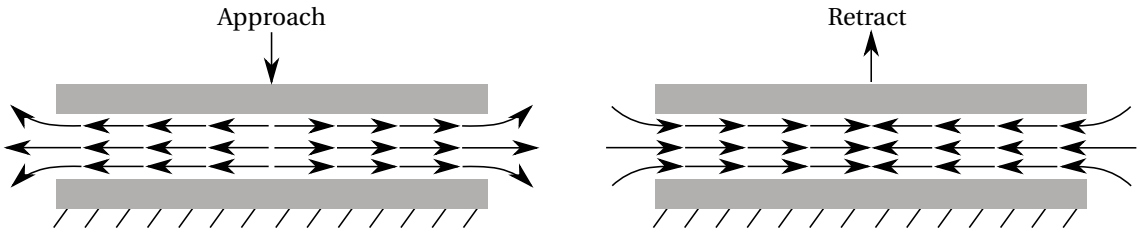

(a) Top plate is approaching. The air is squeezed out. **(b)** Top plate is retracting. The air is sucked in.

Figure 6.10: Schematic of squeeze film effect.

REFERENCES

[1] A. K. Pandey and R. Pratap, "Effect of flexural modes on squeeze film damping in MEMS cantilever resonators," *Journal of Micromechanics and Microengineering*, vol. 17, pp. 2475–2484, dec 2007.

7

CONCLUSIONS AND RECOMMENDATIONS

The goal of the thesis was to *in situ* adjust the stiffness of an AFM cantilever with at least one order of magnitude, while remaining compatible with conventional AFM systems.

- A literature study was performed to identify different methods to achieve stiffness tuning in MEMS. It was written in a journal-style format which is under review. It enables designers with an overview on existing methods to achieve stiffness adjustment in MEMS. It was concluded that electrostatic tuning is the most applied method, but in order to achieve a wide tuning range large and complex devices are required. Mechanical tuning provides a compact solution if a large range is required, but these methods are often discrete.
- Three concepts were considered, which were based on adding mechanical springs, change in effective length and change in second moment of inertia. The best concept was using the change in effective length, which was achieved by electrostatic clamping of a cantilever. An electrode which is covered by an insulative layer is placed close to a regular AFM cantilever. By applying a large voltage, the cantilever is pulled-in.
- A study was performed on the voltage-deflection behavior on the cantilever under an electrostatic load, to find the pull-in voltage. This was done by comparing a COMSOL model, analytical model and measurements. These measurements were performed with off the shelf components on a proof-of-concept setup. It consisted of a commercially available probe, a robotic nanomanipulator and an electrode which was made from spring steel, using a laser cutter. The models agreed quite well with the measurements. Both the COMSOL model and the analytical model overestimated the required pull-in voltage. The pull-in deflection of the analytical model was on average 17% higher than the measurement and the pull-in voltage is 11% higher. An important factor is that the measurements were performed in discrete steps of 1 V. So the pull-in voltage is inherently underestimated. It was concluded that the cantilever goes to a clamped-pinned configuration after pull-in and that a higher voltage is required to go to the required adjusted state. This behavior is simulated with a time-dependent COMSOL model.
- The change in stiffness was demonstrated in a proof-of-concept experiment, by measuring the change in resonance frequency with a laser Doppler vibrometer. This was done for a varying electrode position. These measurements were in good agreement with the theoretical behavior. The unadjusted stiffness of $0.2\,\mathrm{N\,m^{-1}}$ was changed to $27\,\mathrm{N\,m^{-1}}$, which is a change of over two orders of magnitude. This change in stiffness meets the requirements that were set in the introduction of this thesis. This was not achieved before in literature. Figure 7.1 shows the summarizing figure from the literature review, but with the present work included. The present work has a significantly larger range than previously published devices.

The design is not yet capable of performing actual AFM measurements, but the working principle of the design was demonstrated with the experiments. The required change in stiffness was achieved. There are still some steps to be taken, before AFM measurements can be performed. Because the concept uses conventional AFM cantilevers, a working prototype is likely to be compatible with the widely used laser deflection sensor.

An outlook on those steps to be taken to obtain a working prototype are shown in the recommendations.

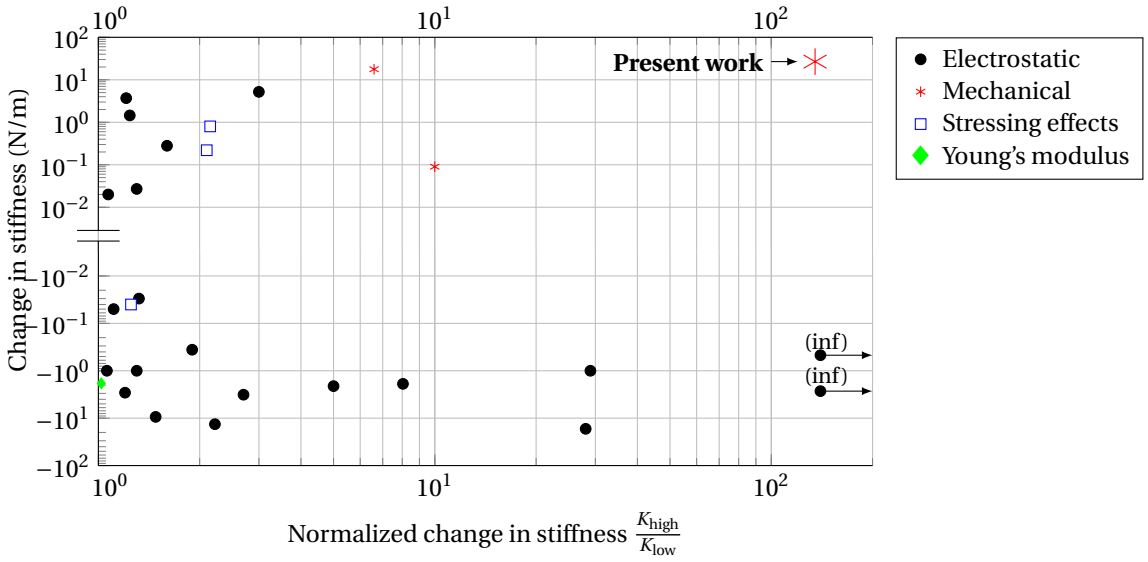

Figure 7.1: Change in stiffness versus normalized change in stiffness with present work included.

7.1. RECOMMENDATIONS

The ultimate goal of the project is to micro fabricate a working prototype, which can be used in actual AFM measurements. In order to achieve this goal a couple of recommendations are made:

- The analytical model, which was developed in section 5.2 is only valid up to the pull-in voltage. This model should be extended or a second model should be adapted which can describe post pull-in behavior. Having an analytical model that can describe the full behavior helps to choose the optimal design parameters for the system.
- A practical design should be made, such that actual AFM measurements can be performed. The electrode should be integrated with the cantilever in a single device. The ultimate goal is to have a probe that can cover the entire range of stiffness that is used in AFM ($0.01\,\mathrm{N\,m^{-1}} - 40\,\mathrm{N\,m^{-1}}$), and that every value of stiffness can be obtained. This requires a movable electrode, with a large stroke. This is a challenging task. An intermediate step could be to make a stiffness adjustment for only two values, which is considerably easier.
- Before fabrication, the chosen materials should be tested. The dielectric strength should be verified, such that the design can be adapted to the findings. Stiction might be a problem for the device. Measurements on the stiction force should be done for the materials of choice for the design. If the stiction force is higher than the mechanical restoring force of the cantilever, it is necessary to take precautions to limit stiction. This can for instance be done by using low surface energy materials, decreasing contact area by surface roughening or applying dimples, or chemically modifying the surface with an anti-stiction coating.

A

THEORY OF ATOMIC FORCE MICROSCOPY

In this chapter important aspects of AFM will be further explained. The most important parts of the equipment of AFM are shown in appendix A.1. The key interaction forces that play a role in AFM are explained in appendix A.2. The information about the deflection of the cantilever can be used for several modes: the force-distance curve, the basic imaging modes (topographic modes) and a selection of non-topographic, which will be discussed in appendix A.3.

A.1. EQUIPMENT

The AFM is able to control the position of a chip with a micro cantilever beam relative to the sample. This entire chip is called the probe. This part is the topic of this thesis and will be further elaborated in appendix A.1.1. A sensor system is used to determine the deflection of the cantilever. In most of the AFM systems a laser deflection sensor is used. The working principle will be explained in appendix A.1.2. In order to control the position of the probe probe a stage and a control loop is needed which will be the topic of appendix A.1.3.

A.1.1. THE AFM PROBE

The AFM probe consists of a (support) chip, cantilever and tip. This nomenclature can be seen in A.1. Besides the 'standard' rectangular cantilever, triangular and V-shaped probes are being used in industry. This thesis will only focus on the rectangular ones. Chips from different manufacturers are more or less the same; they all have the same support chip size (1.6 mm x 3.4 mm). Also the angle of the edges at the support chip is constant, because the KOH etch used for this process step guarantees an angle of 54.7°. Only the thickness may vary for different probes and manufacturers; values of 300 µm, 315 µm and 500 µm are commonly used.

The most common used material is mono-crystalline silicon, while silicon nitride is sometimes preferable. Silicon wears down faster, and tends to be more reactive than silicon nitride. Probes can either be made entirely out of silicon nitride, or the tip of a mono-crystalline silicon probe can be coated with silicon nitride. Other common coatings are diamond (for a harder tip) or gold (for chemical inertness) [1]. Coatings are not only used at the tip side; backside coatings are also often applied. This are usually metals like aluminum, gold, platinum or chromium to increase reflectivity for the laser deflection sensor (see appendix A.1.2).

The dimensions of commercially available cantilevers come in a wide variety. These dimensions play an important role in the mechanical behavior of the cantilever. The stiffness and resonance frequency depend on these parameters. In table A.1 the range of dimensions and properties are summarized.

Amongst a large variety in cantilevers, there are also a lot of different types of probe tips. The shape of the tip has a large influence on the quality of the images. In general one can say, that the sharper an AFM tip, the more detailed the image can be; a sharper tip can follow the surface better than a blunt tip. This is illustrated in figure A.2.

Table A.1: Typical dimensions and properties of commercially available AFM cantilevers.

Length (μm)	Width (μm)	Thickness (μm)	Stiffness ($N\,m^{-1}$)	Resonance frequency (kHz)
100-500	20-50	1-3	0.01-100	13-500

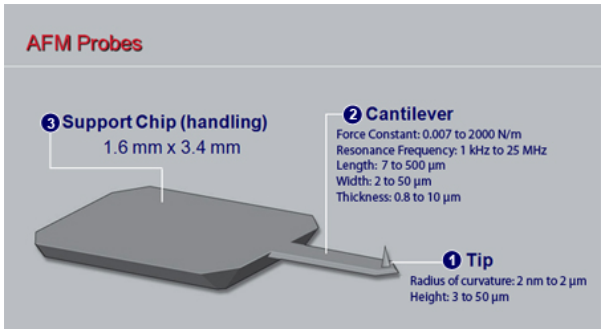

Figure A.1: Nomenclature in AFM probes. `http://www.nanoandmore.com/afm-probes-guide.php`

A.1.2. LASER DEFLECTION SENSOR

There are several ways of measuring the deflection of the cantilever, but the most common one is the laser deflection sensor. This comprises a laser, that is focused on the backside of the cantilever, near the tip. The reflection of this laser beam is measured by a photo sensitive sensor. Figure A.3a shows the working principle of the laser deflection sensor. Both the vertical movement ΔZ, as the rotation at the end α add up to the displacement of the laser spot ΔS at the sensor. The sensor is a photo sensitive display, consisting out of four quadrants, as can be seen in figure A.5b. When the cantilever deflects, the laser spot will move up and down on the sensor. By measuring the intensity difference between the upper (1 and 2) and lower (3 and 4) halves, the deflection can be determined. The torsional motion of the cantilever can be used by using the difference between the left- (1 and 3) and the right side (2 and 4) of the PSD. This application will be explained in appendix A.3.4.

A.1.3. STAGE

The AFM can control the position of the probe, relative to the sample, in x-, y- and z-direction. For each direction of motion there is a coarse and a fine actuator. The coarse actuator is usually a stepper motor, and is used for the large actuation strokes, that do not require a high precision, like finding the right scanning area or approaching the sample. The fine actuation is usually done with piezoelectric transducers. These actuators have a relatively small stroke, but are precise and accurate. There are different scan-configurations possible; either the stage or probe can be kept stationary, while the other moves. It is also possible that the x-y- and z-motion are divided over the probe and stage; for instance that the stage does the x-y scanning, while the probe moves in z-motion. The x- and y piezo-actuators are used to scan the sample, as shown in figure A.3b. The z-actuator can be used to adjust the tip-sample distance.

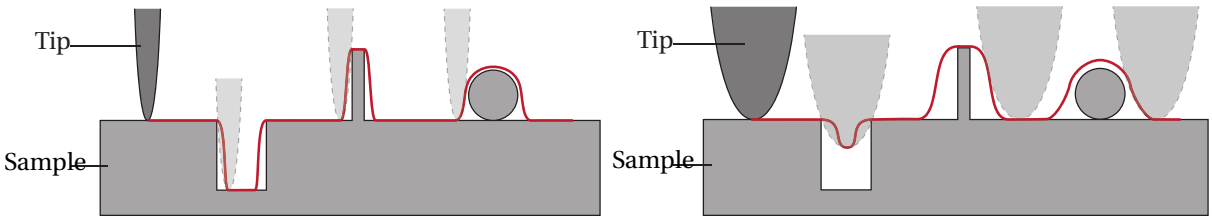

(a) Imaging with a sharp tip.

(b) Imaging with a blunt tip.

Figure A.2: The sharpness of the tip determines the quality of the image. For a sharper tip, a more detailed image can be made. The red line, is the shape that the AFM 'sees'. Image a) has a sharper tip than image b). The influence of the tip shape on the image is called tip convolution

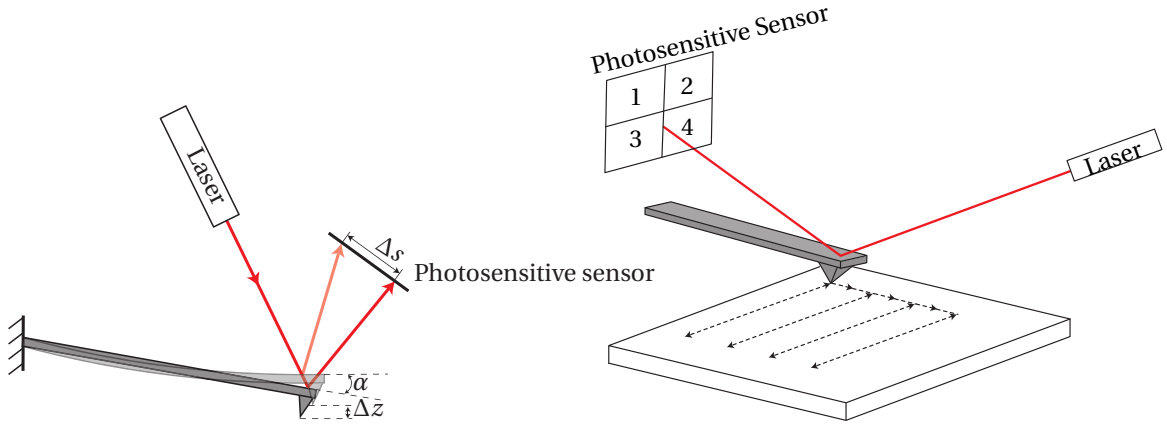

(a) The deflection of the cantilever is determined by measuring the change in position (ΔS) of the laser on the photosensitive sensor. The change in the position of the laser is caused by the motion in the out-of-plane direction ΔZ of the cantilever, and the tilting of the tip α due to deflection.

(b) The sample is scanned line for line by the AFM probe. Along each line, multiple measurement points are taken to reconstruct the surface topography. The laser deflection sensor is used to measure the deflection of the cantilever.

Figure A.3: The working principles of Atomic Force Microscopy: scanning and sensing

A.2. TIP-SAMPLE INTERACTION

When approaching the sample with the probe, several forces will play a role. It depends on the distance between tip and sample which forces are dominant. The sum of the attracting and repulsive forces determine the total force, and deflection of the cantilever. In this section the most important forces that play a role will be discussed. The most important forces are the long range attracting Van der Waals forces, short range ionic repulsion forces and capillary force. There are other forces present in the tip-sample interaction such as electrostatic-, magnetic-, ionic repulsion-, Casimir-, chemical bonding-forces etc. These forces will not be further explained, since they are not essential to understand the working principles of AFM.

A.2.1. VAN DER WAALS FORCES

One of the most important forces in atomic force microscopy are the Van der Waals forces; it are inter-atomic attractive forces that become very important when two objects are very close. But for AFM, these forces are considered long-range in comparison with the other dominant forces. There are three types of Van der Waals forces: (1) Keesom-, (2) Debye- and (3) London force. Keesom force is the result of the dipole-dipole interaction between atoms or molecules, Debye forces are caused by dipole-induced dipole interaction and London forces is the induced dipole-induced dipole interaction. Typically, Van der Waals forces are in the range of 1-10 nN in tip-sample interaction. These forces depend on different material dependent parameters, but have the same relation with respect to the separation distance r: $F \sim -\frac{1}{r^6}$ [2].

A.2.2. IONIC REPULSION FORCES

When the tip comes extremely close to the sample, ionic repulsion forces start to become dominant. These ionic forces consist of Pauli repulsion and coulombic repulsion between the nuclei. The Pauli repulsion is a consequence of the Pauli exclusion principle, that says that electrons cannot occupy states with the same quantum number. So when the electron clouds of the atoms of the tip and sample start to interact, there will be a repulsive force. These repulsive, short distance, forces can be approximated with a $F \sim \frac{1}{r^{12}}$ relation.

A.2.3. CAPILLARY FORCES

In ambient environment almost all samples have a small liquid layer, usually water. This forms a meniscus that pulls the tip towards the sample when the tip is in contact with the liquid. This capillary force is large

compared to the Van der Waals forces. When the tip approaches the sample and comes into contact with the liquid layer, the tip will be pulled-in due to this force. The opposite occurs when the tip is retracted from the sample; the liquid meniscus will keep pulling on the tip, causing the cantilever to deflect downwards. As soon as the retracting force is bigger than the pulling force of the liquid the capillary meniscus will break and the tip will snap out.

In some applications the capillary force needs to be eliminated. This can either be done by operating the AFM in a vacuum or in a chamber with dry nitrogen; then there will be no condensation on the sample. An other solution could be to operate the entire system in liquid; this eliminates the capillary.

A.3. AFM MODES

The AFM is mostly known for its topographical modes; in these modes the topography of the surface is mapped. These modes will be discussed in appendix A.3.2 for the static mode and appendix A.3.3 for dynamic mode imaging. The AFM can also be used to measure material properties. These non-topographical modes will be discussed in appendix A.3.4. In figure 1.2 the stiffness range of the cantilevers for the imaging modes was summarized. In appendix A.3.1 the 'force-distance' curve is explained to look at the fundamental mechanisms in these measurements.

A.3.1. THE FORCE-DISTANCE CURVE

Making a force-distance curve is one of the basic operations of an AFM. In this type of measurement the force between tip and sample is measured. It is not possible to measure the force in a direct way though, but it is derived by using Hooke's law: $F = -k_c \cdot u_{\text{tip}}$. The cantilever stiffness k_c is multiplied with the deflection of the tip u_{tip}, that can be measured by deflection sensor. The most simple form of the force-distance curve is shown figure A.4a. This only considers the Van der Waals, and ionic repulsion forces, as explained in appendix A.2. At a long distance from the sample, there is no force acting between tip and sample. When the tip approaches the sample, the long range Van der Waals forces start to attract the tip. This is represented as a negative force in the force-distance curve. The magnitude of this force is progressively increasing for a decreasing tip-sample distance. At a certain point repelling ionic forces will start to play a significant role and add a positive force to the tip. These forces increase progressively for a decreasing tip-sample distance, but the rate is faster than for the Van der Waals forces. At a certain point the repelling force will become dominant and the force will go asymptotically to infinity.

In practical applications, the curve is usually different than in the ideal case as shown in figure A.4b. For example, 'jump to contact' is a common phenomenon in the force-distance cure. This happens when the attractive forces on the tip suddenly become much higher than the mechanical restoring force. This can for instance happen when the tip comes in contact with a liquid layer on the sample, and a capillary bridge is formed. Snap-out effect can be witnessed in the retracting motion. The tip can adhere to the sample due to, for instance, chemical binding or capillary forces. When the retracting force is larger than the adhesion forces, a snap-out effect is seen in the force-distance curve.

A.3.2. CONTACT MODE

One of the main modes in AFM imaging is the contact mode. The tip of the probe is in direct contact with the sample. It works in the region where the repelling forces are dominant (figure A.4a). The probe is dragged along the surface, and any topographical features on the sample will result in a deflection of the cantilever that will be measured with the sensor. There are two subclasses of contact mode imaging: constant force and constant height mode.

A.3.2.1. CONSTANT FORCE

When an AFM scans in the constant force mode, a feedback loop tries to keep the force between the tip and sample constant. Since the force cannot be measured in direct way, the deflection of the cantilever is sensed; this is a measure for the force between tip and sample. When the system detects a small deflection of the cantilever, the feedback loop is used to adjust the position in the z-direction. The displacement of the z-actuator

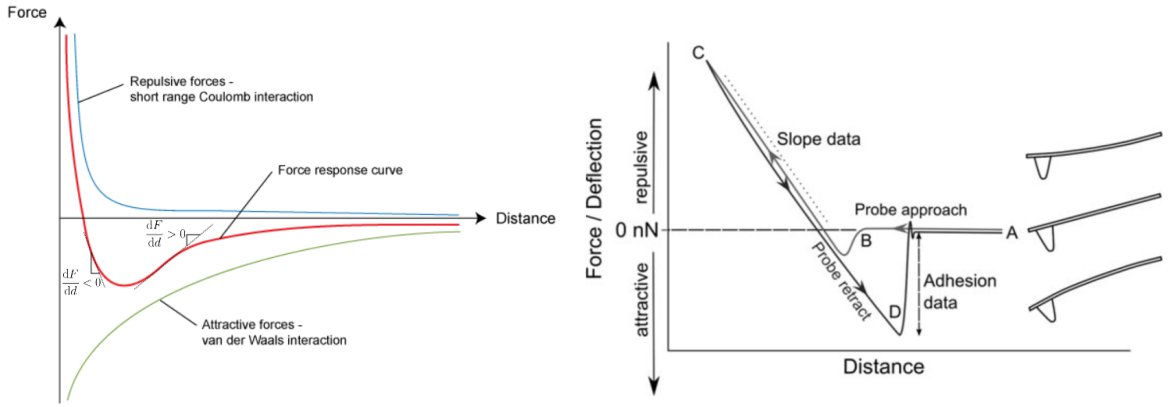

(a) The attractive Van der Waals forces and repulsive coulombic (often called ionic repulsion, see appendix A.2) forces add up to the typical, theoretical, shape of a force distance curve. The practical force-distance curve usually looks different than this theoretical approximation though, because other forces often play a significant role. [3]

(b) A model force-distance curve. At point A, the probe is far from the surface, at B 'snap-in' occurs as attractive forces pull the probe onto the surface. The force becomes repulsive as the probe continues to drive towards the sample. At some user-defined point C, the direction of travel reverses. At point D 'Pull-of' occurs as the force applied to the cantilever overcomes tip-sample adhesion.[4].

Figure A.4: Two models for force-distance curves compared. Figure (a) only considers the Van der Waals forces and ionic repulsion forces, while Figure (b) also considers the adhesion between tip and sample on the retracting motion. Figure (a) is useful to understand the approaching motion of the tip, while Figure (b) gives an insight in the rest of the stroke

is then used to reconstruct the sample. The advantage of this method is that the forces on the cantilever and sample stay at a constant. It will not cause the cantilever to break, the wear-rate of the tip remains low and the sample is less damaged. Constant force imaging can also be used for friction measurements. Friction forces are calculated by multiplying the friction coefficient (material property) with the normal force: $F_{\text{frict}} = \mu F_{\text{norm}}$. Since the normal force is a set constant, the friction coefficient can be determined if the frictional force is known. The frictional force can be calculated with the torsional stiffness and torsion of the cantilever, which is shown in figure A.5a.

A.3.2.2. CONSTANT HEIGHT

Constant height mode is similar to the constant force mode. But as the name suggests, the height of the AFM probe relative to the sample is constant during scanning. No feedback loop on the z-position is needed, which results in a faster scan. This method implies that the force on the tip depends on the topography of the sample. When there are features that are very high, this might damage the cantilever. When there are features that are deep in the sample, the tip might loose contact.

A.3.3. DYNAMIC MODE

The second main mode in AFM is the dynamic mode. The cantilever is actuated close to, or at its resonance frequency and is placed close to the sample. There are two sub-modes that belong to the dynamic mode: Frequency Modulation (FM-AFM) and Amplitude modulation (AM-AFM)[5].

A.3.3.1. FREQUENCY MODULATION

In the FM-AFM mode, the tip is at a distance from the sample such that it will not touch. The oscillation amplitude is in the order of 10 nm and the long-distance, attracting surface forces interact with the tip. The cantilever is actuated close to its resonance frequency, with a constant amplitude. Forces acting on the tip cause a slight change in resonance frequency, because the effective stiffness at the tip location changes. This change in frequency is used as the input of a feedback loop, which tries to keep the resonance frequency constant by adjusting the tip-sample height [6].

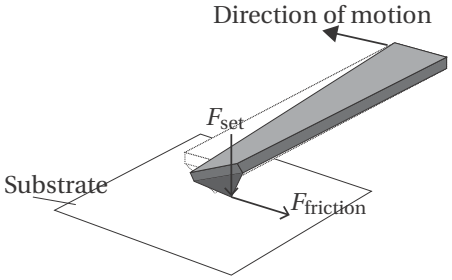

(a) The torsional motion of a cantilever arises when the cantilever is dragged along the substrate and a certain force is applied to the tip (F_{set}). This results in a friction force $F_{friction}$ that results in the torsion of the cantilever. This torsion can be measured by not taking the vertical component of the photo sensitive sensor, but by measuring the horizontal one.

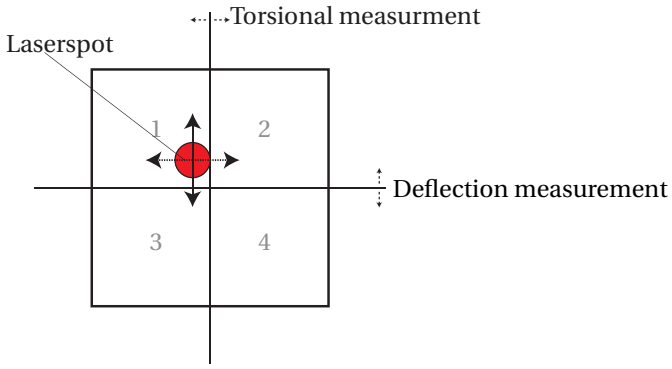

(b) The photosensitive sensor is divided into four quadrants (1, 2, 3 and 4). The intensity difference between (1+2) and (3+4) is used to measure the deflection of the cantilever. The intensity difference between (1+3) and (2+4) for the torsional motion of the cantilever.

Figure A.5: Working principle of laser deflection sensor for frictions measurements

A.3.3.2. AMPLITUDE MODULATION

In amplitude modulation, the cantilever is actuated near, or at its resonance frequency. The amplitude of the oscillating cantilever is used as the input for the feedback loop. The oscillation amplitude is influenced by the tip-sample interaction. The feedback loop tries to keep this oscillation amplitude constant by adjusting the height of the cantilever relative to the sample. It can operate in low amplitude mode (<1 nm) [7] and high amplitude mode (~100 nm) [8]. In the first mode, the tip will not have mechanical contact with the sample, while in the second mode it will. This is also known as 'Tapping mode' or 'Intermittent mode'. The tip will briefly touch the sample each oscillation cycle. This tapping mode is the most frequently used method of the AM-AFM modes. [1]

A.3.4. NON-TOPOGRAPHIC MODES

The atomic force microscope has other applications than imaging. Some material properties can be derived by using the AFM, these are called the non-topographic modes. Examples of such modes:

- Force spectroscopy: using the force-distance curve to measure the force between tip and sample. For instance: by functionalization of the tip, molecular binding force can be measured [9].
- Nano-indentation: by indenting an AFM tip into the substrate, the hardness and Young's modulus of the sample can be derived. The indentation of the tip in the sample can be derived by comparing the deflection of the cantilever with the z-motion of the stage. Several models were developed that match the indentation with the Young's modulus and hardness [10].
- Nano-lithography: The AFM can be used for nano-patterning [11, 12].

[1] In literature, AM-AFM is sometimes said to be equal to 'Tapping mode', while this is not necessarily the case

REFERENCES

[1] M. Tortonese, "Cantilevers and tips for atomic force microscopy," *IEEE Engineering in Medicine and Biology Magazine*, vol. 16, no. 2, pp. 28–33, 1997.

[2] E. Meyer, "Atomic force microscopy," sep 1992.

[3] University of Cambridge, "Tip Surface Interaction."

[4] P. Eaton and P. West, *Atomic Force Microscopy*. Oxford: Oxford University Press, 2010.

[5] R. García, "Dynamic atomic force microscopy methods," *Surface Science Reports*, vol. 47, pp. 197–301, sep 2002.

[6] T. R. Albrecht, P. Grütter, D. Horne, and D. Rugar, "Frequency modulation detection using high-Q cantilevers for enhanced force microscope sensitivity," *Journal of Applied Physics*, vol. 69, pp. 668–673, jan 1991.

[7] Y. Martin, C. C. Williams, and H. K. Wickramasinghe, "Atomic force microscope-force mapping and profiling on a sub 100-Å scale," *Journal of Applied Physics*, vol. 61, pp. 4723–4729, may 1987.

[8] Q. Zhong, D. Inniss, K. Kjoller, and V. Elings, "Fractured polymer/silica fiber surface studied by tapping mode atomic force microscopy," jun 1993.

[9] H.-J. J. Butt, B. Cappella, and M. Kappl, "Force measurements with the atomic force microscope: Technique, interpretation and applications," *Surface Science Reports*, vol. 59, pp. 1–152, oct 2005.

[10] W. C. Oliver, "Measurement of hardness and elastic modulus by instrumented indentation : Advances in understanding and refinements to methodology," *Journal of Materials Research*, vol. 19, no. 1, pp. 3–20, 2004.

[11] X. Xie, H. Chung, C. Sow, and A. Wee, "Nanoscale materials patterning and engineering by atomic force microscopy nanolithography," *Materials Science and Engineering: R: Reports*, vol. 54, pp. 1–48, nov 2006.

[12] R. Garcia, A. W. Knoll, and E. Riedo, "Advanced scanning probe lithography.," *Nature nanotechnology*, vol. 9, pp. 577–87, aug 2014.

B

SEM MICRO GRAPHS CANTILEVER

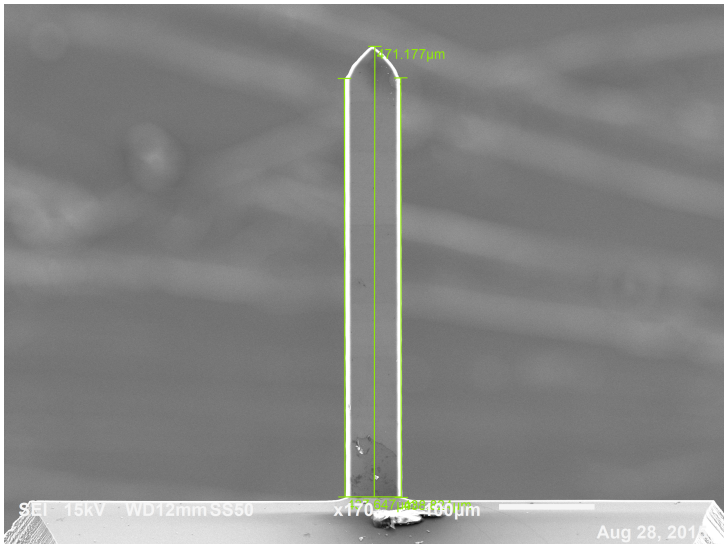

(a) Top of the cantilever to determine the lengths.

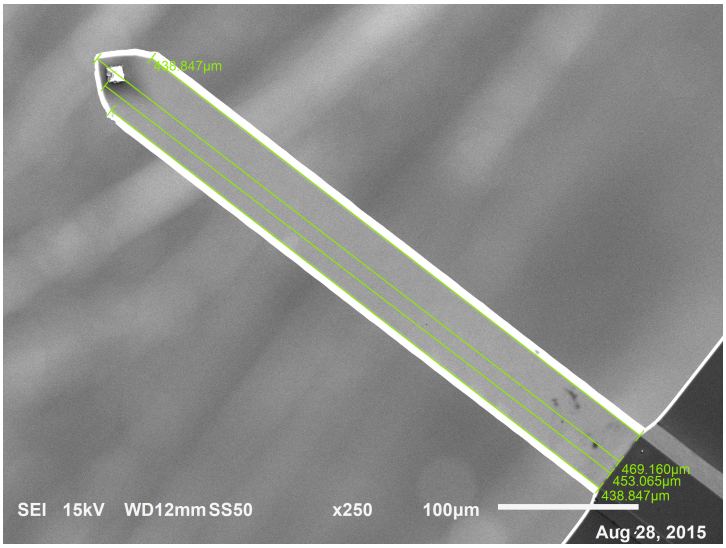

(b) Bottom of the cantilever to determine the lengths.

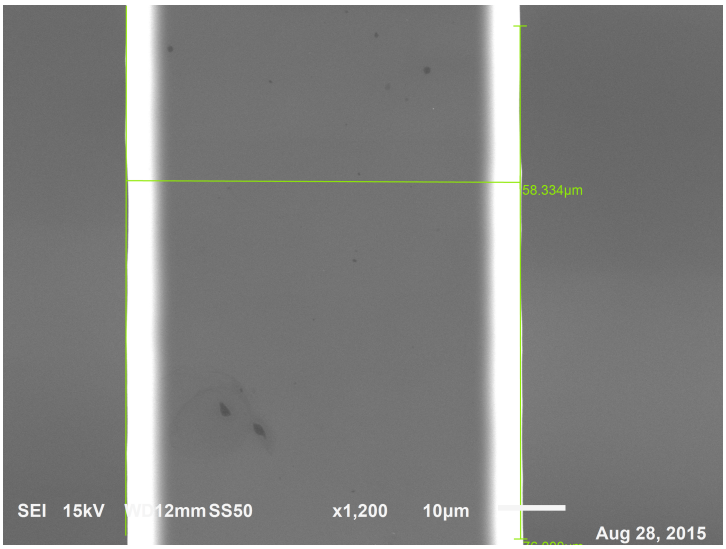

(c) Top of the cantilever to determine the width.

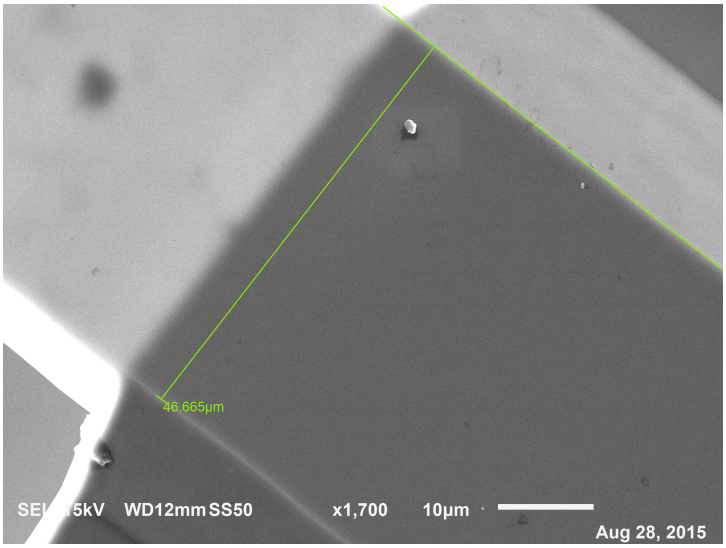

(d) Bottom of the cantilever to determine the width.

Figure B.1: SEM images taken from cantilever C1 to determine the dimensions.

C

TYPICAL DATASET VOLTAGE-DISPLACEMENT MEASUREMENT

The following micrographs are the result of a voltage-deflection measurement, as described in section 5.5. This dataset is the same as figure 5.22.

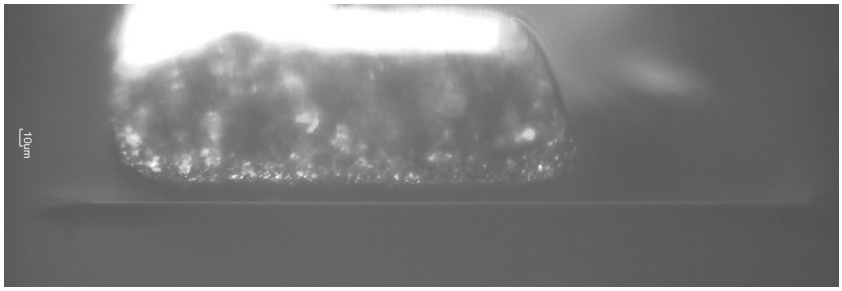

(a) $V_{DC} = 0$

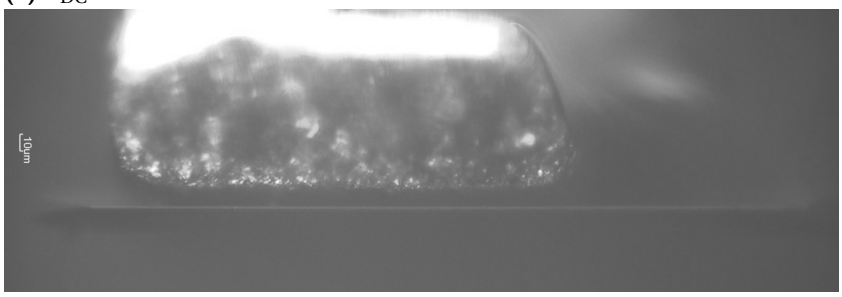

(b) $V_{DC} = 5$

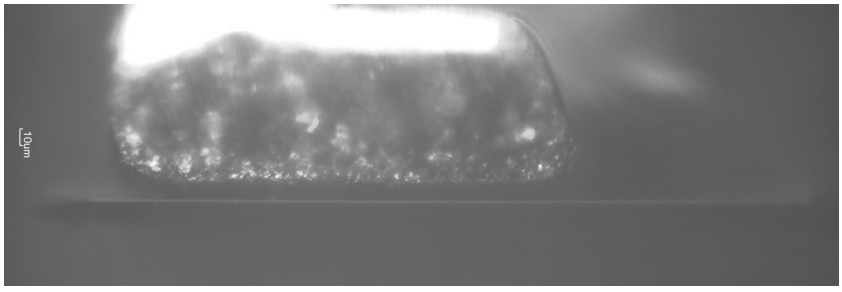

(c) $V_{DC} = 10$

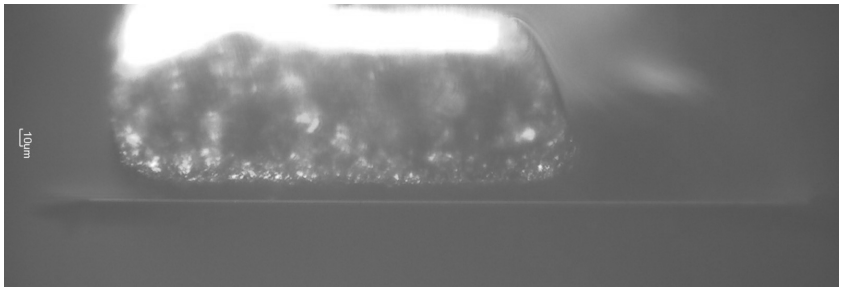

(d) $V_{\mathrm{DC}} = 15$

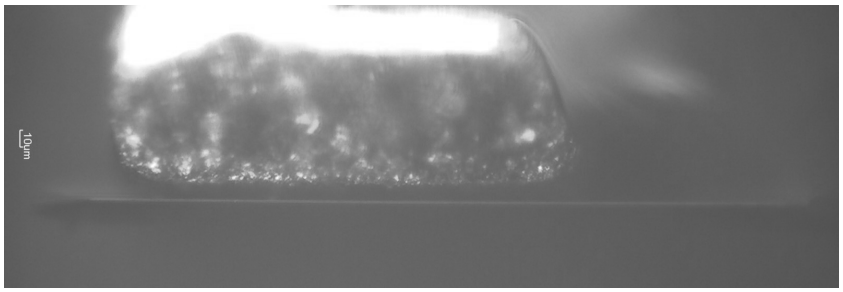

(e) $V_{\mathrm{DC}} = 20$

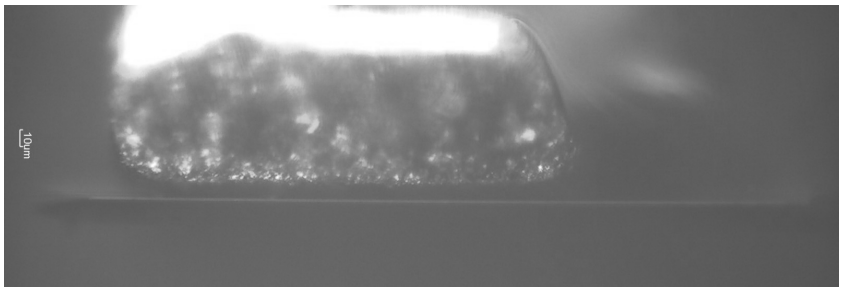

(f) $V_{\mathrm{DC}} = 25$

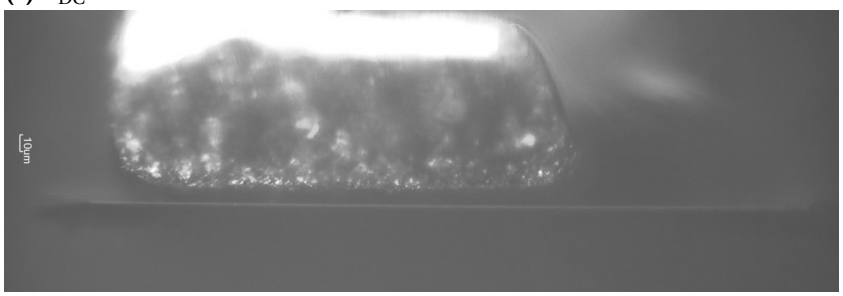

(g) $V_{\mathrm{DC}} = 26$

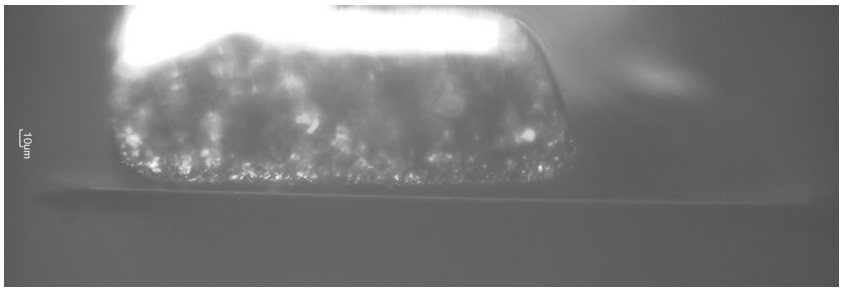

(h) $V_{\mathrm{DC}} = 37$

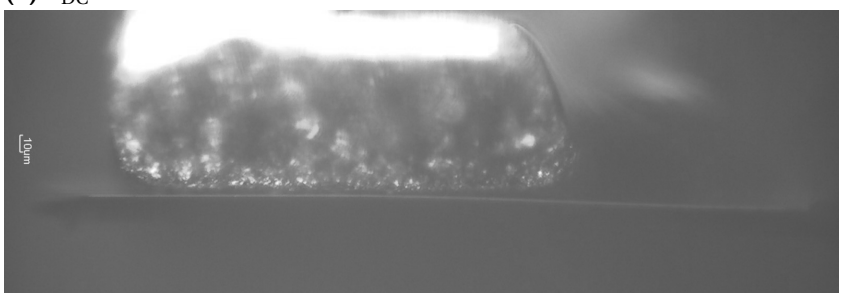

(i) $V_{\mathrm{DC}} \sim 50$

D

COMSOL MODEL

In this appendix the COMSOL model will be discussed in more detail. The physics, geometry, study and post processing will be discussed. The model is based on the 'electrostatic actuated cantilever' that can be found in the COMSOL model library.

D.0.4.1. STATIC MODEL

Physics The physics that were used is 'electromechanics'. This is needed to simulate the mechanical behavior of the cantilever and the electrostatic force caused by the applied potential.

Geometry The first step is making a plane geometry of the cross section of the cantilever and the surrounding air. This is shown in figure D.1. The cantilever itself is made with a polygon, while the air is made with a rectangle. Another rectangle is used to model the insulative layer. An extra line, splitting the cantilever in two, is added to make sure there is a mesh boundary at this point. This can be used to plot the cross-section. Next, the planar geometry is extruded, which is shown in figure D.2. This is done in two steps; region without

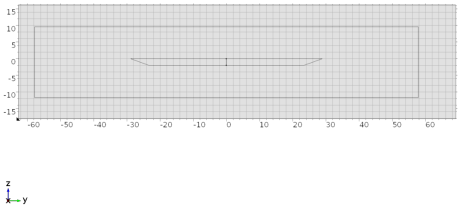

Figure D.1: The cross section of the cantilever and surrounding air modeled in COMSOL.

overlap with electrode and a region with overlap up to L_{side}. An extra block is added for the air, surrounding this part of the cantilever. This block is 10 µm longer than the length of the cantilever. The insulative layer is made with two hexahedrons.

Materials and physics The material of the cantilever is silicon, the insulative layer is a material with relative permittivity of 4.03 and the remaining domains are made of air. The default material properties are used. The most important properties are the relative permittivity of air of 1, Young's modulus of silicon 169 GPa and Poisson's ratio of silicon 0.28, which is equal to the values used for the analytical model.

The base of the cantilever is chosen to be a fixed constraint and the static potential is applied to the entire top surface of the cantilever.

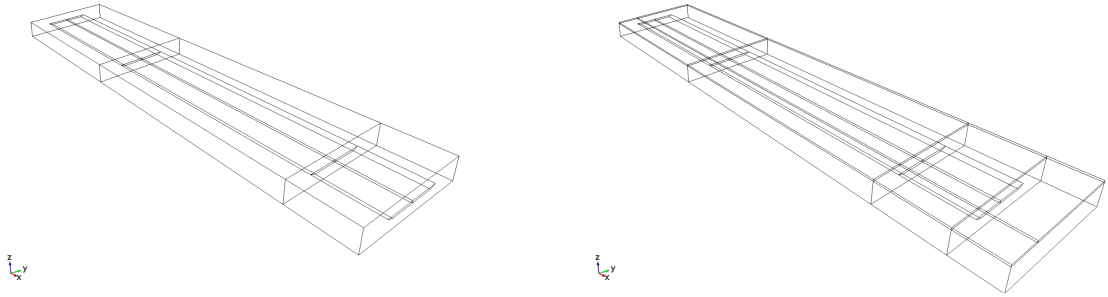

(a) The extrusion of the planar geometry of figure D.1 in different stages. **(b)** The complete geometry.

Figure D.2: The 3D design of the cantilever in COMSOL

Mesh Next, the mesh is generated. Because a large part of the geometry has a constant cross section, a planar, quad mesh is applied to the plane at the base as shown in figure D.3a, that is swept through the geometry as shown in figure D.3b. A mesh convergence study has been performed, by comparing course and fine meshes. A finer mesh should give more accurate results, while a course mesh provides fast calculation. The results will converge for an increasing amount of elements, but more elements do not necessarily result in a more accurate model; the location of the elements is an important fact to consider. The mesh of the planar geometry and the swept are varied, with the predefined settings in COMSOL ('normal','fine','extra fine' etc.). In order to make a comparison between the different meshes, the tip displacement is used as the parameter of comparison. And all the meshes are solved in a static case, where a potential of 25 V is applied. The results of the convergence study are summarized in table D.1, where the results are organized according to the number of elements.

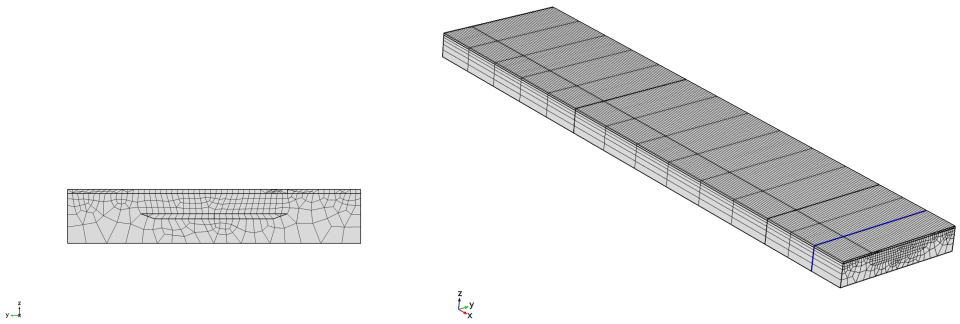

(a) The extrusion of the planar geometry of figure D.1 in different stages. **(b)** The complete geometry.

Figure D.3: The 3D design of the cantilever in COMSOL

Table D.1: Results of the mesh convergence study. Where the refinement of the parts of the mesh (planar, swept and tetrahedral) are used as variables for the number of degrees of freedom (DOF) and maximum displacement that was found.

Number	Planar Mesh	Swept	DOF	Tip deflection (μm)
1	extra fine	fine	173155	1.824
2	fine	extra fine	166131	1.875
3	finer	fine	117059	1.710
4	fine	fine	76507	1.8805
5	normal	fine	41895	1.647

E

MATLAB CODE

This appendix contains the details of the Matlab code, which is used for the voltage-deflection experiments of section 5.5. This code processes the analysis on the collected micrographs, which show the side view of the cantilever under a varying bias voltage. This is compared with the analytical model and results from COMSOL. Figure E.1 shows a diagram of the m-files that were used and how they are cooperating.

Master.m The master-file is the main file of this code. The other parts of this analysis are managed from here. First the physical constants and the measured parameters of the cantilevers are are loaded in the workspace. The master-file then calls a function, that calculates the thickness, stiffness and second moment of inertia of the cantilever as a function of the measured parameters. It returns the nominal values, and the most optimistic and pessimistic estimate, according to the measurement uncertainty (see section 5.1). Next, the measurement data is processed in 'measurement.m', resulting in a vector with cantilever deflection and a vector with corresponding voltages. Now the model can be calculated. This is not only done for the nominal stiffness, but also for the upper and lower bound of the stiffness, as it was calculated in the previous function file. Also the measurement accuracy on the gap is taken into account; the gap is assumed to be measured with a $\pm 0.5\mu$m accuracy. The minimum gap is used for the lower bound of the stiffness, while the maximum gap is used for the upper bound of the stiffness. The measurement and model can also be compared with the COMSOL model. The file 'ReadComsol.m' reads out a text file that is generated by COMSOL and creates a vector with deflection and a vector with voltages. Finally the three methods are combined in a plot.

Thickness_Resonance.m The thickness of the cantilever is measured by solving $f = \frac{1}{2\pi}\sqrt{\frac{k}{m_{\text{eff}}}}$ for the thickness t. This is done in the function 'Thickness_Resonance.m'. As explained in section 5.1, there is an uncertainty on the measured parameters, which is estimated to be $\pm 0.5\mu$m. The thickness is calculated for all the possible combination of parameters in nominal, overestimated and underestimated state. This is done with the function 'SolveSymbolic.m', that accepts the geometry of the cantilever, and returns the corresponding thickness. The maximum and minimum thickness of the cantilever, as well as the nominal value are returned by the function.

SolveSymbolic.m This file is generated by 'Generate_SolveSymbolic.m', which converts a symbolic expression to this numerical function. This saves computation time. This numerical function uses the geometry of the cantilever to calculate the thickness.

Generate_SolveSymbolic.m This code converts a symbolic function into a numerical function with the function 'matlabFunction'. The mass and stiffness are expressed as a (symbolic) function of the thickness, where this thickness is the only unknown. The equation for the resonance frequency is then solved for this unknown thickness.

Measurement.m Next, the measurement data is processed in the m-file 'Measurement.m'. In the first part of the code, the settings can be chosen. This will pop up as a dialog box when running the code. A vector with voltages and the pixel size in x- and y-direction are inserted. Next, the reference image is loaded into the system. It goes into full screen and a mouse click is used to indicate the approximate position of the end of the cantilever and location of the electrode; this is the region of interest. Next, the location of the cantilever is determined in a 'while-loop'. (Before running the code, a threshold must be selected. This is the intensity of the pixels of the cantilever.) The code takes the point that was selected with the mouse click and starts looking in a vertical line, with the specified range for a pixel with an intensity that at least as big as the threshold. When it cannot find such a pixel, it moves one line to the right. It keeps repeating this procedure, until the condition is met. Now the position of the end of the cantilever is known in the reference image. Now a spline is created for the electrode and for the end of the cantilever. This is done with a separate function file 'createspline.m'. For the cantilever, five lines of pixels are averaged in x-direction, such that the measurement becomes less sensitive to noise and errors. The Electrode is averaged over its entire width. In a for-loop, the image analysis is done. The subsequent images are compared by comparing the new intensity profiles with the earlier created spline. The shift of the new data with respect to the spline is determined in 'splineshift.m. The deflection of the cantilever is determined by subtracting the motion of the electrode of the deflection of the cantilever, because it is possible that the entire image has shifted a little bit. The final step is to calculate the deflection of the tip of the cantilever by extrapolating, because the deflection is measured at L_{side}.

createspline.m This file creates a spline fit from a data set. The inputs are the gray scale image, and the x- and y-range that are of interest. The pixel intensity is averaged over x, to minimize noise and errors. The 'fit' function of Matlab is used, with 'smoothing parameter' p set to 1, to get a cubic spline interpolant; in this way the spline stays as close as possible to the original data.

splineshift.m This file computes how many pixels the intensity profile has shifted compared with the spline. This is done with the least squares method, as explained in section 5.5.1.8.

Model.m This file calculates the voltage-deflection relation of the model as described in section 5.2. This model calculates the required bias voltage to reach equilibrium at a certain deflection of the cantilever. A vector is made that contains the deflection of the cantilever from zero to gap-size in steps of 0.01 µm. In a for-loop, the corresponding required bias voltage is calculated for all the elements in this vector. The system is unstable as soon as the bias voltage starts decreasing for an increasing deflection instead of increasing. So at the maximum voltage the cantilever will snap in. The voltage-deflection relation up to the snap-in voltage is the output of this file.

ReadComsol.m A COMSOL simulation has been made for the system. A text file with the voltage-displacement relation has been exported after this simulation. This can be imported into Matlab with this file. This code is generated by using the 'import data' tool, and a automated scripts has been created.

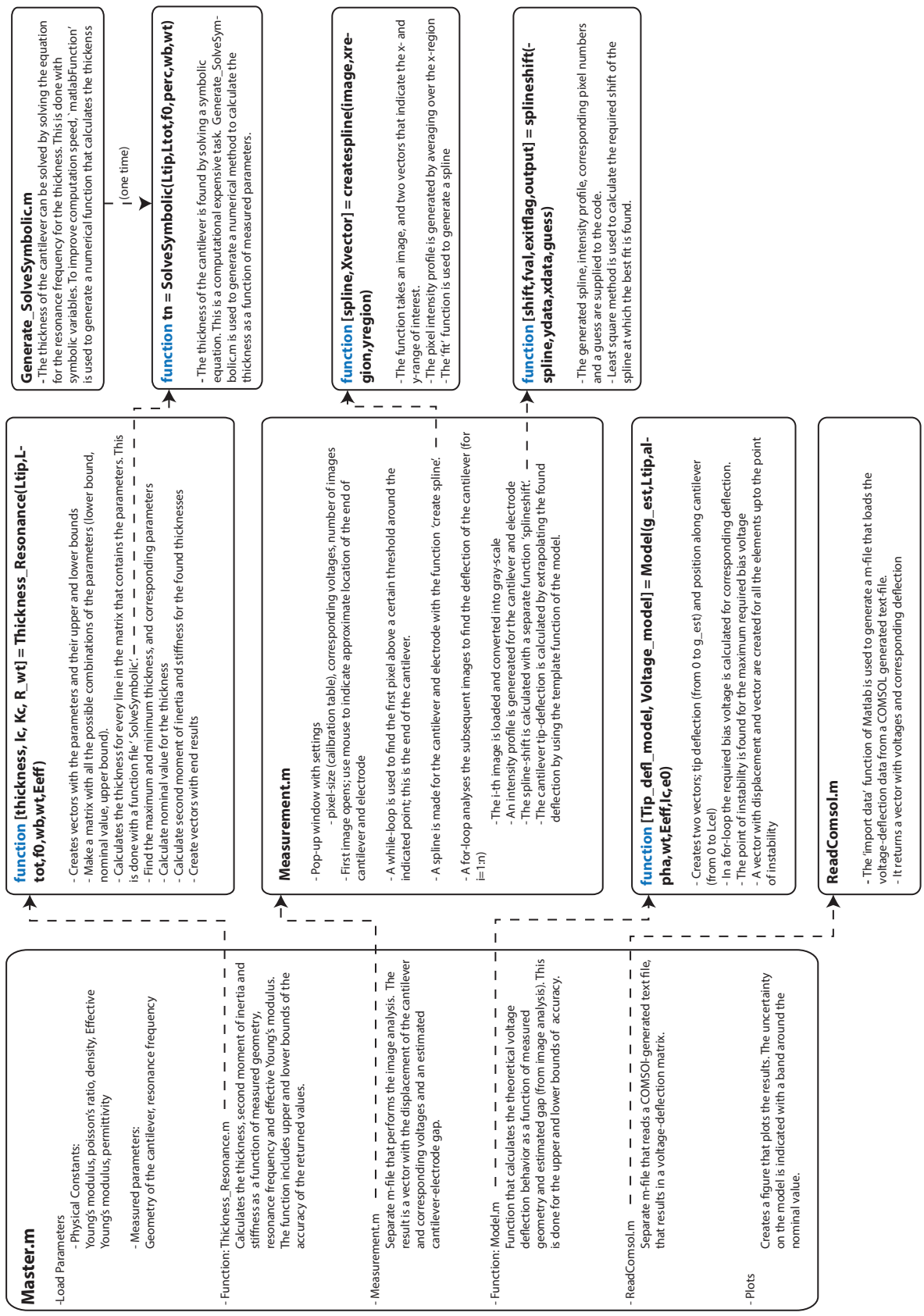

Figure E.1: Diagram of the Matlab code for comparing measurements with the model.

MASTER.M

```
%% Master file to compare measurement, model and COMSOL
%  by Marcel de Laat
%  Master project: Adjustable stiffness AFM probe
%  This code is used to analyse the Voltage-deflection behavior of a
%  commercially available AFM cantilever (BudgetSensors, 450um, 13khz, Al
%  coating). Measurements, a semi-analytical model and a COMSOL model are
%  compared in this code.
%  The data of this code is based on Cantilever C7
clear all; clc; close all;

%% Parameters
% Constants
E = 169e9;          % Young's modulus (Pa)
v = 0.28;           % Poisson's ratio
rho = 2329;         % Density silicon  (kg/m^3)
Eeff = E/(1-v^2);   % Effective Young's modulus (Pa)
e0 = 8.85e-12;      % Absolute permittivity (F/m)
eair = e0;          % Permittivity in vacuum
erd = 4.03;         % Relative permittivity of dielectric
eins = e0*erd;      % Absolute permittivity of dielectric

% Measured
Ltip = 455.7e-6;    % Length base-tip cantilever (m)
Ltot = 476.9e-6;    % Total length cantilever (m)
Lside = 443.4e-6;   % Length of the side of cantilever (m)
Lel = 229.4e-6;     % Overlap electrode - cantilever (m)
wt = 57.8e-6;       % Width at top - electrode side (m)
wb = 46.7e-6;       % Width at bottom - tip side (m)
f0 = 13265.63;      % Measured resonance frequency (Hz)
ht = 15e-6;         % Tip height (m)
lt = 6e-6;          % length tip-base (m)
bt = 6e-6;          % width tip-base (m)
dins = 1.60e-6;     % Thickness of dielectric layer
g_est = 8.013e-6;   % Estimated gap
a = 52e-6;          % Effective length after pull-in
Lcel = Ltip-a;      % Length of cantilever upto edge of electrode
alpha = Lel/Lcel;   % Ratio between electrode length and effective length

%% Calculation of the thickness and stiffness of the cantilever
[thickness, Ic, Kc, wt_acc] = Thickness_Resonance(Ltip,Ltot,f0,wb,wt,Eeff);

%% Measurements
Measurement             % The m-file that processes the images.

%% Model
% Calulates the model for upper bound, lower bound and nominal value
[Tip_defl_modelmin, Voltage_modelmin] = Model(g_est-0.5e-6,Ltip,alpha,wt_acc(1),Eeff
    ,Ic(1),eair,eins,dins);
[Tip_defl_model, Voltage_model] = Model(g_est,Ltip,alpha,wt_acc(2),Eeff,Ic(2),eair,
    eins,dins);
[Tip_defl_modelmax, Voltage_modelmax] = Model(g_est+0.5e-6,Ltip,alpha,wt_acc(3),Eeff
    ,Ic(3),eair,eins,dins);

%% Read COMSOL data
ReadComsol
```

```

%% Plots
[TRIVIAL]
```

THICKNESS_RESONANCE.M

```
% Code to determine the thickness of the cantilever

function [thickness, Ic, Kc, R_wt] = Thickness_Resonance(Ltip,Ltot,f0,wb,wt,Eeff)
    R_Ltip = [Ltip-1e-6 Ltip Ltip+1e-6];    % Length base-tip cantilever (m)
    R_Ltot = [Ltot-1e-6 Ltot Ltot+1e-6];    % Total length cantilever (m)
    R_f0 = [f0-3.12 f0 f0+3.12];                    % Measured resonance frequency
        (Hz)
    R_perc = [0.8 1 1.2];                   % Percentage of the tip-volume +-
        20%
    R_wb = [wb-0.5e-6 wb wb+0.5e-6];        % Width at bottom - tip side (m)
    R_wt = [wt-0.5e-6 wt wt+0.5e-6];        % Width at top - electrode side (m)

    vect=combvec(R_Ltip,R_Ltot,R_f0,R_perc,R_wb,R_wt)';     % Make a matrix with all
        combinations of the variables
    t=[];
    for i=1:length(vect)                                    % Calculates the
        thickness of the cantilever for all possible combinations of variables
        vector = vect(i,:);
        t(i)=real(SolveSymbolic(vector(1),vector(2),vector(3),vector(4),vector(5),
            vector(6)));
    end

    [t_min, I_min] = min(t);                                                %
        Maximum thickness
    [t_max, I_max] = max(t);                                                %
        Minimum thickness
    Ic_min = (t_min^3/36)*(vect(I_min,6)^2+vect(I_min,5)^2+4*vect(I_min,5)*vect(
        I_min,6))/(vect(I_min,5)+vect(I_min,6));    % Minimum second moment of area
    Kc_min = 3*Eeff*Ic_min/vect(I_min,1)^3;

        % Minimum stiffness
    Ic_max = (t_max^3/36)*(vect(I_max,6)^2+vect(I_max,5)^2+4*vect(I_max,5)*vect(
        I_max,6))/(vect(I_max,5)+vect(I_max,6));    % Maximum second moment of area
    Kc_max = 3*Eeff*Ic_max/vect(I_max,1)^3;

        % Maximum stiffness

    t_nom = real(SolveSymbolic(Ltip,Ltot,f0,R_perc(2),wb,wt));
                                % Nominal value of the thickness
    Ic_nom = (t_nom^3/36)*(R_wt(2)^2+R_wb(2)^2+4*R_wt(2)*R_wb(2))/(R_wb(2)+R_wt(2));
            % Second moment of area cantilever (m^4)
    Kc_nom = 3*Eeff*Ic_nom/R_Ltip(2)^3;
                                                % Stiffness cantilever (N/m)

    thickness = [t_min; t_nom; t_max];          % Create vector with results
    Ic = [Ic_min; Ic_nom; Ic_max];              % Create vector with results
    Kc = [Kc_min; Kc_nom; Kc_max];              % Create vector with results
end
```

GENERATE_SOLVESYMBOLIC.M

```
% This file generates a m-file that is depending on symbolic expressions.
syms t Ltip Ltot wt wb f0 perc positive

% Constants
E = 169e9;              % Young's modulus (Same as Comsol) (Pa)
v = 0.28;               % Poisson's ratio (Same as Comsol)
rho = 2329;             % Density silicon (Same as Comsol) (kg/m^3)
Eeff = E/(1-v^2);       % Effective Young's modulus (Do) (Pa)

% Parameters (To be measured!)
ht = 15e-6;             % Tip height (m)
lt = 6e-6;              % length tip-mbase (m)
bt = 6e-6;              % width tip-base (m)

% Derived parameters
vt = ht*lt*bt/3;          % Volume of tip - pyramid approximation (m^3)
mt = rho*(vt+((wt+wb)/4)*(Ltot-Ltip)*t);              % Mass of tip (kg)

%% Calculation of the thickness and stiffness of the cantilever
vc = 0.5*(wt+wb)*t*Ltip;    % Volume of cantilever (m^3)
mc = vc*rho;                % Mass of cantilever (kg)
meff = (33/140)*mc+mt;      % Effective mass cantilever + tip (kg)

Ic = (t^3/36)*(wt^2+wb^2+4*wt*wb)/(wb+wt);    % Second moment of area cantilever (m
    ^4)
k = 3*Eeff*Ic/Ltip^3;                         % Stiffness cantilever (N/m)

tn = solve(f0==(1/(2*pi))*sqrt(k/meff),t,'Real', true);  % Thickness of the
    cantilever
g = matlabFunction(tn,'File','SolveSymbolic');
```

MEASUREMENT.M

```
global g_est

%% Settings
% Opens dialogbox to enter settings
prompt = {'Enter number of datapoints:','Enter n space-separated Voltages','The size
     of one pixel-X (micrometer/pixel):','The size of one pixel-Y (micrometer/pixel):
    '};
dlg_title = 'Input';
num_lines = 1;
answer = inputdlg(prompt,dlg_title,num_lines,def);
n = str2num(answer{1});
Voltages = str2num(answer{2});
pixelsizex = str2num(answer{3}); % Size of pixel in x
pixelsizey = str2num(answer{4}); % Size of pixel in y

%% Select regions of interest
PicName0 = ['0.jpg'];           % Create filename for the zero-bias picture
image0 = imread(PicName0);      % Load image
Gray0 = rgb2gray(image0);       % Convert to grayscale
figure(1);                      % Create new figure
imshow(Gray0);                  % Show grayscale image
```

```
set(gcf,'units','normalized','outerposition',[0 0 1 1]) % Fullscreen
uiwait(msgbox('Left-Click three times in the image'));
[xc,yc] = ginput(3);                % Click once
ydatr = round(yc);                  % Rounded values (-> Discrete Pixels)
xdatr = round(xc);                  % Rounded values (-> Discrete Pixels)

%% Cantilever location
maxthresh = 123;        % Threshold (different for each dataset)
xrange = 0;             % Amount of pixels to look to the left
yrange = 30;            % Amount of pixels to look in the y-direction
j = 0;                  % Initializing numbers for loop
Max = 0;                % Initializing value 'Max'
while Max < maxthresh  % Find the location of the tip
    % Take the first line from the left of the region of interest
     Line = Gray0(ydatr(1)-yrange/2:ydatr(1)+yrange/2,(xdatr(1)-xrange+j));
     Max = max(Line);                                % Find maximum value
     xcant = xdatr(1)-xrange+j;                      % The x-location of the cantilever
     ycant = ydatr(1)-yrange/2+find(Line==Max)-1;% The y-location of the cantilever
     j=j+1;                                          % Takes next line for the next loop
end
ycant=min(ycant);  % In the case that multiple pixels are selected, pick the top one

%% Create Spline for the cantilever and the electrode
n_avg_cant = 10;    % Number of pixels for averaging to the right
y_range_cant = 30;  % Range of pixels to look up and down for cantilever
y_range_el = 50;    % Range of pixels to look up

% Create spline for the cantilever
[spline_cant,Xvector_cant] = createspline(Gray0,(xcant):(xcant+n_avg_cant),ycant-
    y_range_cant:ycant+y_range_cant);
% Create spline for the electrode
[spline_el,Xvector_el] = createspline(Gray0,xdatr(2):xdatr(3),ydatr(2)-20:ydatr(2)
    +20);

%% Image recognition for all images
% Initialize values that are being used in the for-loop.
cant_shift=[];
cant_shift_end=[];
x_shift = 0;
y_shift = 0;
cant_shift(1) = 0;
el_shift = 0;
cant_shift(1) = 0;
for i=1:n
    % Load Image
    PicNamel = [num2str(i) '.jpg'];  % Create filename depending on number
    imagel = imread(PicNamel);       % Load image
    Grayl = rgb2gray(imagel);        % Convert to grayscale

    % Detect motion of the cantilever relative to electrode; generate
    % vectors with (average) pixel intensity.
    int_prof_cant = mean(Grayl(ycant-y_range_cant+round(cant_shift(i)):ycant+
        y_range_cant+round(cant_shift(i)),xcant:xcant+n_avg_cant)');
    int_prof_el = mean(Grayl(ydatr(2)-20+round(el_shift(i)):ydatr(2)+20+round(
        el_shift(i)),xdatr(2):xdatr(3))');

```

```
    % Calculate the spline shift
    % Calculate the shift of the cantilever
    [cant_shift(i+1),fval(i),~,~] = splineshift(spline_cant,int_prof_cant,
        Xvector_cant,0);
    % Calculate the y-shift of the electrode
    [el_shift(i+1),~,~,~] = splineshift(spline_el,int_prof_el,Xvector_el,0);

    % Add the rounded value of the previous loop
    cant_shift(i+1)=cant_shift(i+1)+round(cant_shift(i));
    el_shift(i+1) = el_shift(i+1)+round(el_shift(i));
end

% Calculate the deflection of the cantilever relative to the electrode
Cant_deflection = cant_shift-el_shift;
```

CREATESPLINE.M

```
function [spline,Xvector] = createspline(image,xregion,yregion)
%% Description of the function
% This function receives an image (in gray scale) with the feature in
% x-direction, and two vectors that describe the region of interst.
% It returns the spline for the averaged data

%% Make an average over the x-axis
DataAverage = mean(image(yregion,xregion)')';
Xvector = [yregion(1):1:yregion(end)]';

%% Create the spline for the electrode and the cantilever
spline = fit(Xvector,DataAverage,'smoothingspline','SmoothingParam',1);
end
```

SPLINESHIFT.M

```
function [shift,fval,exitflag,output] = splineshift(spline,ydata,xdata,guess)
%% Description of the function
% This function receives a defined spline and raw measurement data (single vector)
% It calculates the shift of the raw data, such that it fits the spline
f_min = @(x_shift)sum((spline(xdata-x_shift)-ydata).^2); % Least squares
[shift,fval,exitflag,output] = fminsearch(f_min,guess,optimset('TolX',1e-8)); %
    Minimize least squares function for shift
end
```

MODEL.M

```
%% The forloop calculates the necessary voltage to reach equilibrium for the
% given tip deflection. Instability occurs at dV/dy_L=0
% Also the shape of the cantilever is calculated for each given tip
% deflection

function [Tip_defl_model, Voltage_model,dydx] = Model(g_est,Ltip,alpha,wt,Eeff,Ic,
    Lcel,eair,eins,dins)
y_L = [0:1e-8:g0];              % Tip deflection
x_cant = [0:1e-6:Lcel];         % Vector with points along x-axis  base - tip
```

```
9
10 for l = 1:length(y_L)
11     y_Li = y_L(l);
12     integralfunction = @(x) x.^2.*(3*Lcel-x)./((eair*dins)+eins*(g_est
           -(2.56-16.127./(4*(x./Lcel+0.00185).^2+6.2786))*y_Li)).^2;
13     intf = integral(integralfunction,(Lcel-alpha*Lcel),Lcel);
14     % Effective width to compensate for fringe field.
15     weff = wt*(1+0.65*g0*(1-y_Li/g_est)/(wt));
16     % Voltage necessary to reach equilibrium at deflection y_Li
17     V(l,:) = sqrt((12*Eeff*Ic*y_Li)/(eair*eins^2*weff*intf));
18     % Shape of the cantilever for deflection y_Li (um)
19     yx(l,:) = (2.56-(16.127./(4*(x_cant./Lcel+0.00185).^2+6.2786))).*y_Li;
20     % Derivative at y(Lcel)
21     dydx(l) = (yx(l,end)-yx(l,end-1))/(x_cant(2)-x_cant(1));
22 end
23
24 [~, Imax] = max(V);              % Pull-in voltage
25 Imax = Imax(ceil(end/2));        % Take middle value, if more than one
26 % Calculate deflection at y(Ltip)
27 Tip_defl_model = y_L(1:Imax)+dydx(1:Imax)*(Ltip-Lcel);
28 Voltage_model = V(1:Imax);          % Corresponding voltages with tip deflections
29 end
```

F

POSTER FOR INTERNATIONAL MICRO NANO CONFERENCE AMSTERDAM

The present work was presented with a poster on the International Micro Nano Conference in Amsterdam on 8 and 9 December 2015. The poster that was used for this conference is shown in this appendix.

In situ stiffness adjustment for AFM probes: up to two orders of magnitude

M L C de Laat[1], H H Pérez Garza[2], M K Ghatkesar[1]
[1]Delft University of Technology, [2] DENSSolutions BV

Marcel de Laat
Delft University of Technology
PME - Micro and Nano Engineering (MNE)
Mekelweg 2, 2628 CD, Delft
The Netherlands
Tel: +31 6 5251 8244
Email: m.l.c.delaat@student.tudelft.nl

1. Motivation

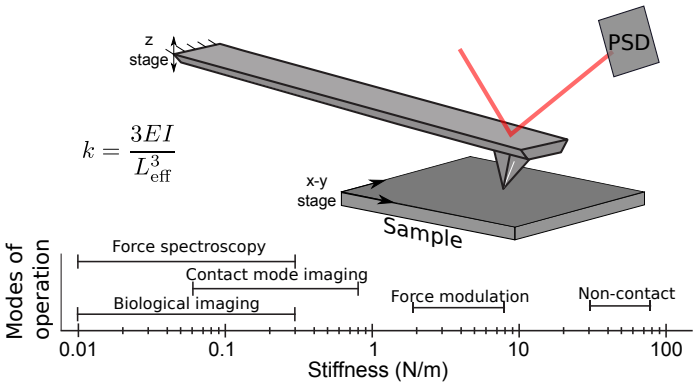

Typically, cantilevers are exchanged for different modes of operation. Can we design a stiffness–tunable AFM probe that covers the entire range of stiffness, without exchanging it?

2. State of the art

In plane AFM probe

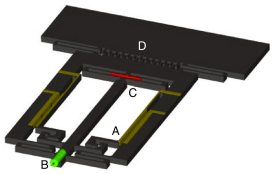

Mueller-Falcke *et al.*, 2006, Nanotechnology 17

- Discrete stiffness adjustment
- Incompatible with commercial AFM systems
- Large range (10x increase)

Piezoelectric bending

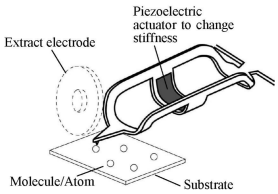

Kawai *et al.*, 2006, 19th International Conference on Micro Electro Mechanical Systems

- Limited tuning range (~14%)
- Compatible with commercial systems
- Continuous tuning

3. Concept

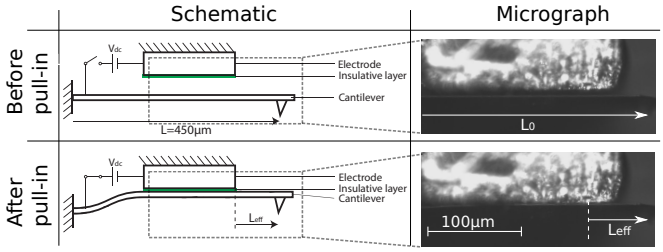

- By applying a large voltage, the cantilever will pull-in.
- The effective length of the cantilever will be reduced, hence its stiffness will increase.

4. Experimental setup

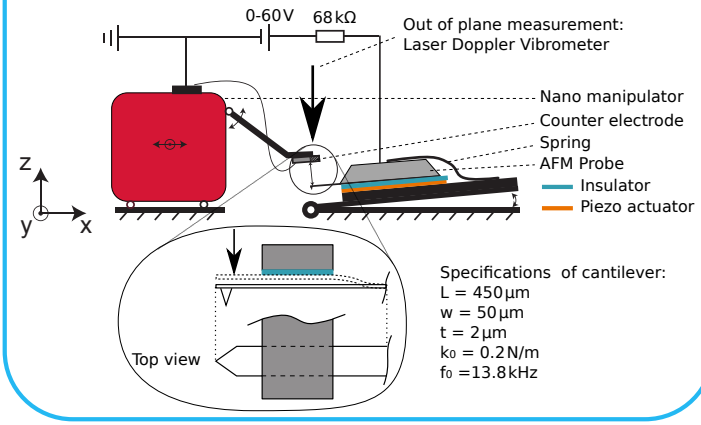

5. Results

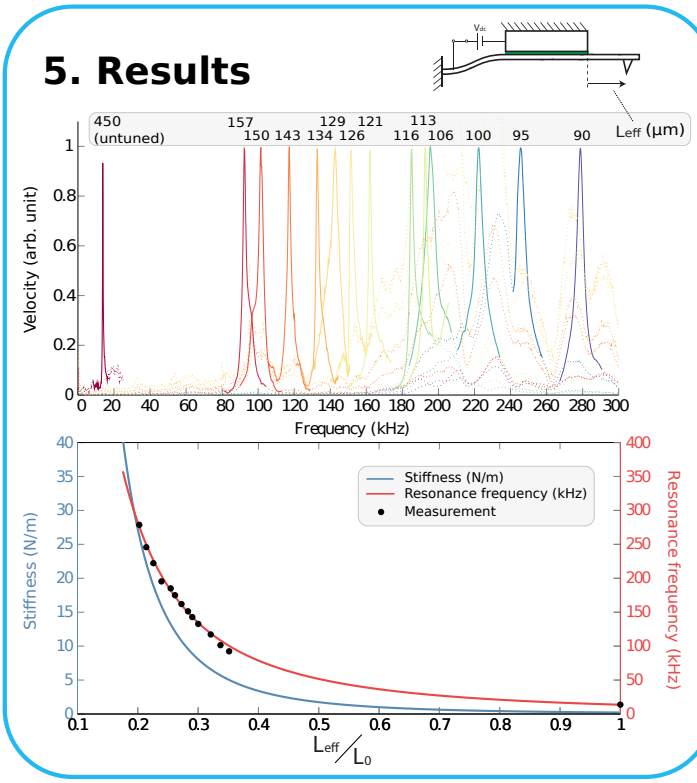

6. Conclusions & outlook

The entire range of stiffness can be covered in a single cantilever. For the tested cantilever we obtained stiffnesses from 0.2 N/m to 27 N/m, covering two orders of magnitude in a single cantilever.

This proof of concept is the first step towards a micro fabricated prototype. This should integrate the electrode positioning system and cantilever such that it can be used in an actual AFM setup.

TU Delft Delft University of Technology

Challenge the future